ISSN en trámite

Geofísica Internacional

Revista Trimestral Publicada por el Instituto de Geofísica de la
Universidad Nacional Autónoma de México

México
Volume 58 Number 4
October - December
2019

— Geofísica Internacional —

Dr. Hugo Delgado Granados
Director of Instituto de Geofísica

Dra. Ligia Pérez Cruz
President of Unión Geofísica Mexicana

Editor Chief
Dr. Servando De la Cruz-Reyna
Instituto de Geofísica, UNAM
sdelacrr@geofisica.unam.mx

Technical Editor
Mtra. Andrea Rostan Robledo
Instituto de Geofísica, UNAM
arostan@igeofisica.unam.mx

Editorial Board
Donald Bruce Dingwell
Earth and Environment
Ludwig Maximilian University of Munich, Germany

Eric Desmond Barton
Departamento de Oceanografía
Instituto de Investigaciones Marinas, Spain

Jorge Clavero
Amawta Consultores, Chile

Gerhardt Jentzsch
Institut für Geowissenschaften
Friedrich-Schiller-Universität Jena, Germany

Peter Malischewsky
Institut für Geowissenschaften
Friedrich-Schiller-Universität Jena, Germany

François Michaud
Géosciences Azur
Université Pierre et Marie Curie, France

Olga Borisovna Popovicheva
Scobeltzine Institute of Nuclear Physics
Moscow State University, Rusia

Jaime Pous
Facultad de Geología
Universidad de Barcelona, Spain

Joaquín Rui
UA Science
University of Arizona, United States

Angelos Vourlidas
Solar Physics Branch
NASA Goddard Space Flight Center, United States

Théophile Ndougsa Mbarga
Department of Physics
University of Yaounde I, Cameroon

Associate Editors
José Agustín García Reynoso
Atmospheric Science Centro de Ciencias de la Atmósfera UNAM, Mexico

Tereza Cavazos
Atmospheric Science
Departamento de Oceanografía Física CICESE, Mexico

Dante Jaime Morán-Zenteno
Geochemistry
Instituto de Geología, UNAM, Mexico

Margarita López
Geochemistry
Instituto de Geología UNAM, Mexico

Avto Gogichaisvilii
Geomagnetism And Paleomagnetism
Instituto de Geofísica UNAM, Mexico

Jaime Urrutia-Fucugauchi
Geomagnetism And Paleomagnetism
Instituto de Geofísica, UNAM, Mexico

Felipe I. Arreguín Cortés
Hydrology
Instituto Mexicano de Tecnología del Agua IMTA, Mexico

William Lee Bandy
Marine Geology And Geophysics
Instituto de Geofísica UNAM, Mexico

Fabian García-Nocetti
Mathematical And Computational Modeling
Instituto de Investigaciones en Matemáticas Aplicadas y en Sistemas UNAM, Mexico

Graciela Herrera-Zamarrón
Mathematical Modeling
Instituto de Geofísica, UNAM, Mexico

Ismael Herrera Revilla
Mathematical And Computational Modeling
Instituto de Geofísica UNAM, Mexico

Rene Chávez Segura
Near-Surface Geophysics
Instituto de Geofísica UNAM, Mexico

Juan García-Abdeslem
Near-Surface Geophysics
División de Ciencias de la Tierra CICESE, Mexico

Alec Torres-Freyermuth
Oceanography
Instituto de Ingeniería, UNAM, Mexico

Jorge Zavala Hidalgo
Oceanography
Centro de Ciencias de la Atmósfera UNAM, Mexico

Shri Krishna Singh
Seismology
Instituto de Geofísica, UNAM, Mexico

Xyoli Pérez-Campos
Seismology
Servicio Sismológico Nacional, UNAM, Mexico

Blanca Mendoza Ortega
Space Physics
Centro de Ciencias de la Atmósfera, UNAM, Mexico

Inez Staciarini Batista
Space Physics
Pesquisador Senior Instituto Nacional de Pesquisas Espaciais, Brazil

Roberto Carniel
Volcanology
Laboratorio di misure e trattamento dei segnali DPIA - Università di Udine, Italy

Miguel Moctezuma-Flores
Satellite Geophysics
Facultad de Ingeniería, UNAM, Mexico

Assistance
Elizabeth Morales Hernández,
Management
eliedit@igeofisica.unam.mx

GEOFÍSICA INTERNACIONAL, Año 58, Vol. 58, Núm. 4, octubre - diciembre de 2019 es una publicación trimestral, editada por la Universidad Nacional Autónoma de México, Ciudad Universitaria, Alcaldía Coyoacán, C.P. 04150, Ciudad de México, a través del Instituto de Geofísica, Circuito de la Investigación Científica s/n, Ciudad Universitaria, Alcaldía Coyoacán, C.P. 04150, Ciudad de México, Tel. (55)56 22 41 15. URL: http://revistagi.geofisica.unam.mx, correo electrónico: revistagi@igeofisica.unam.mx. Editora responsable: Andrea Rostan Robledo. Certificado de Reserva de Derechos al uso Exclusivo del Título: 04-2022-081610251200-102, ISSN: en trámite, otorgados por el Instituto Nacional del Derecho de Autor (INDAUTOR). Responsable de la última actualización Saúl Armendáriz Sánchez, Editor Técnico. Fecha de la última modificación: 30 de septiembre 2019, Circuito de la Investigación Científica s/n, Ciudad Universitaria, Alcaldía Coyoacán, C.P. 04150, Ciudad de México.

Geofísica
Internacional

Vol. 58, Núm. 4, octubre-diciembre de 2019

Contents

Hydrogeochemical characterization and quantification of the groundwater mixture in a hydrogeological basin of the middle zone of San Luis Potosí.
S. Torres-Rivera, J. A. Ramos-Leal, J. Moran-Ramírez, J. R. Torres-Hernández, L. Padilla-Sánchez, S. E. Carranco-Lozada, M. E. García-Arreola 247

Structural Interpretation and Depth Estimation from Aeromagnetic Data of Abigi-Ijebu-Waterside area of Eastern Dahomey Basin, Southwestern Nigeria.
Osinowo Olawale Olakunle, Adabanija Moruffdeen A., Adewoye Oluwatoyin Adebayo 259

Electrical Resistivity Tomography for the detection of subsurface cavities and related hazards caused by underground coal mining in Coahuila.
José A. Batista Rodríguez, Marco A. Pérez Flores, Yuri Almaguer Carmenates, Maximiliano Bautista Hernández 279

Oceanographic units of Gulf of Mexico and adjacent areas: The monthly integration of surface biophysical features.
A. Uribe-Martínez, R. Aguirre-Gómez, J. Zavala-Hidalgo, R. Ressl, E. Cuevas 295

Geofísica Internacional (2019) 58-4: 247-258

Original paper

Hydrogeochemical characterization and quantification of the groundwater mixture in a hydrogeological basin of the middle zone of San Luis Potosí

Torres-Rivera S., Ramos-Leal J. A., Moran-Ramírez J., Torres- Hernández J. R., Padilla-Sánchez L., Carranco-Lozada S. E. and García-Arreola M. E.

Received: November 15, 2017; accepted: september 24, 2019; published on line: October 01, 2019

Resumen

Los procesos de caracterización hidrogeoquímica e interacción agua-roca en las subcuencas de Santa Catarina y Ocampo-Paraíso en la Zona Media de San Luis Potosí han permitido identificar los tipos de aguas subterráneas. Los resultados del análisis químico y el estudio geológico regional han permitido documentar los posibles mecanismos de interacción del agua con la roca. Los resultados indican que la composición del agua subterránea en cada una de estas cuencas refleja la disolución por el agua de lluvia de los minerales de carbonato y magnesio de las rocas carbonatadas de la formación del Cretácico (Formación El Abra del Cretácico) y del flujo subterráneo a través de un medio granular con fuerte influencia del material de origen volcánico. Las aguas del tipo Ca-HCO_3, Ca-Mg-HCO_3 se modifican durante el flujo subterráneo mediante la incorporación de iones Na^+ y SO_4^{2-}. En el caso de la subcuenca III de San Nicolás, se ha documentado que su relleno incluye depósitos fluviales que pueden depositarse en condiciones climáticas de regiones semiáridas. El análisis hidrogeoquímico de las concentraciones de iones mayores, litio y bromo, permitieron identificar que el agua que se extrae de la región es producto de un proceso de mezcla en la que intervienen tres miembros extremos (mezcla ternaria): El primero, Santa Catarina (C_1), tiene las concentraciones más bajas de bromo y litio en la recarga ocurre en las partes de mayor altitud en la región, hacia la Sierra de Álvarez. El segundo miembro (C_2), tiene valores altos del bromo, bajo en litio y se origina hacia el valle de Ocampo Paraíso. El tercer miembro (C_3), tiene bajas concentraciones de bromo, alto en litio y proviene de área de San Nicolás Tolentino. Los porcentajes de mezcla indican que C_1, aporta el 50%, C_2 contribuye con el 31% y C_3 aporta 19 %, del agua al sistema.

Palabras clave: hidrogeoquímica, mezcla ternaria, miembro extremo, elemento conservativo, flujo local, Sierra Madre Oriental.

Torres-Rivera S.[1]
Torres- Hernández J. R.[1]
Posgrado en Geología
Facultad de Ingeniería
Universidad Autónoma de San Luis Potosí (UASLP),
Manuel Nava #5, Zona Universitaria
CP. 78240, San Luis Potosí, S.L.P., México
*Corresponding author: iq_soniatrivera@yahoo.com.mx

Ramos-Leal J. A.
Posgrado en Geociencias Aplicadas
Instituto Potosino de Investigación Científica y Tecnológica
A.C. (IPICYT), C. Presa San José No. 2055
Lomas 4ª. Sección, CP 78216
San Luís Potosí, S. L. P., México

Moran-Ramírez J.
[3]Cátedra CONACYT-UNAM, Geofísica
Circuito de la Investigación Científica s/n
Ciudad Universitaria, 04150
Coyoacán, Ciudad de México

Padilla-Sánchez L.
García-Arreola M. E.
Area de Ciencias de la Tierra
Facultad de Ingeniería
Universidad Autónoma de San Luis Potosí (UASLP)
Manuel Nava #5, Zona Universitaria
CP. 78240, San Luis Potosí, S.L.P., México

Carranco-Lozada S. E.
Instituto Politécnico Nacional, CECyT No. 17
León Guanajuato, México

Abstract

The hydrogeochemical characterization and water-rock interaction processes in the sub-basins of Santa Catarina and Ocampo-Paraíso in the Zona Media of San Luis Potosí have allowed identifying the types of groundwater. The results of the chemical analysis and the regional geological study show the possible rock-water interaction mechanisms. These results indicate that the composition of the groundwater in each of these basins reflects the dissolution of the carbonate and magnesium minerals of the carbonate rocks of Cretaceous age (El Abra Formation), by rainwater, and of the groundwater through a granular medium with a strong influence of the material of volcanic origin. The Ca-HCO_3, Ca-Mg-HCO_3, water type are modified during the groundwater flow by incorporation of Na^+ and SO_4^{2-} ions. The San Nicolás (sub-basin III) has covered by fluvial deposits in a climatic conditions of semiarid regions. The hydrogeochemical analysis of major ions, lithium and bromine allowed identifying that the extracted water from the region is a product of mixing process, involving three end-members (ternary mixture). The first, Santa Catarina (C_1), has the lowest concentrations of bromine and lithium and its recharge occur in the highest altitude land in the region, towards the Sierra de Álvarez. The second end member (C_2), displays high values of bromine, low in lithium and originates towards the Ocampo Paraíso Valley. The third end member (C_3), has low bromine concentrations, high in lithium, and comes from San Nicolás Tolentino area. The mixing percentages indicate that C_1 contributes 50%, C_2 gives 31% and C_3 adds 19% water to the system.

Key words: hydrogeochemistry, ternary mixture, end-member, conservative element, local flow, Sierra Madre Oriental.

Introduction

The chemical composition of the groundwater results from the interaction of rainwater with the dissolved rocks in the recharge zone (where it acquires part of its components). After filtration, it continues acquiring ions by its contact with the granular material through which it moves. The carbonate rocks undergo a process of chemical alteration by the action of rainwater that is combined with carbonic acid, this acid water dissolves the carbonate rocks, giving rise to a karstic landscape. In karst areas, the groundwater flow is characterized by high speeds, short residence times and significant water-rock interaction (Roback *et al.,* 2001). When the water infiltrates by small fractures, the solution goes deepening and widening these fissures, creating a network of ducts in the karstic rock. This process increases its secondary permeability and induces the formation of karst (Kiraly *et al.,* 1979; Andreo *et al.,* 2004; Antigüedad et al., 2008). In their evolution, groundwater may interact with other currents or groundwater flows, resulting in mixing of waters of different chemical composition due to natural or anthropogenic processes (Harpaz and Bear, 1963; Ramos *et al.,* 2007). A way of analyzing this phenomenon in generating isovalue curves of the different ions contained in the water, which allows to crossing directions of flow and zones where they can occur encounters of subterranean currents with different chemical compositions. Another way to organize the contributions of water mixtures in the groundwater flow is to use the conservative elements, frequently considered as tracers. The blends may be mainly binary or ternary; simultaneous mixtures with more than three end-members are uncommon to occur in nature whereas binary mixtures are very common. For example, to quantify the mixture of fresh and marine water have been widely explained in numerous publications (Apello and Postma, 1996; Generaux *et al.,* 2004; Wallick, 1981; Lee and Krothe, 2001; Abu-Jaber, 2001; Skalbeck *et al.,* 2002; Valentino and Stanzione, 2002). However, ternary mix models are less common. Rice and Hornberger (1998) evaluated the maximum flow contribution for groundwater in the US, and Generaux *et al*., (2004) evaluated groundwater mixtures by basin-to-basin transfer in the Costa Rica. Laaksoharju *et al.,* (1999), have addressed simultaneous mixtures with more than three end-members (EM). However, these authors did not explain how this process is carried out in nature. In addition, Douglas *et al.,* (2000) have reported that the mixing of three types of water with different chemical conditions and documented that this process can promote chemical reactions in an aquifer. In this work, we report that how chemical composition of water circulates through the volcanic rocks, limestone and alluvial fill in three different sub-basins. Therefore, the physicochemical characteristics, groundwater types, ion exchange processes and water-rock interaction of three different aquifers (San Nicolas Tolentino, Ocampo-Paraiso, Santa Catarina) are studied, which situated in the Zona Media of the state of San Luis Potosi, central Mexico. These findings contribute significantly due to their necessity in supplying drinking water as well as agricultural purposes. In addition, it provides valuable geochemical information for hydrogeology at local as well as a regional level.

Hydreogeological framework

The San Nicolás Tolentino aquifer (SNTA) located in the southern part of the state of San Luis Potosí (Figure 1) and it covers an exposed area of approximately 1,712.99 Km^2. In this region, the climate is dry, arid with an average annual rainfall of 300 mm (INEGI, 2002) and an average temperature of 25° C (INEGI, 2002).

The SNTA consists of three sub-basins, drained by the Santa Catarina (sub-basin I), Ocampo Paraíso (sub-basin II) and San Nicolás Tolentino (sub-basin III) River (Figure 1).

The Santa Catarina sub-basin (I), is an exorheic sub-basin with an area of 732.5 km^2, it is drained by the Santa Catarina River, which corresponds to 84.5% of the total area of the SNTA. Ocampo-Paraíso sub-basin (II) forms a sub-basin of 345.36 km^2. San Nicolás sub-basin (III) is an endorheic sub-basin of the area of 369.62 km^2 in which the Las Golondrinas dam is located.

Geology

The oldest stratigraphic unit that outcrop in the region is known as Guaxcama Formation of Lower Cretaceous (Neocomian-Aptian), which is composed of anhydrite, gypsum, and dolomite (Carrillo, 1971). This formation developed large diapiric structures (Carrillo-Bravo, 1971; Torres-Hernández, 1994), and is covered by the thick more than 1000m calcareous sequence of the Abra Formation. The youngest Cretaceous unit is the Cardenas Formation, which is constituted by a sequence of shales and sandstones. Its thickness is irregular, between 50 and 100m. The central training unit to consider in this work is the Abra Formation, it is construed by lagunar and reef facies. This unit is widely distributed, and carved for the most significant karst development. It thicknesses is up to 1,800 m (Zapata-Zapata and Pérez-Venzor, 1979).

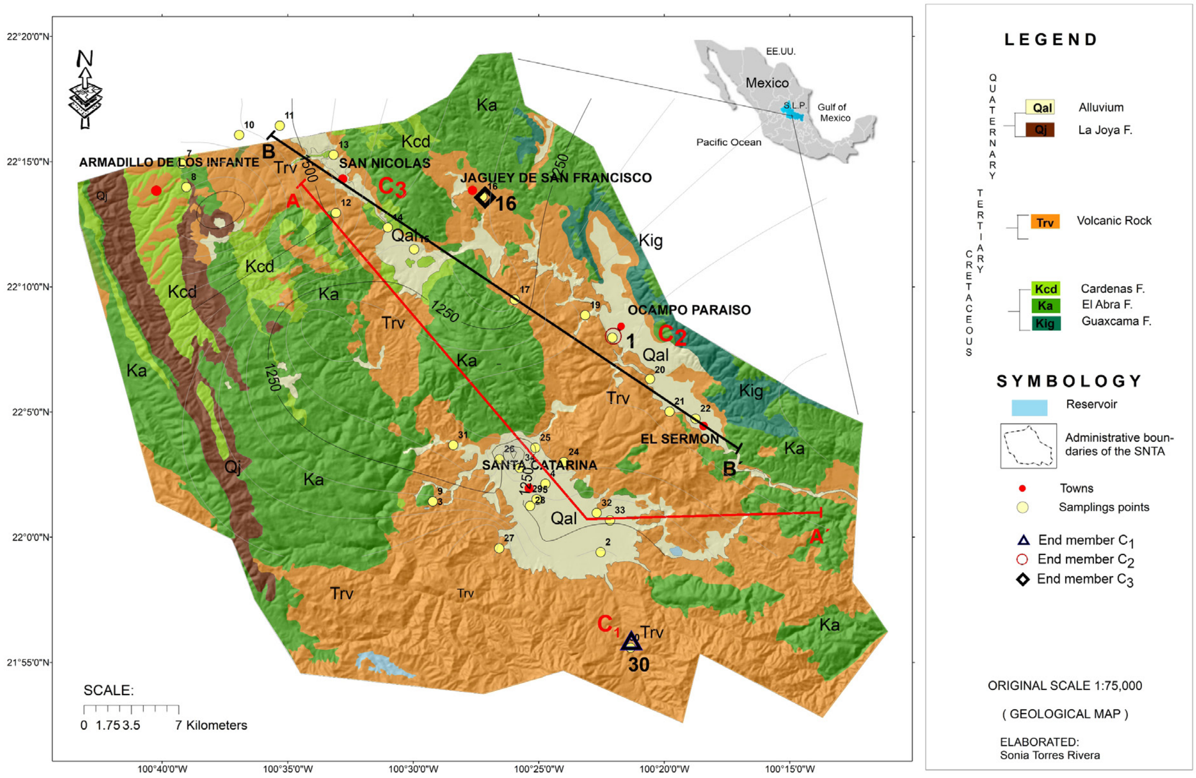

Figure 1. Location of the San Nicolas Tolentino Aquifer, regional geology of the study area and sampling points.

The Sierra de Alvarez (west of the studied area), constitutes the highest elevation in the region, and exposed as the slope foot facies (pre-reef deposits with 120 m of thickness), which is known as Tamabra Formation (López-Doncel, 2003).

The Cretaceous rocks are covered discordantly by volcanic rock sequences of andesitic and rhyolitic composition (Casa Blanca andesite, Santa María Ignimbrite, Portezuelo Latite, San Martin Avalanche, San Nicolás Formation, and Jagüey Formation; Torres Hernández *et al.,* 2010). This set of Paleogene (Oligocene) volcanic units is mainly distributed in the south-central part of the study area, with thicknesses greater than 140 m (Labarthe-Hernández *et al.,* 1982). Alluvium sediments cover all the units locally. Figure 2 shows a longitudinal geological section of the Peotillos, San Nicolás Tolentino and Santa Catarina valleys, looking towards the east (Figure 2). It can be observed that the Sierra de San Nicolás Tolentino is a remnant that belongs to a flank of an anticlinal that was eroded in Ocampo Paraiso sub-basin.

Hydrogeology

In the study area, aquifers are housed in granular material that partially covers Paleogene volcanic rocks, and carbonated rocks of the Cretaceous. Regionally, the largest aquifers are housed in limestone rocks.

The distribution of granular material is limited in the valleys, where it reaches only a few tens of meters, so its potential is not essential. The fracture medium represented by El Abra Formation that is the most crucial aquifer unit in the region because of its wide distribution and high thickness (Zapata and Pérez, 1979). This unit is exposed overall the high mountain, where it functions as a vital recharge zone, and in general, the flow goes from NW to SE, W to E, and in the southern part, of S to N (Figure 2). Since the origin of this unit belongs to the marine-platform and cover with reef and lagoon facies that provides it primary porosity whereas tectonic processes responsible for secondary porosity. In this región, El Abra Formation is very fractured, especially in the anticline nuclei where it develops numerous karstic structures (from sinkholes and uvalas to poljes). The processes of dissolution form cavities in the sub-soil, developing karstic caverns such as those of La Puente, El Ángel and La Catedral. Volcanic units with less distribution and thickness than limestones also function as aquifer units (Figure 2).

Methodology

Sampling and analysis

We collected a total of 34 water samples (26 correspond to wells, 8 to dugwells) whose distribution is shown in Figure 1, based on the "Groundwater Sample Protocol" (Armienta *et al.,* 1987; Deutsch, 1997). During sample collection, physical-chemical parameters were measured in an isolation cell, which has limited interaction with the atmosphere, preventing changes in its original composition (temperature, electrical conductivity, pH, dissolved oxygen, oxide reduction potential and alkalinity). All groundwater samples were collected in linear high-density polyethylene (HDLP) bottles for the analysis of more abundant ions. The bottles were previously washed three times, with plenty of deionized water. The sample was acidified right after collection to pH <2 with ultrapure nitric acid. The samples for the determination of anions were not acidified. The major ions were analyzed in the Laboratories of Chemical Analysis, Faculty of Engineering, Autonomous

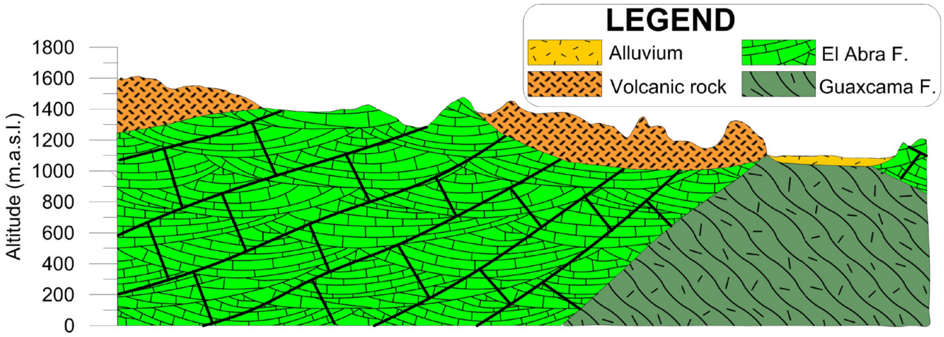

Figure 2. Longitudinal geological section of the Sierra de Peotillos, San Nicolas Tolentino and the Santa Catarina valley, facing east.

University of San Luis Potosi. The alkalinity was performed in situ by the titration method of Gran. For the analysis of Ca^{2+}, Mg^{2+}, Na^{+}, and K^{+}, the Atomic Flame Absorption Spectrometry (FAA) method was used. The chlorides were analyzed by the Argentometric method, the Sulphates, and Fluor with the Turbidimetric method. All chemical analyses show an ionic balance less than close to 5% allowed (Freese and Cherry, 1979).

Calculation of Mixtures

The end-members represent the highest and lowest concentrations of the system. The mixtures types can be binary and ternary; the former has been used to quantify mixtures of freshwater and marine waters (Apello and Postman, 1996; Genereux *et al*., 2002; Wallick, 1981; Abu-Jaber, 2001, Skalbeck *et al*., 2002; Valentino and Stanzione 2002). (Laaksoharju *et al*., 1999; Douglas *et al.,* 2000) showed multidimensional models with more than three water mixtures. As part of the methodology for the qualitative and quantitative analysis of a binary or ternary mixture, three end-members representing the evolution of the aquifer under study are identified.

The percentage calculation for each of the sub-basins was obtained using three equations with three unknowns; it is represented as a balanced equation:

$$C_t=C_1+C_2+C_3 \tag{1}$$

Where C_1 is the member associated with the local recharge in Santa Catarina, C_2 is the member associated with Ocampo-Paraiso, and C_3 is associated with the flows of San Nicolás Tolentino. C_1, C_2, and C_3 are unknown values, and C_w is equal to 1.

These components were determined with the equations of the mass balance of two conservative elements Li^{+} and Br^{-}:

$$C_wLi_w=C_1{}^*Li_1+C_2{}^*Li_2+C_3{}^*Li_3 \tag{2}$$

$$C_wBr_w=C_1{}^*Br_1+C_2{}^*Br_2+C_3{}^*Br_3 \tag{3}$$

(Equation 4) is obtained by substituting in Equation 2 in C_3 of Equation 1:

$$C_3=\frac{C_W(Li_W - Li_1)+(Li_2-Li_1)}{Li_3-Li_1} \tag{4}$$

C_1 substitute for Equation 3 in Equation 1 and obtain the Equation 5:

$$C_1=\frac{C_W(Br_W - Br_3)+C_2(Br_3-Br_2)}{Br_1-Br_3} \tag{5}$$

The only possible solution for C_2 is when C_w = 1. The other two components are calculated by clearing C_2 and substituting C_1 and C_3 in Equation 1 and the Equation is obtained:

$$C_2=C_T-C_1-C_3 \tag{6}$$

Results and discussion

The statistics of the chemical results of the groundwater samples are presented in Table 1. The results show that sub-basin I has a lower temperature, is rich in K^{+}, Ca^{2+}, HCO_3^{-}, Cl^{-}. Sub-basin II has an average temperature, lower ph, DO, Eh, Na^{+}, K^{+}, Ca^{2+} and higher Mg^{2+}. The sub-basin III presents higher T, pH, EC, DO, Eh, Na^{+}, SO_4^{2-} and lower Alkalinity, hardness, Cl^{-}.

Hydrogeochemical characterization

The chemical composition of groundwater is the result of continuous processes of interaction between precipitation water that infiltrates the subsoil and circulates through geological materials. Part of the chemical components is acquired in the recharge zone. Others are acquired along the pathway, captured by wells and in the discharge area as springs, resulting in different hydrogeochemical signatures.

Types of water

The Piper diagram (Piper, 1994) represents the end-members of each region and the classification of the different types of water (Figure 3). In the left part of the diamond, it displays mainly calcium-bicarbonate water. The upper part indicates dissolution of rock and middle part represents mixed waters where ion exchange can occur. On the left side of the diamond, is possibly the most evolved water, with dominance of the carbonate and sulfate ions.

In general, three families were obtained for the study area: calcium bicarbonate ($Ca-HCO_3$), sodium bicarbonate ($Na-HCO_3$), and only one exotic sample that is classified as calcium sulfated ($Ca-SO_4$) (Figures 3a and 3b).

Table 1. Statistics of the chemical results of sub-terrestrial water samples.

Sub-basin	T ºC	pH	EC µS/cm	DO %	Eh mV	TDS mg/L	Hard Total mg/L	Major Elements (mg/L) Na^+	 K^+	 Ca^{2+}	 Mg^{2+}	 HCO_3^-	 Cl^-	 SO_4^{2-}
I) SC														
MIN	24	7	309	2	234	200	61	24	6	16	2	134	7	14
MAX	31	9	1848	40	1816	1290	836	149	9	255	48	401	12	725
MEAN	27	8	610	18	516	419	210	51	6	62	13	217	9	118
STD	3	1	557	13	575	391	278	44	1	86	17	93	2	268
II) OP														
MIN	21	8	449	2	81	320	148	36	4	41	8	232	7	29
MAX	34	9	810	24	340	600	336	54	8	83	38	366	30	115
MEAN	24.6	7.8	566	7.4	282	422	221	41	6	58	19	280	12	48
STD	4	0.4	118	7.4	80	96	61	6	1	12	10	46	7	29
III) SNT														
MIN	16	8	1	6	275	400	205	27	4.1	59	8.1	267	11	2
MAX	26	8	808	20	344	600	301	77	25	90.1	22.3	390	35	53
MEAN	21	8	545	10	318	447	247	44	9	77	13	322	18	32
STD	3.1	0.2	208.6	4.4	20.6	66.0	29.3	15.4	5.9	10.1	5.6	35.7	8.3	16.1

I) Santa Catarina sub-basin (SC); II) Ocampo Paraiso sub-basin (OP) and III) San Nicolas Tolentino sub-basin (SNT)

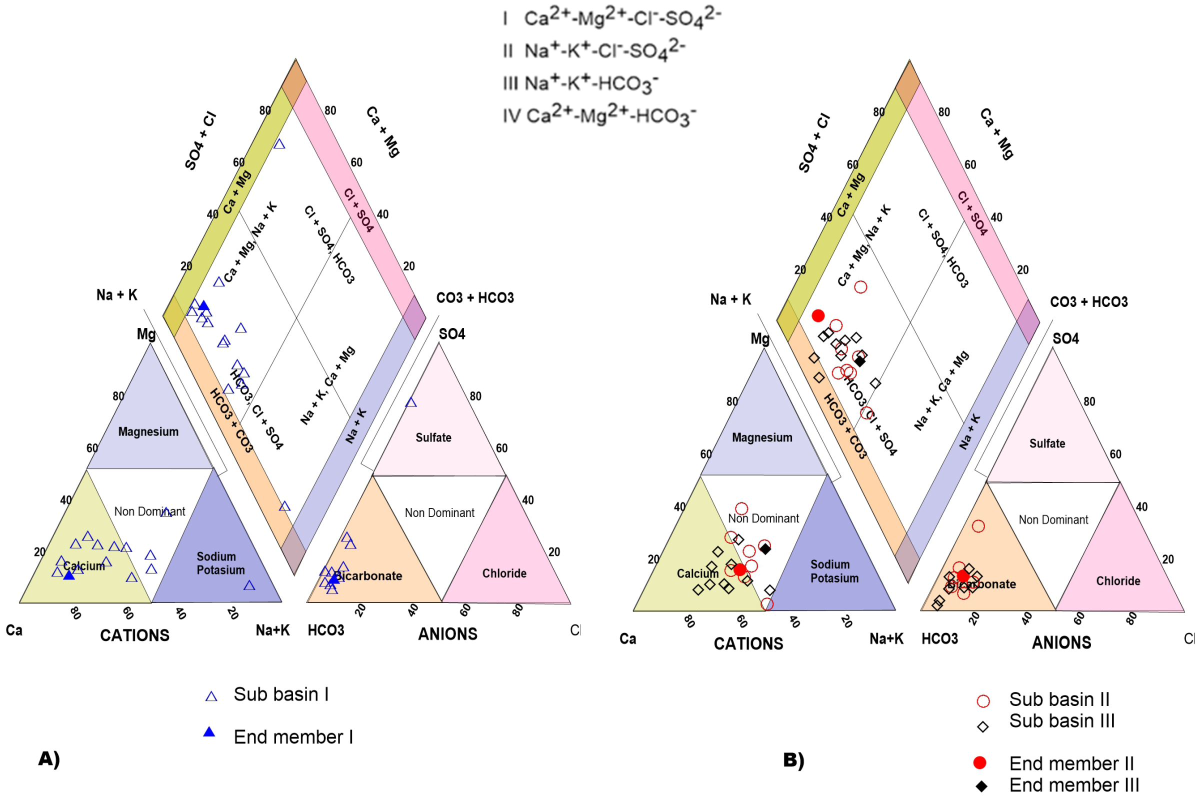

Figure 3. Piper diagrams: A) sub-basin I, Santa Catarina. B) sub-basins II and III Ocampo Paraiso and San Nicolas Tolentino for groundwater.

In Santa Catarina sub-basin I, two aquifers have been detected (Torres-Rivera, 2012) that is known as free and confined, respectively. The water recharge area of the free aquifer is influenced by the Santa Catarina and San Martín rivers. The predominant water family is Ca-Na-HCO_3 and Ca-HCO_3 (Figure 3A). These water families reflect that the most important source corresponds to the Santa Catarina River. Their main salt content corresponds to the interaction of the water with calcareous Ca-HCO3 family and movement of the water in the granular material, which consists predominantly products of the San Martín Avalanche (Torres-Hernández *et al.,* 2010; Torres-Rivera, 2012). The mixing of the Ca-HCO_3 water type with volcanic rocks interaction generates Ca-Na-HCO_3 family. A single sample corresponds to Sulfate-Bicarbonate-Calcium-Magnesium composition, and additionally, it has 1290 mg/L of TDS; reflecting above all a much higher salt enrichment than all the other samples analyzed in this valley. This high value is considered as evidence that it reflects a regional flow and corresponds to a confined aquifer (Torres-Rivera, 2012). It also represents a confined aquifer, since the well that captures these waters penetrated beneath a thick ignimbrite layer (Santa María Ignimbrite), which functions as a seal rock of the same.

The waters family in the sub-basin II of Ocampo-Paraíso, is Ca-Na-HCO_3, reflecting above all the interaction of the currents with calcareous rocks and the incorporation of the sodium liberated from the volcanic clasts in the granular medium.

In sub-basin III of San Nicolás, the Ca-Na-HCO_3 and Ca-Na-HCO_3-SO_4 families were documented at the south of the Morenos town. This type of water reflects the interaction of the water with limestone rocks, gypsum, and ion exchange in the valleys where there is the presence of clay materials.

Hydrogeochemical processes with Gibbs diagrams

To identify some hydrogeochemical processes that occur in the groundwater, diagrams are used such as Gibbs diagrams (Gibbs, 1970), which was developed for surface water studies; however, in recent decades it has been used for the study of groundwater. The three main mechanisms that control the chemistry of surface water can be defined as the domain of atmospheric precipitation (rain), the domain of the rock, and domain of the evaporation-crystallization process (Gibbs, 1970). The Gibbs diagram was elaborated with the chemical data (anions and cations) of the groundwater samples (Figure 4).

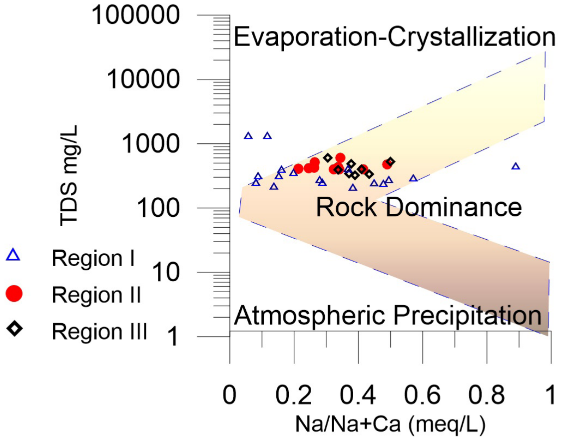

Figure 4. Gibbs diagram, the main evolutionary process that we identify with this diagram is the interaction rock water; the yellow arrow indicates the direction of the evolution of groundwater.

Based on Figure 4, we can infer that during its evolution, the water was influenced mainly by the water-rock interaction and a little evaporation due to the evaporation seems to have been dominant only in two samples. When the water infiltrates the subsoil, the water-rock interaction begins, the water from the recent infiltration has fewer chemical components; while the greater distance traveled, the residence time, the more significant the physical and chemical components increase; this evolutionary behavior, can be seen in Figure 4. Member I is very close to the vertical axis, which is associated with the water in the recharge zone while member II is away from the vertical axis because of its significant evolution.

Flow Systems

The increase of chemical components during the evolution of the groundwater can be observed in the Mifflin diagram (Mifflin, 1968) and uses hydrogeochemical indicators ($Na^+ + K^+$ + vs. $Cl^- + SO_4^{2-}$) to understand the evolution of groundwater and establish the different types of water flows (Figure 5). It is divided into three zones, and the area closest to the origin is due to the low circulation and short residence time of the water, the samples in this area are associated with the recharge (local flow). In the next zone, the concentrations increase and may be associated with a long-distance or longer residence time (intermediate flow).

Finally, the higher concentration is associated with more significant water-rock interaction and higher evolution of the groundwater (regional flow). In the study area, there are two types of water flow, one local and the other intermediate (Figure 5).

Hydrogeochemical Section

During its pathway, the groundwater interacts with the different materials, which results in the increase of the chemical components and in some cases, the decrease of these, due to the mixture with water of recent infiltration. To corroborate the water-rock interaction and mixtures a hydrogeological-hydrogeochemical, this section was elaborated.

The hydrogeochemical section is 40.5 km, begins in the Armadillo de los Infante, where volcanic rocks contact with the limestones and known as El Abra Formation, which cross the Ocampo valley of volcanic rocks and finally, cuts a valley where gypsum from the Guaxcamá Formation are found a few meters deep (Figure 6). (This section is only justified for the valleys of San Nicolas Tolentino and Ocampo Paraiso).

For the first sub-basin, the Ca-Na-HCO_3 waters reflect the primary interaction with calcareous rocks of the El Abra Formation that crops out in the Sierra de Álvarez, which are partially dolomitized and contain varying amounts of magnesium in their dominant composition of Ca-HCO_3. Ca-HCO_3 its transit through the granular material that fills the Graben de Peotillos (López-Doncel *et al.,* 2001) could print its sodium content indicates that this filling was deposited as a lacustrine fluvial material, which is due to having a shallow water tie. The location of the valley in an environment with medium to intense evaporation could include to some extent sodium. Another possible source of this sodium would be the decomposition of sodium plagioclase in the ignimbrite rocks, which interacts with the water currents and mix into the San Nicolas Tolentino river.

To the south of the Morenos town, where the San Nicolás River breaks its trajectory. As mentioned above, the first family waters (Ca-HCO_3) acquire a character of Bicarbonate-Sulphated, perhaps due to the nearby influence of the gypsum that emerges in El Potrero anticline.

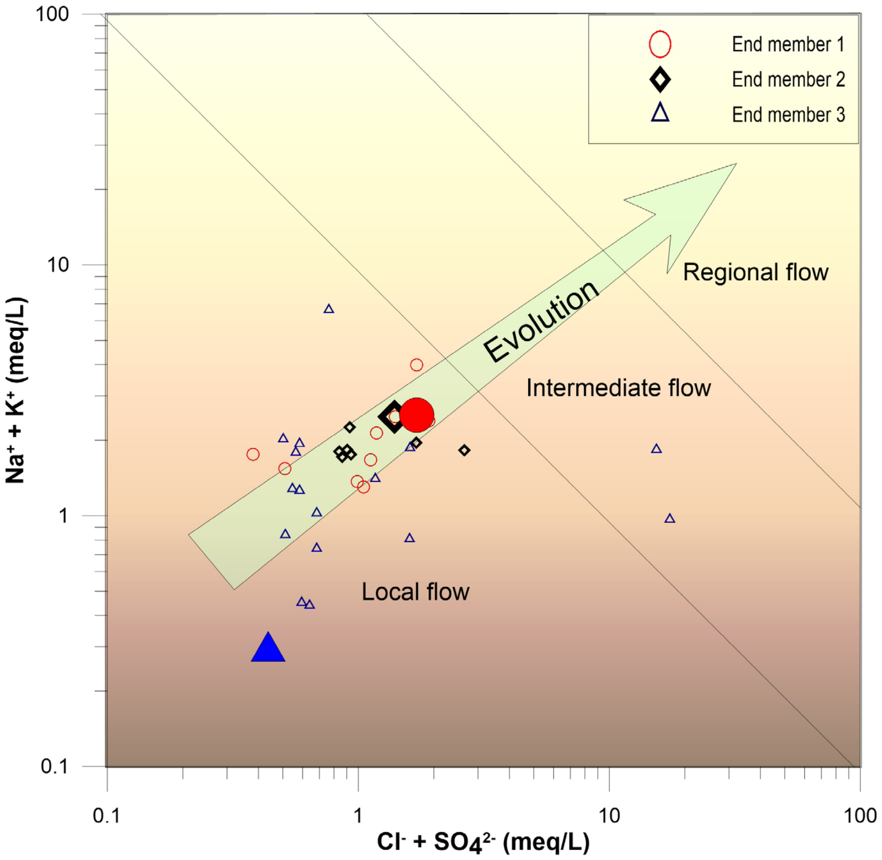

Figure 5. Mifflin diagram, classifies the water according to its evolution.

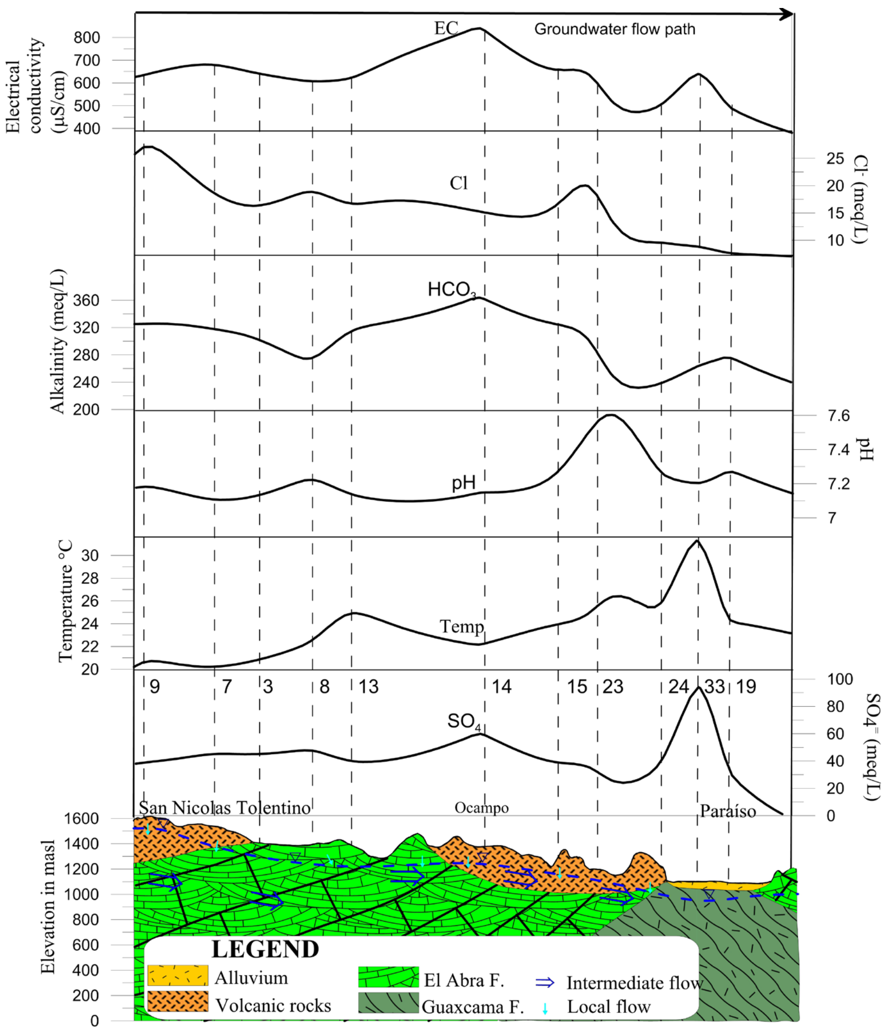

Figure 6. Hydrogeochemical section of Armadillo de los Infante to Paraiso; the numbers indicate several use; the discontinuous blue line indicates the piezometric level.

The physical parameters of sub-basins II and III, in the Armadillo de los Infante reveal that the electrical conductivity in the waters is approximately 650 µS/cm, along the hydrogeochemical section. The highest point is located at the center of the section in Paraiso, due to the interaction of the groundwater with the limestones whereas lowest point at the end of the section in Ocampo Paraiso town, because there is a mixture of local recharge water through the volcanic rocks. The concentration of chlorides is high at the beginning of the section, with values of 25 mg/L due to the agricultural activity that takes place in that area. Concentrations tend to decrease toward Ocampo Paraíso where it is possible for groundwater to mix with waters of recent infiltration. The alkalinity starts with values of 320 mg/L in Armadillo de los Infante and increases in the Ocampo zone due to the interaction of the water with the limestones, decreases to 240 mg/L at the end of the section due to mixing with water from recent infiltration (Figure 7).

The pH is 7.2 at the beginning and maintains little variation until Ocampo. However, it increases up to values of 7.6 and end with values of 7.2. The temperature starts at 20 °C and increases throughout the section until reaching 31 °C towards the end of the section in Paraiso. Sulfates begin with values close to 40 mg/L, increase slightly towards Ocampo town (60 mg/L) and on the Paraiso town increase to reach 100 mg/L; this increase can be related to the interaction of water with gypsums, which generates an exothermic reaction and this is congruent with the temperature anomaly in Paraiso.

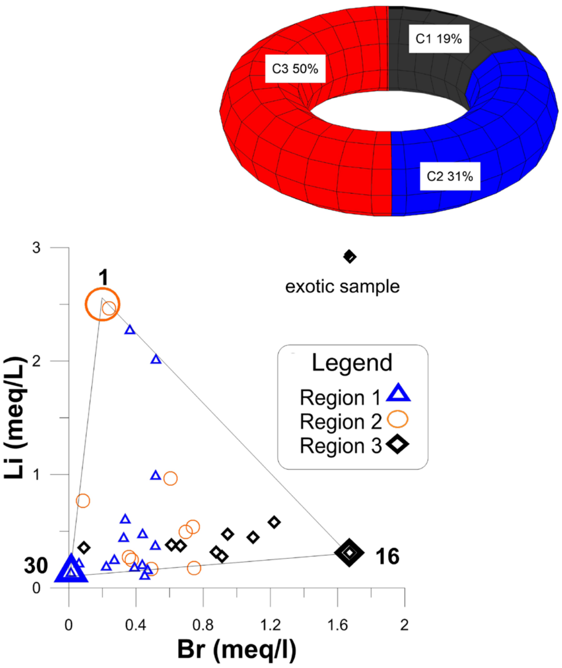

Figure 7. Scatter diagrams of conservative elements (Br- and Li-) for the study area.

Origin of the end-members and mixtures

To evaluate the contributions to a hydrogeological system, the mixture models are used, for which it is necessary to identify the end-members representative of each region.

Based on the scatter plot of the conditional elements i.e., Li and Br, which do not react chemically with the environment during the evolution of groundwater are used in the present study. The study represents three end members (C_1, C_2, C_3) and corresponds to a ternary mixing. Two members are the most evolved and corresponds to intermediate flows while third one is associated with local recharge.

In Figure 7, a ternary mixing is identified, which is formed by (C_1) associated with sub-basin I (Santa Catarina) for local recharge, (C_2) associated with sub-basin II (Ocampo-Paraíso) and (C_3) associated with the flow of sub-basin III (San Nicolás Tolentino). This figure display a triangle, in whose vertices the end-members are located. The remaining samples are between the limits of the mixture lines and are considered as a mixture of the fractions of the end member. Any water sample from the system can be generated utilizing the three end-members.

Sub-basin I, is represented by sample 30, which located to the south of the study area (Santa Catarina), towards the Sierra de Álvarez (Figure 1) and associated with local recharge and content low values of Cl^-, SO_4^{2-}, Br^-, and Li^+. In this sample the lowest values were measured for Cl^- (0.22 meq/L), Li^+ (0.128 meq/L) and 0.012 meq/L of Br^- (Figure 7); the measured temperature was of 14 °C, with a pH of 6.5. The type of this member is $Ca-HCO_3$.

Sub-basin II, sample 1, which corresponds to an intermediate flow, is located at the eastern-center of the study area in the Ocampo-Paraíso basin (Figure 1). The temperature measured in this sample was about 24.4°C and Cl^- concentrations of 0.84. meq/L; 2.46 meq/L of Li^+; and, 0.24 meq/L of Br^- (Figure 7). The water type of this member is $Na-K-HCO_3$.

Sub-basin III, is represented by sample 16. This water sample represents an intermediate flow and is located towards the north of the study area, towards the Jagüey de San Francisco, belonging to the basin of San Nicolás Tolentino (Figure 1). It has high temperatures of 20.5°C and have concentrations of Cl^- of 0.819 meq/L; 0.312 meq/L of Li^+; and high concentrations of Br^- (1.67 meq/L) (Figure 7). This type of water is $Na-K-HCO_3$.

In Table 2, C1 contributes 50 %, C2 contributes 31%, and C3 contributes 19% of water to the system (Table 2).

Conclusions

- The aquifer receives its recharge water that drains through flat platform rocks (El Abra Formation), gypsum, anhydrite (Guaxcama Formation) and volcanic rocks that delimit the aquifer.
- Three different types calcium bicarbonate ($Ca-HCO_3$), sodium bicarbonate ($Na-HCO_3$), calcium sulfate ($Ca-SO_4$) waters were obtained.
- A local and an intermediate regional flow were identified, where each system has a representative sample used as an extra limb.
- A ternary mixture and water-rock interaction processes were identified in the study area.
- The system is fed by three essential regions. C1, C2 and C3 contributes 50%, 31% and 19%, respectively of water to the system.

Table 2. Mixing fractions considering three extreme members (samples 30, 1 and 16) for the groundwater of the Zona Media of San Luis Potosí.

Sample	C1	C2	C3	CT
1	0.00	1.00	0.00	1.00
2	0.01	0.20	0.79	1.00
3	0.63	0.24	0.13	1.00
4	0.74	0.25	0.01	1.00
5	0.64	0.17	0.19	1.00
6	0.35	0.31	0.33	1.00
7	0.27	0.64	0.09	1.00
8	0.44	0.54	0.02	1.00
9	0.35	0.55	0.11	1.00
10	0.44	0.52	0.04	1.00
11	0.15	0.71	0.14	1.00
12	0.87	0.03	0.09	1.00
13	*	*	*	*
14	0.57	0.35	0.08	1.00
15	0.54	0.38	0.07	1.00
16	0.00	0.00	1.00	1.00
17	0.48	0.39	0.13	1.00
18	0.58	0.44	0.00	1.00
19	0.44	0.42	0.14	1.00
20	0.72	0.28	0.00	1.00
21	0.72	0.01	0.27	1.00
22	0.75	0.20	0.05	1.00
23	0.75	0.21	0.03	1.00
24	0.63	0.29	0.08	1.00
25	0.81	0.15	0.04	1.00
26	0.40	0.26	0.35	1.00
27	0.00	0.09	0.91	1.00
28	0.74	0.26	0.00	1.00
29	0.77	0.23	0.00	1.00
30	1.00	0.00	0.00	1.00
31	0.94	0.02	0.03	1.00
32	0.73	0.27	0.00	1.00
33	0.86	0.13	0.01	1.00
34	0.71	0.17	0.12	1.00

References

Abu Jaber, N., 2001, Geochemical evolution and recharge of the shallow aquifers at Tulul al Ashiqif, NE Jordan: Enviromental Geology, vol. 41, 372-383pp.

Antigüedad, I., Morales, T., Uriarte, J.A., 2008, Los acuíferos kársticos. Caso del país Vasco. Grupo de Hidrogeología. Geodinamica Saila. Universidad del país Vasco-Euskal Herriko. 8pp.

Andreo, B., Vadillo, I., Carrasco, F., Neukum, C., Jiménez, P., Goldscheider, N., Hötzl, H., Vías, J.M., Pérez, I. y Göppert, N., 2004, Precisiones sobre el funcionamiento hidrodinámico y la vulnerabilidad a la contaminación del acuífero kárstico de la Sierra de Líbar (provincias de Málaga y Cádiz, sur de España) a partir de un ensayo de trazadores. Revista de la Sociedad Geológica de España, 17 (3-4): 187-197pp.

Apello, C.A., Postma, D., 1996, Geochemistry, Groundwater and Pollution: Rotterdam, Netherlands, A.A. Balkema, 536 pp.

Armienta, E.K., Zamora y Juárez, F., 1987, Manual para el análisis químico de aguas naturales, en campo y laboratorio. Comunidades técnicas. Serie Docencia y Divulgación, Num. 4. México D.F. Instituto de Geofísica de la UNAM, 86pp.

Carrillo-Bravo, J., 1971, La Plataforma Valles - San Luis Potosí: Boletín de la Asociación Mexicana de Geólogos Petroleros, vol. 23, 1-102pp.

Deutsch, W.J., 1997, Groundwater Geochemistry: fundamentals and applications to Contamination: New York, CRP-Press 232pp.

Douglas, M., Clark, I.D., Raven, K., Bottomley, D., 2000, Groundwater mixing dynamics at a Canadian Shield mine: Journal of Hydrology, 235, 88-103pp.

Freeze, R.A., and Cherry, J.A., 1979, Groundwater: Englewood Cliffs, NJ, Prentice-Hall, 604 pp.

Genereux, D., 2004, Comparison of naturally-occurring chloride and oxygen-18 as tracers of interbasin groundwater transfer in low land rain forest, Costa Rica: Journal of Hydrology, 295(1-4), 17-27pp.

Gibbs, R.J., 1970, Mechanisms controling world water chemistry: American Association for the Advancement of Science, New Series, vol. 170, No.3962, 1088-1090pp.

Harpaz, Y. and Bear, J., 1963, Investigations on mixing of waters in subsoil storage operations, International Association Scientific Hydrology, vol. 64, 132-153pp.

Instituto Nacional de Estadística y Geografía (INEGI), 2002, Estudio Hidrologíco del estado de San Luis Potosí.

Kiraly, L., y Müller, I., 1979, Heterogeneité de la perméabilité et de alimentation dans le karst, effect sur la variation du chimisme des sourceskasrstiques. Bull. Center Hydrogéol. Neuchatel, vol. 3, 237-285pp.

Laaksoharju, M., Skarman, C., Skarman, E., 1999, Multivariate mixing and mass balance (M3) calculations, a new tool for decoding hydrogeochemical information: Applied Geochemistry, vol.14, 861-871pp.

Labarthe Hernández, G., Tristán González, M., Aranda Gómez, J.J., 1982, Revisión estratigráfica del Cenozoico de la parte central del Estado de San Luis Potosí. Universidad Autónoma de San Luis Potosí, Instituto de Geología y Metalurgia, Folleto Técnico No. 85, 205 pp.

Lee, E.S., Krothe, N.C., 2001, A four component mixing model for water in a karst terrain in south central Indiana, USA using solute concentration and stable isotopes as tracers: Chemical Geology, 179, 129-143pp.

López-Doncel, R.A., 2003. Formación Tamabra del Cretácico Medio de la porción central del margen occidental de la Plataforma Valles-San Luis Potosí, Centro-Noreste de México. Revista Mexicana de Ciencias Geológicas Vol. 20, n. 1: 1-19.

López-Doncel, R. A., Soto-Araiza, R. G., Dircio-Castro, D., 2001, Carta Geológico Minera, Peotillos F14-A75 San Luis Potosí, Servicio Geológico Mexicano

Mifflin, M.D., 1968, Delineation of groundwater flow systems in Nevada, Report series H-W., Desert research Institute Technical, vol. 4, 111pp.

Piper, A.M., 1994, A graphic procedure in the geochemical interpretation of water analyses. Am. Geophysical Union Trans. Vol. 25, 914-923p.

Ramos Leal J.A., Martínez Ruiz V.J., Rangel Méndez J.R. y Alfaro de la Torre M.C., 2007, Hidrogeological and mixing process of waters in aquifers in arid regions: a case study in San Luis Potosí Valley, Mexico. Environ Geol 53:325-337pp.

Rice, K.C., Hornberger, G.M., 1998, Comparation of hydrochemical tracers to estimate source contributions to peak flow in a small, forested, head water catchment: Water Resources Research, 34(7), 1755-1766pp.

Roback, R.C., Johnson, T.M., McLing, T.L., Murrell, M.T., Luo, S., Ku, T.L., 2001, Uranium isotopic evidence for groundwater chemical evolution and flow patterns in the eastern Snake River Plain Aquifer, Idaho: Geological Society of America Bulletin, 113 (9), 1133-1141pp.

Skalbeck, J.D., Shevenell, L., Widmer, M.C., 2002, Mixing of thermal and non thermal waters in the Steamboat Hills area, Nevada, USA: Geothermics, 31, 60-90pp.

Torres-Hernández, J.R., Rodríguez-Ríos, R., Barboza-Gudiño, J.R., Saucedo-Girón, R., Tristán-Capetillo, L.C., García-Pérez, K., 2010, Cartografía Golόgico Minera Santa Catarina F14-A-85 San Luis Potosí, Servicio Geológico Mexicano.

Torres-Rivera, S., 2012 Caracterización hidrogeoquímica y direcciones de flujo de agua subterránea en el acuífero de San Nicolás Tolentino. Tesis de Maestría. Maestría en Ciencias en Geología Aplicada, Facultad de Ingeniería de la Universidad Autónoma de San Luis Potosí. 105 p.

Valentino, G.M., Stanzione, D., 2002, Source process of the thermal waters from the Phlegraean Fields (Naples, Italy) by means of selected minor and trace elements distribution: Chemical Geology, 245, 245-274pp.

Wallick, E.I., 1981, Chemical evolution of groundwater in a drainage basin f Holocene age, east-central Alberta, Canada: Journal of Hydrology, 54, 245-283pp.

Zapata Zapata, J.L., Pérez Venzor, J.A., 1979, Cartografía Geológica Hoja Peotillos, S.L.P, Universidad Autónoma de San Luis Potosí, Instituto de Geología y Metalurgia, Folletos Técnicos N.63, 30pp.

Geofísica Internacional (2019) 58-4: 259-277

Original paper

Structural Interpretation and Depth Estimation from Aeromagnetic Data of Abigi-Ijebu-Waterside area of Eastern Dahomey Basin, Southwestern Nigeria

Osinowo, Olawale Olakunle, Adabanija, Moruffdeen A. and Adewoye, Oluwatoyin Adebayo

Received: May 21, 2018; accepted: September 03, 2019; published on line: October 01, 2019

Resumen

Los datos de alta resolución aeronáutica (HRAM) de la costa de Abigi-Ijebu en la parte oriental de la cuenca Dahomey en el sudoeste de Nigeria se filtraron, transformaron, mejoraron, analizaron e interpretaron en términos de estructuras, geometría del basamento y espesor sedimentario, para evaluar el potencial de prospección petrolera de este sector de la cuenca Dahomey, así como proporcionar información relevante que podría apoyar la campaña de exploración de hidrocarburos del descuidado brazo oriental de la cuenca Dahomey, que recientemente ha demostrado ser prolífico con el descubrimiento de yacimientos de petróleo Aje y Ogo en la parte costera de la cuenca . Los datos de HRAM se filtraron para eliminar el ruido cultural y de fondo, continuaron hacia arriba para suprimir los efectos de fuentes poco profundas y mejorar el efecto de roca del sótano que emana de fuentes relativamente más profundas. Los datos también se redujeron al polo a baja latitud para simplificar las anomalías magnéticas y para enfocar los picos de las anomalías positivamente simétricas con respecto a las fuentes geológicas correspondientes. Se aplicaron filtros derivados para detectar y mejorar las firmas magnéticas alineadas de forma preferencial que reflejan el marco estructural del área de estudio. El análisis espectral radial y las técnicas de ponderación de profundidad de Euler se emplearon para determinar la profundidad de las fuentes magnéticas que generaron la topografía del basamento y, por lo tanto, el espesor de las rocas sedimentarias que cubren las rocas cristalinas.

Los derivados y filtros derivados de inclinación mejoraron y delinearon varias estructuras regionales lineales, algunas de las cuales tienen más de 15 km de longitud y una tendencia principalmente a lo largo de la dirección NE - SW. El análisis espectral y las soluciones de ponderación de profundidad de deconvolución de Euler 3D indican que la profundidad en la parte superior de las anomalías magnéticas varía desde alrededor de 100 m por encima del dato de referencia de Minna hasta más de 2,0 km por debajo del dato. La topografía del basamento revelada por las parcelas de solución de Euler indica rocas del basamento de la corteza gradual y suavemente deprimidas que pueden ser ayudadas por fallas regionales que gradualmente descendieron o deprimieron las rocas de la corteza hacia el sur para aumentar el acomodo de los sedimentos. Por lo tanto, esto sugiere un aumento en el potencial de prospección de hidrocarburos hacia el sur del área de estudio, especialmente en el mar abierto y más profundamente en el Océano Atlántico.

Palabras clave: ángulo de inclinación; Filtros derivados; Deconvolución de Euler: Topografía del basamento; Potencial de hidrocarburos; Dahomey.

Osinowo, Olawale Olakunle
Adewoye, Oluwatoyin Adebayo
Department of Geology
University of Ibadan
Ibadan, Nigeria

Adabanija, Moruffdeen A.
Earth Sciences Department
Ladoke Akintola University of Technology
Ogbomoso, Nigeria
*Corresponding author: wale.osinowo@ui.edu.ng, olawale.osinowo13@alumni.imperial.ac.uk

Abstract

High Resolution Aeromagnetic (HRAM) data of Abigi-Ijebu waterside in eastern part of Dahomey Basin southwestern Nigeria were analyzed and interpreted in terms of structures, basement geometry and sedimentary thickness to evaluate the petroleum potential of this sector of the Dahomey Basin as well as provide relevant information that could support the hydrocarbon exploration campaign of the neglected eastern arm of the basin, which has lately proved prolific with the discovery of Aje and Ogo oil fields in the offshore part of the basin. The HRAM data were filtered to remove cultural and background noise, upwardly continued and reduced to pole at low latitude to simplify and focus the peaks of magnetic anomalies positively symmetrical over corresponding geologic sources. Derivative filtering delineated and enhance preferentially aligned magnetic signatures that reflect the structural framework of the study area. Radial spectral analysis and Euler deconvolution depth weighting techniques were employed to determine depth to magnetic sources which generated the basement topography and thus the thickness of sedimentary rocks overlying the crystalline rocks.

The derivatives and tilt derivative filters enhanced and delineated several linear regional structures, some of which are over 15 km in length and trend mainly along NE - SW direction. Spectral analysis and 3D Euler deconvolution depth weighting solutions indicate that the depth to the top of magnetic anomalies ranges from around 100 m above the Minna reference datum to over 2.0 km below the datum. The basement topography as revealed by the Euler solution plots indicate gradual and gently depressing crustal basement rocks which may be aided by regional faults that gradually stepped down or depressed the crustal rocks southward for increase sediment accommodation. This therefore suggests increase in the hydrocarbon prospect potential southward of the study area, especially in the offshore and deeper into the Atlantic Ocean.

Key words: tilt angle; derivative filters; euler deconvolution; basement topography; hydrocarbon potential; dahomey basin.

Introduction

Recent advancements in geophysical data acquisition technology, improved flight specifications and acquisition of data very close to the ground surface (< 80 m – 150 m) have greatly improved the capacity of aeromagnetic survey to generate High Resolution Airborne Magnetic (HRAM) data which provide detailed geological information required for mapping subsurface geological structures (Reeves, 2005). HRAM data have also proved very successful in mapping topographical features of the subsurface basement surface which could influence the structure of overlying sediments. Large-scale aeromagnetic survey has gained relevance in locating regional faults and shear zones having huge potential as hosts for varieties of economic minerals, especially the epigenetic and stress-related mineralization (Paterson & Reeves, 1985). The method through determination of depth to basement rocks has also proved very useful in estimating the thickness of sedimentary pile above crystalline basement rocks (Reid *et al*., 1990; Nabighian & Hansen, 2005).

In this research, high-resolution airborne magnetic data acquired for the Nigerian Geological Survey Agency (NGSA) by Fugro Geophysical Limited in 2007 were analyzed, enhanced and interpreted to delineate structural framework and investigate the nature of the subsurface basement topography, in addition to expressing the geology and causes of the magnetic anomalies observed in the Abigi - Ijebu waterside area in southwestern Nigeria. The study area is situated in Abigi - Ijebu waterside in southwestern Nigeria, it is located on the flank of the eastern part of the Dahomey Basin, it is bordered in the south by the Atlantic Ocean and lies between longitude 4°00’E and $4°30^1$ E; and latitude $6°20^1$ N and $7°00^1$ N (Figure 1).

Abigi in Ijebu waterside was in the past explored for its hydrocarbon potential mainly because of its proximity to Escravos in western Niger Delta, southern Nigeria and also for the occurrence of huge deposit of tar sands (bitumen), the deposit has been reported as the second largest deposit in the world, after that of Alberta in Canada. This study therefore seeks to investigate the subsurface of Abigi-Ijebu waterside and environs through the analyses of aeromagnetic data of the area with the object of providing information that could generate requisite information likely to further aid the exploration campaign of that section of the Dahomey Basin, especially with the success stories of oil discovery in Aje and Ogo fields offshore and western end of the Nigerian sector of the Dahomey Basin in southwestern Nigeria.

Geology of the Study Area

The Dahomey Basin forms one of the series of West African Atlantic marginal basin that were initiated during the period of rifting in the late Jurassic to early Cretaceous (Omatsola & Adegoke, 1981). During the rifting stage, there was basement fracturing and initial separation between the African and South American plates (Brownfield & Charpentier 2006). Several marginal basins were developed at this time resulting to block faulting, fragmentation and subsidence on the central Paleozoic basement rock (Omatsola & Adegoke, 1981).

The basin stretches along the coast of Nigeria, Benin Republic, Togo and Ghana along the margin of the Gulf of Guinea. It is separated from the Niger Delta by a subsurface basement high referred to as the Okitipupa Ridge. Figure 1 presents the geology of the study area while the insert is the geologic map of the Nigerian sector of the Dahomey Basin with adjacent crystalline basement rocks. The geology of the study area depict that of a transition zone between the Basement Complex rocks of southwestern Nigeria in the north and the sedimentary units that unconformably overly the depressed part of the crystalline rocks at the edge of the Dahomey Basin, around Abigi-Ijebu waterside area of the southwestern Nigeria. The Basement Complex rocks has been reported by various authors to comprise largely of a metasedimentary series with associated minor metaigneous rocks, which have been variably altered to migmatitic gneisses, and the Older Granites suite of both intrusive and replacement origin (Jones & Hockey, 1964: Grant, 1971; Burke *et al.*, 1976). The northern part of the study area is dominated by crystalline rocks such as biotite granite gneisses and granodiorite, migmatite gneiss, quartz-feldspartic granulites, undifferentiated schist, quartz-schist and quartzites (Figure 1) (Burke *et al.*, 1976).

In the southern part of the study area, sedimentary rock units defined through a stratigraphic setting of the eastern Dahomey Basin, as put together by several authors, such as Adegoke (1969), Ogbe (1970), Kogbe (1974), Billman (1976), Omatsola & Adegoke (1981), Ako *et al.*, (1980), Okosun (1990) and Idowu *et al.*, (1993), presented five (5) lithostratigraphic formations from the Cretaceous to Tertiary ages (Figure 1). The succession from the oldest to the youngest includes Abeokuta Group, Cretaceous in age and consists of Ise, Afowo and Araromi Formations as members. The Abeokuta group is immediately overlain in quick succession by Paleocene Ewekoro Formation, Eocene Ilaro Formation, Coastal Plain Sands and the Recent Alluvium in that order of succession. Table 1 presents the stratigraphic column of eastern Dahomey Basin as compiled by Obaje (2009).

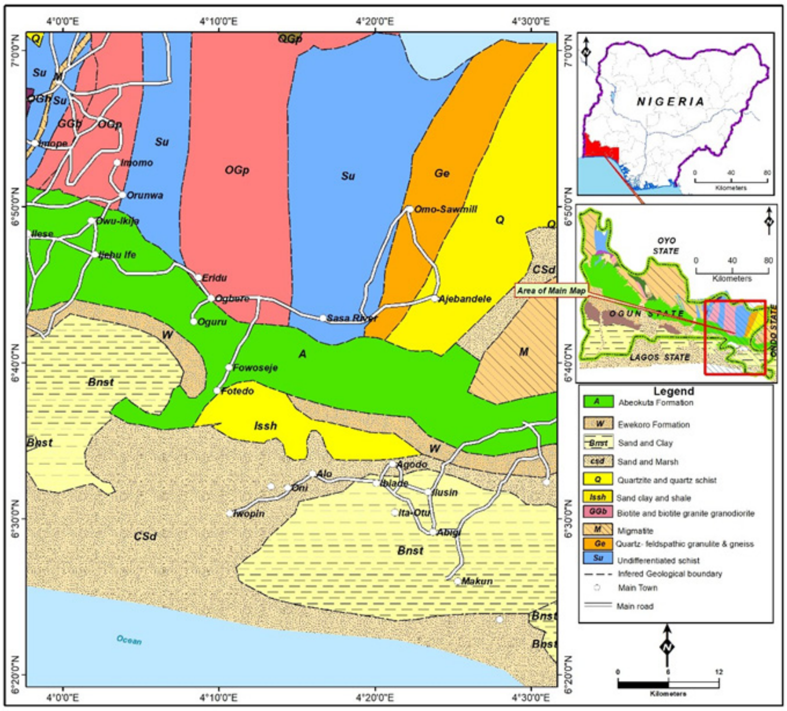

Figure 1. Geological map of the study area (NGSA, 2009).

Table 1 Stratigraphic Column of the Eastern Dahomey Basin (Obaje, 2009).

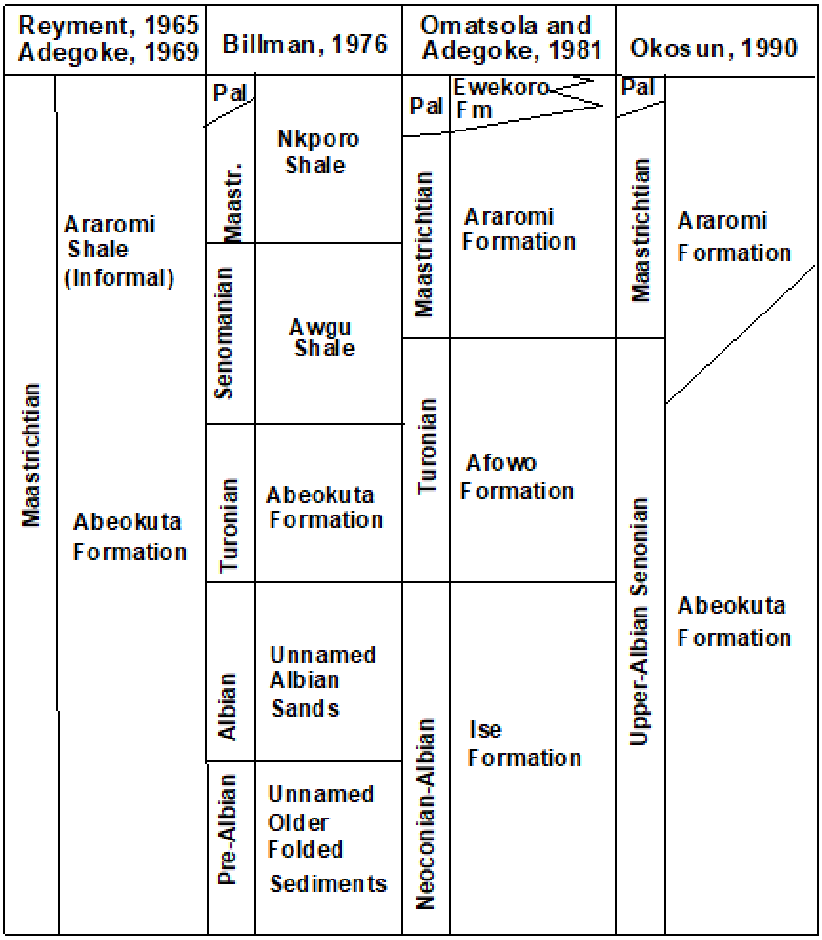

Reyment, 1965 Adegoke, 1969		Billman, 1976		Omatsola and Adegoke, 1981		Okosun, 1990	
Maastrichtian	Araromi Shale (Informal)	Pal	Nkporo Shale	Pal	Ewekoro Fm	Pal	Araromi Formation
		Maastr.		Maastrichtian	Araromi Formation	Maastrichtian	
		Senomanian	Awgu Shale	Turonian	Afowo Formation	Upper-Albian Senonian	Abeokuta Formation
	Abeokuta Formation	Turonian	Abeokuta Formation				
		Albian	Unnamed Albian Sands	Neoconian-Albian	Ise Formation		
		Pre-Albian	Unnamed Older Folded Sediments				

Abigi-Ijebu waterside is situated at the edge of the Dahomey Basin where the basin gradually grades into the Basement Complex rocks of the southwestern Nigeria. Here, basement rocks are exposed in the north with no sediment cover. The central and towards the south of the study area, sediment thickness gradually build up and grades from the very shallow part of the basin into the progressively deeper part of the basin. The thickness of the sedimentary pile as recorded by Adegoke (1969) was put at just few tens of meters to somewhere just above 1000 m.

Materials and Methods

This section briefly describe how the aeromagnetic data of Abigi-Ijebu waterside area of southwestern Nigeria, used for this study, were acquired, as well as presents some of the various processing techniques employed to filter out unwanted signals, transform magnetic anomalies and enhance salient desirable subsurface magnetic attributes that helped to generate geological information used to image and understand the terrain.

Data Acquisition

Airborne magnetic data acquisition was done using a 3 x Scintrex CS3 Cesium Vapour magnetometer having sensitivity of 0.0006 nT √Hz rms, gradient tolerance of 40000 nT/meter and absolute accuracy of less than 2.5 nT throughout the range. The magnetometer which was attached to the tail stinger (behind the empennage of the aircraft) of Cessna Caravan 208B ZS-FSA specialized aircraft uses FASDAS data acquisition system and took magnetic readings at 0.1 seconds recording interval, which is approximately 7 m interval. The aircraft flies at a sensor mean terrain clearance of 80 m, flight line spacing of 500 m, tie line spacing of 5000 m and flight and tie lines trends of 135° and 45° respectively. The flight was flown to run perpendicular to the general geological strike of the field (NGSA 2004; Reeves, 2005).

Data processing involves the transformation of acquired data from the original raw form to a state that bears simple and direct relationship with the terrain/subsurface geology and thus easier to interpret. The processing steps described in this paper exclude the preprocessing operations such as tie-line and micro-leveling, deculturing and others employed to remove residual flight line artifacts and filtering of cultural effects respectively, by the data acquisition company.

The preprocessed/partially processed aeromagnetic data obtained from NGSA were gridded with a cell size of between 1/3 to 1/5 of the flight line spacing, using minimum curvature gridding algorithm (Webring, 1981). The gridded data were thereafter subjected to several filtering operations, example includes Guassian low cut filter to remove the regional trend from the acquired Total Magnetic Intensity (TMI) and thus generate residual magnetic signal while Butterwort, low and high cut as well as band pass filters helped removed noise and noisy data such as cultural and background noise. Data enhancements techniques were applied to improve data quality and amplify specific components of the measured data, especially such components that would ease interpretation. Attribute extraction and derivative determination were performed to further aid interpretation. Horizontal or vertical derivatives, tilt derivatives and total horizontal derivative of the tilt derivative for example are good tools for lineament extraction and thus aid structural interpretation (Verduzco *et al*., 2004). Upward continuation filter was applied to minimize short wavelength signals corresponding to shallow sources and thus enhance deeper source effects. The filter also acts as a cleaning filter because of its ability to remove shallow magnetic signatures that emanate from cultural features and thus enhance relatively deeper anomalies.

Reduction to Pole at Low Latitude (RTPLL)

The shape of magnetic anomaly over a causative body is determined among other factors by shape, size of the causative body, depth of occurrence, magnetic inclination and declination of the inducing field at the survey location (Baranov & Naudy, 1964; Salem *et al*., 2007). The magnetic inclination and declination is dictated by geographical location and thus latitude has effect on the magnetic anomalies. Magnetic anomaly over a body at the poles, north or south, where magnetic inclination is 90^o ($I = 90^o$) or 0^o at the equator ($I = 0^o$) is believed to be simple to interpret and most importantly the anomaly peak is located directly over the causative body (Silva, 1986; Arkani-Hamed, 1988; Lu *et al*., 2003). At the mid north and mid south latitudes however, the anomaly becomes complex with the anomaly peak not lying directly over the corresponding source. Therefore to simplify anomalies and ensure that anomalies lie directly above the causative body, reduction to pole correction is usually applied.

Ijebu waterside in southwest Nigeria is located at mid north, slightly above the equator. It is also located at low latitude (around latitude 7^0), therefore anomalies in this study area are presented in complex form. Also the peaks of the anomalies may not be properly placed on top of the causative sources. This therefore demands the need to carry out reduction to pole correction to simplify the anomaly and for correct focusing of anomaly peak over the causative source. Reduction to the pole for data acquired at low magnetic latitudes (equatorial latitudes) is known to blow-up anomalies originating from north-south lying geological features (Li, 2008). The blow-up is associated with strong amplitude correction that is applied when the declination and wavenumber direction is ð/2 (That is, a magnetic East-West wavenumber) (MacLeod *et al*., 1993; Li, 2008). Thus a specialized correction known as reduction to pole at low latitude was usually applied. Reduction to the Equator (RTE) could also be applied, but this will invert the magnetic data making the anomalies appear negatively symmetrical over corresponding geologic sources. Reduction to the pole at low latitude (RTPLL) incorporates a separate amplitude correction which prevents signals from north-south geological features from becoming over blown and thus dominating the results (Keating & Zerbo, 1996). The specialized correction will simplify anomalies and focus the anomalies peak over the corresponding causative bodies which are easier to interpret without losing any geological/geophysical relevance.

Derivative and Tilt Angle Derivative filters

Derivative-based filters were used to sharpen the edges of magnetic anomalies and to determine their locations (Mushayandebvu *et al*., 2001). They were also used to enhance or suppress features in a given direction, such as x-, y-, and z- directions (Cooper & Cowan, 2008). The horizontal derivatives, along the x- and y-directions were calculated in order to estimate the magnetic variation along the horizontal. The vertical derivative along the z-direction on the other hand estimates vertical variation in magnetic properties of the rocks (Ekinci *et al*., 2013). Tilt derivative filter and the horizontal derivative of the tilt derivative grids were also generated to further enhance structural signatures of the magnetic data across study area. The tilt derivative filter, an analytic signal amplitude normalized ratio of vertical derivative to a value of total horizontal derivative (equations 1 & 2) is apt at enhancing the edges of features and other directional information inherent in potential data which oftentimes are of great structural significance (Miller & Singh, 1994; Verduzco *et al*., 2004; Ferreira *et al*., 2011).

$$TLT = \tan^{-1} \frac{\frac{dM}{dz}}{\left(ThD\right)} \qquad (1)$$

$$ThD = \sqrt{\frac{dM}{dx}^{2} + \frac{dM}{dy}^{2}} \qquad (2)$$

TLT is the Tilt derivative filter, $\frac{dM}{dz}$, $\frac{dM}{dx}$ & $\frac{dM}{dy}$ are the vertical and the two horizontal derivatives of the magnetic field respectively while ThD is Total Horizontal Derivative of Magnetic field.

Euler Deconvolution

The 3D Euler deconvolution is a depth estimating technique and it is used to determine depth and location of geologic unit or structure that produces magnetic anomaly. It uses the x-, y-, z- derivatives to determine location and depth for various idealized targets such as contact, dyke/sill, cylinder and sphere (Reid & Thurston, 2014). Each of the idealized targets is characterized by a specific Structural Index (SI), which measures the fall-off rate of the field with distance from the source. There are two methods; the 'Standard Euler method' and the 'Located Euler method'. The Standard Euler method is based on Euler's homogeneity equation (equation 3), which relates the magnetic potential field and its gradient components to the location of the sources, by the degree of homogeneity N (Thompson, 1982).

$$\left(x - x_0\right)\frac{\partial T}{\partial x} + \left(y - y_0\right)\frac{\partial T}{\partial y} + \left(z - z_0\right)\frac{\partial T}{\partial z} = N(B - T) \qquad (3)$$

Where: x_0, y_0, & z_0 define the position of a source whose total field T is detected at any point (x, y, z), B is the background value of the total field, and N is the Structural Index (SI) which is the degree of homogeneity of the source body, interpreted physically as the attenuation rate with distance (Whitehead & Musselman, 2008).

In this study, the Standard Euler deconvolution was applied to estimate depth to magnetic sources. The 3D Euler deconvolution process was applied at each solution point by setting an appropriate SI value and using least-squares inversion to solve the equation for an optimum values for x_0, y_0, z_0 and B over a square window of 400 by 400 m which consists of the number of cells in the gridded dataset. The individual grid cell size is equivalent to a quarter of the square root of the grid area divided by the number of data point. All points in the window were used to solve the Euler's equations for solution depth, inversely weighted by distance from the centre of the window.

Finally, radial power spectrum analysis which is also useful for determining depth to volcanic intrusion or magnetic basement, based on the spectral analysis of magnetic data using Fourier transform (Garcia & Ness, 1994) was carried out to confirm the result obtained from the 3D Euler deconvolution results.

Results and Interpretation

The results and geological interpretations of the processed aeromagnetic data of Ijebu waterside (study area) are presented in this section. The processed and gridded aeromagnetic data of Ijebu-waterside and environs is presented as the Residual Magnetic Intensity (RMI) map in figure 2. The map indicates short and relatively long wavelength anomalies, some of which are positive while others are negative. The positive magnetic intensities are regions of the study area having relatively high magnetic relief which correspond to regions with relatively high magnetic susceptibilities. The negative magnetic intensity areas on the other hand are areas of low magnetic relief corresponding to regions of relatively low magnetic susceptibility. Residual magnetic intensity distribution across the study area ranges from - 40 nT to 138.5 nT (Figure 2). The northern and considerable part of the central portion of the study area is dominated by high positive anomaly while the southern end displayed low negative magnetic intensity. This defines the area with high and low magnetic reliefs, respectively.

The extracted horizontal and vertical derivatives which were generated in order to

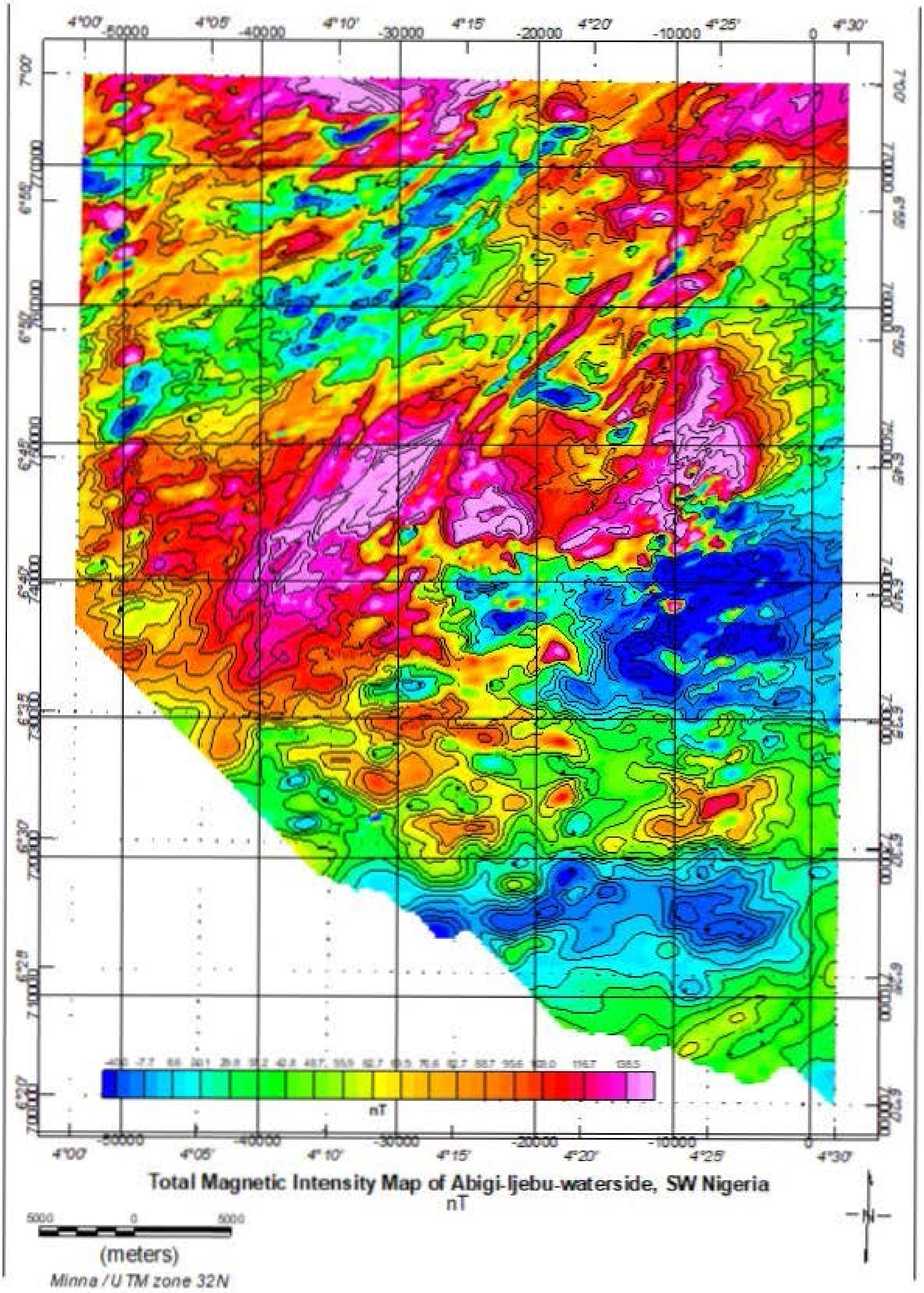

Figure 2. Residual Magnetic Intensity (RMI) map of Ijebu – waterside and environs.

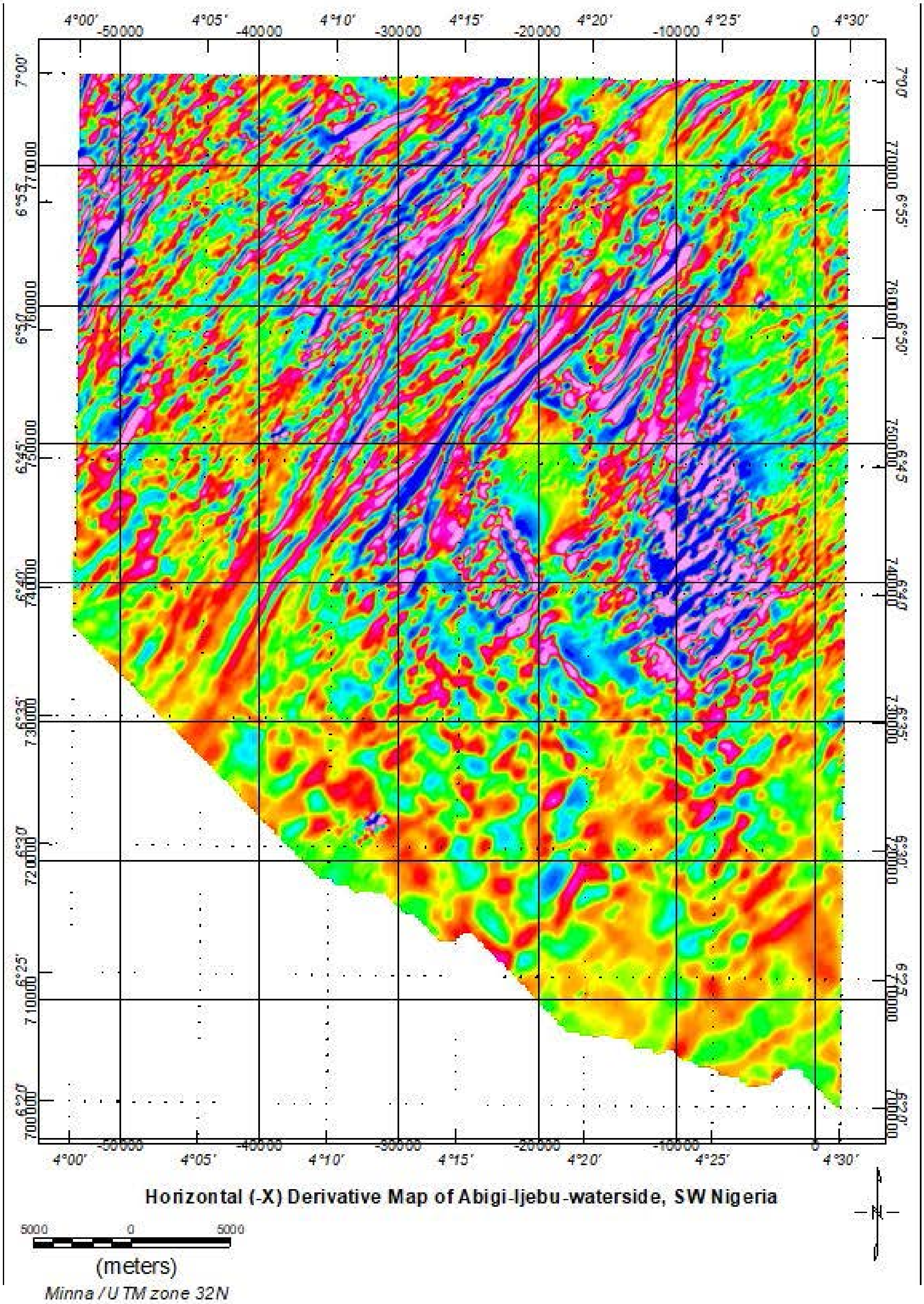

Figure 3. Horizontal Derivative (in x- direction) Map of Abigi, Ijebu-waterside.

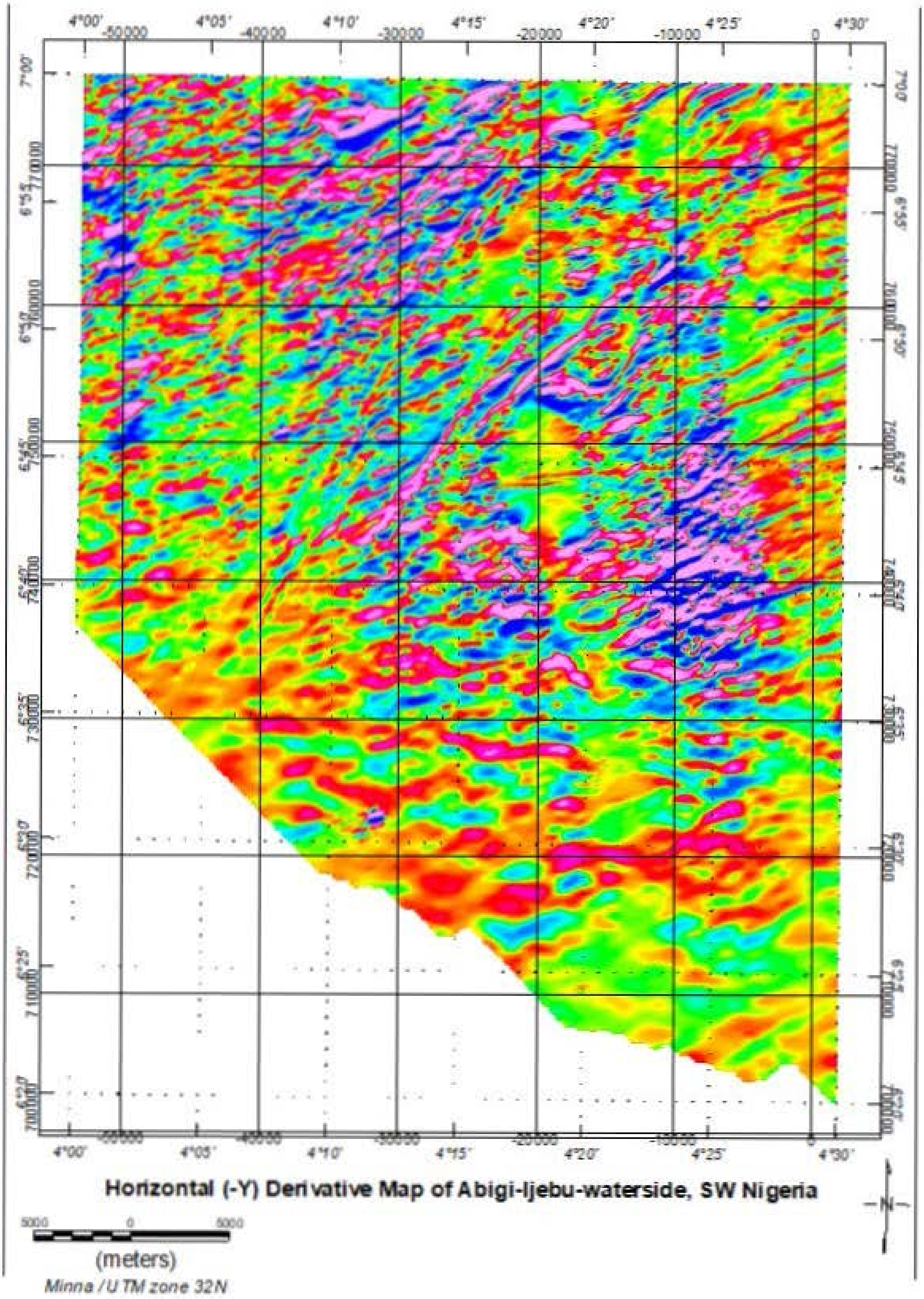

Figure 4. Horizontal Derivative (in y- direction) Map of Abigi, Ijebu-waterside.

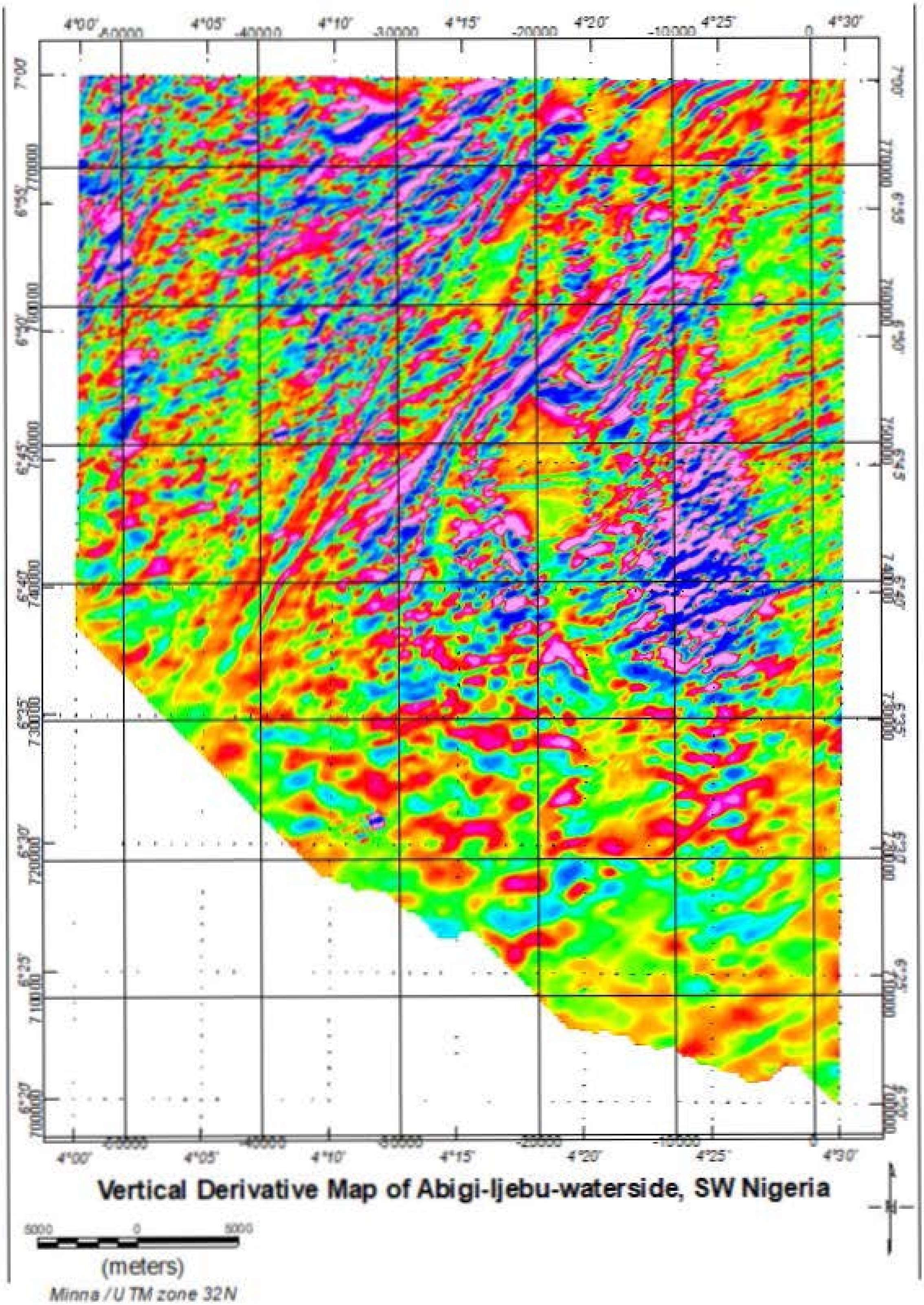

Figure 5. Vertical Derivative (in z- direction) Map of Abigi - Ijebu-waterside.

enhance linear features such as fractures, faults and sheared zones are presented in figures 3, 4 and 6, respectively. The results indicate series of linear magnetic features, many of which are aligned along NE - SW directions. Some of preferentially aligned magnetic features as observed on the derivative maps correspond to linear geological features that generate the preferentially oriented magnetic anomalies.

The tilt derivative and the total horizontal derivative of the tilt derivative grids are presented in figures 6 and 7 respectively. The figures present enhanced edges of linear features which may have originated from deep and shallow sources (Miller & Singh, 1994). The gridded maps of both tilt angle derivatives and total horizontal derivative of the tilt angle derivative like the horizontal and vertical derivative maps also indicate a number of linear features which show predominant alignment of regional and extensive linear structures along NE - SW direction. The tilt derivative grids present better resolved linear structures around Abigi - Ijebu waterside with many visible and better enhanced preferentially aligned patterns in the central part of the grid unlike those observed in the vertical and horizontal derivative grids. The summary of the structural analyses which consist of results obtained from derivative grids as well as tilt angle derivative and the horizontal derivative of tilt angle derivative grid is presented in figure 8 as the lineament map of the study area. The lineament map presents only linear features that appear to originate from deeper sources and also show regional trend, being up to 5 km in length. The trend and orientation of the extracted linear features from structural analysis of aeromagnetic data of Abigi – Ijebu waterside (Figure 8) correlates positively with the established NE - SW structural trend of southwestern part of Nigeria (Burke *et al*., 1976; Rahaman, 1976) as well as lineament map of southwestern Nigeria compiled from field observations during structural and geological mapping of the region.

Euler Deconvolution / Depth Estimation Results

Euler deconvolution depth weighting technique employed to determine depths to magnetic sources in the study area using different structural indexes (0.0 – 3.0), presented geologically reasonable solutions with structural index of 1, which represents contact and faults model (Reid & Thurston, 2014). The Euler solution proportional depth plots indicate shallow depth solutions (above the reference datum) to the magnetic source in the north while deep solutions characterize the south (Figure 9a). The Euler depth solution distribution across the study area (Figure 9b) indicates that the basement crustal rocks generally occur at about 100 m above the Minna reference datum in the northern part of the study area. The basement rocks gradually dips southwards as the crustal rocks get more depressed and deeper to create more accommodation for clastic sedimentary rocks at the edge of the Dahomey Basin. The basement configuration, allows the southern part of the study area, especially with continuous increase in depth to basement rocks southward, toward the Atlantic Ocean, to be overlain by relatively thick sedimentary rock units (in excess of 2 km). This implies that if the rate of basement depression presented by the Euler depth weighting of the onshore part of the Abigi-Ijebu waterside is maintained, projecting southward (offshore) beyond the area covered in this study, sedimentary thickness will exceed 3 km, few kilometers seaward into the Atlantic Ocean. The result of spectral analysis carried out on the aeromagnetic data of Abigi-Ijebu waterside as presented by the averagely power spectrum plot and the corresponding depth estimate (Figure 10) indicate shallow and relatively deep depth estimate results. The shallow depth results range from just above the reference datum to less than 500 m below the datum, while the relatively deeper depth result is more than 2000 m below the Minna datum. The shallow results represent the spectral analysis of magnetic data of regions where magnetic source (basement rocks) exit at the surface or very close to the ground surface which according to Euler deconvolution result coincide with the northern and part of the central portion of the study area. The relatively deeper depth as shown by the Euler solution is restricted to the southern end of the study area.

Discussion of Results

The various analyses carried out on the aeromagnetic data of Abigi – Ijebu waterside, as shown by the structural as well as the depth to basement mapping results indicate that the study area has undergone active tectonic activities in the past. This is evident by the numerous regional tending structural features, some of which are more than 15 km in length, in addition to the down warping basement geometry as shown from the spectral analysis and Euler deconvolution results. This unique basement characteristic is associated with sedimentary basin edge where the depression of the basement rocks (slab) began. This region is usually associated with numerous

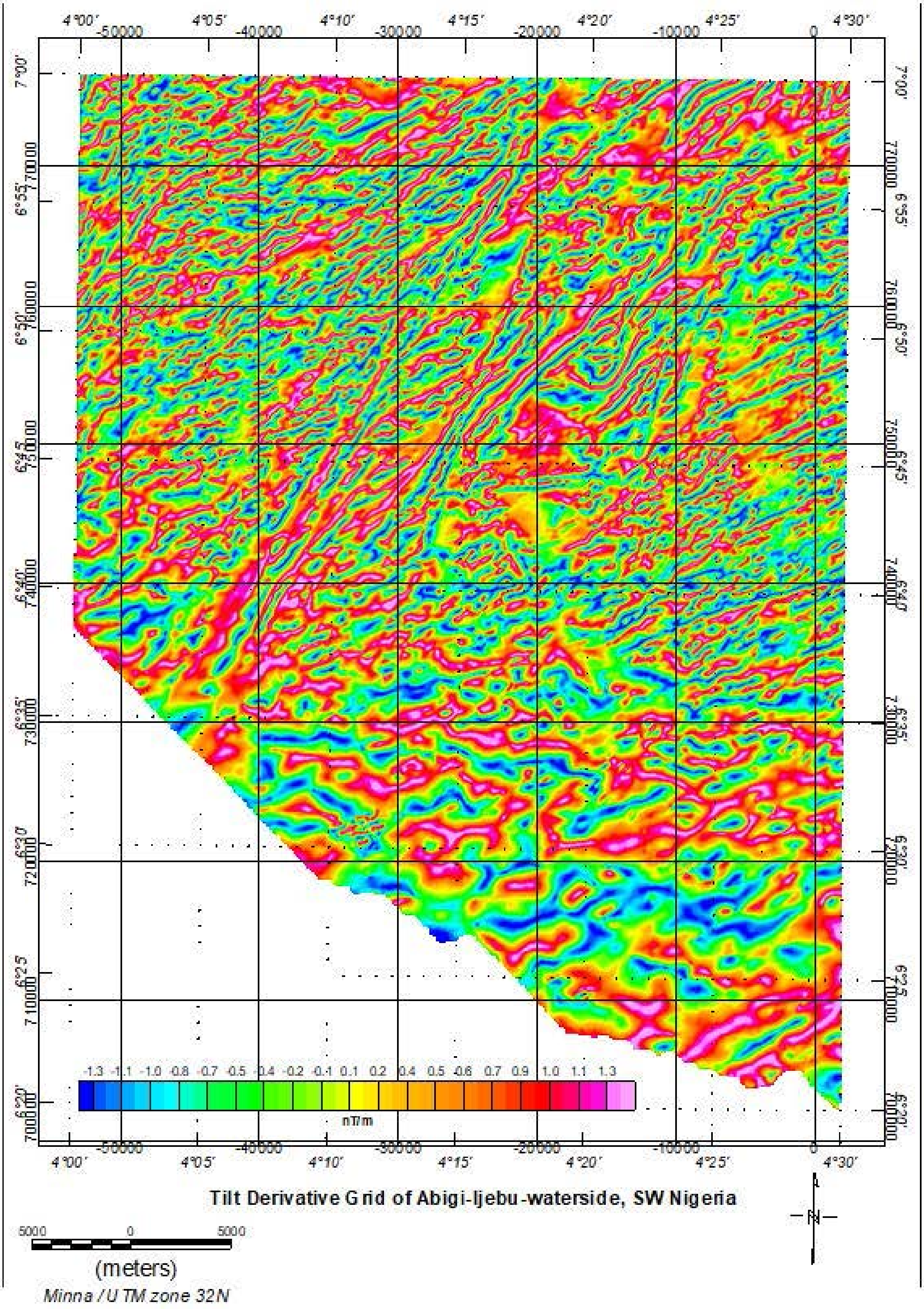

Figure 6. Tilt Angle Derivative Map of Abigi, Ijebu-waterside.

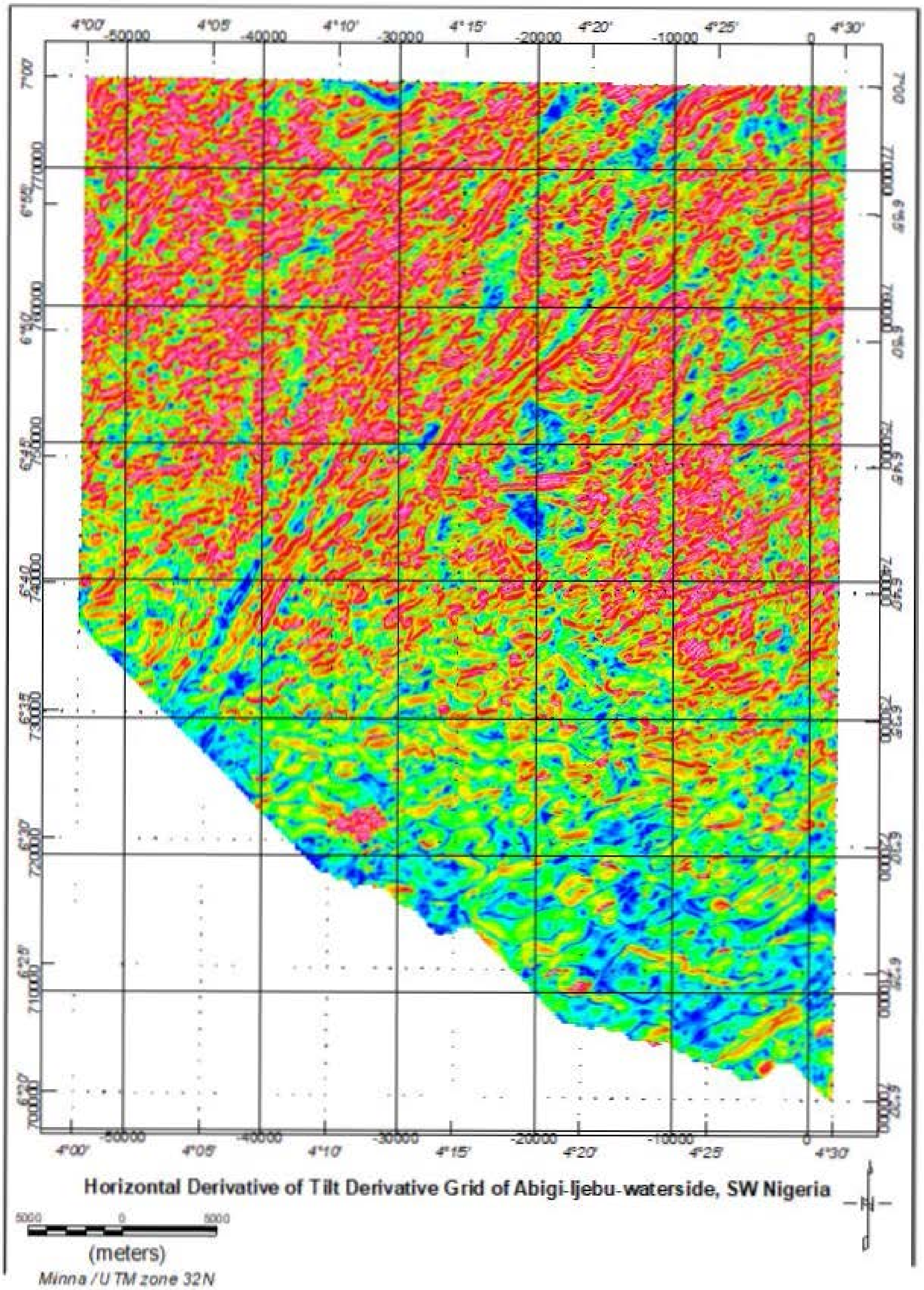

Figure 7. Total Horizontal Derivative of Tilt Derivative grid of Abigi, Ijebu-waterside.

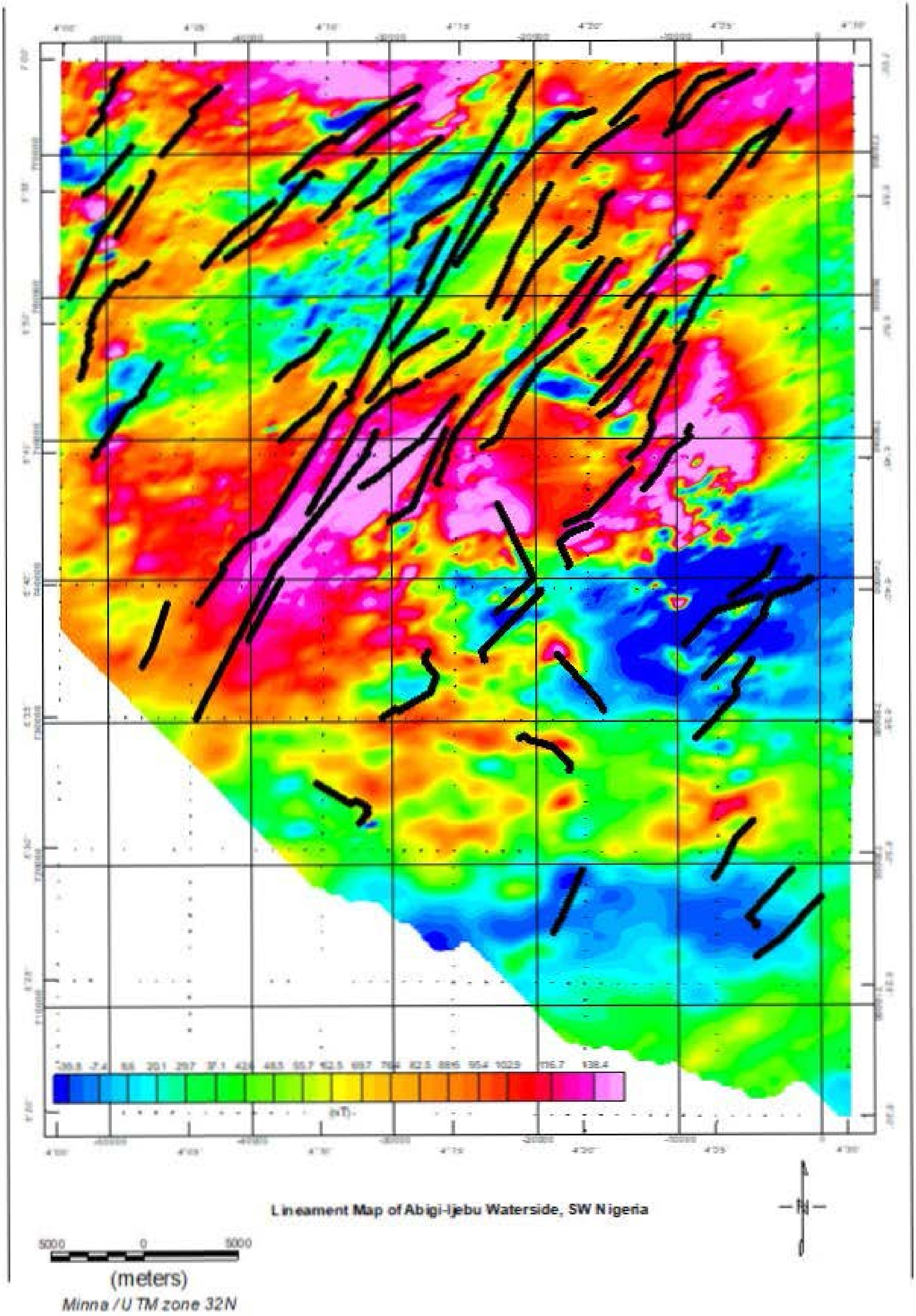

Figure 8. Lineament Map of Abigi-Ijebu-waterside, SW, Nigeria.

faults many of which could take the form of step faults or horst and graben in response to brittle deformation at the basin edge. Here the effect of associated flow/ductile deformation influenced by the magmatic activity that initiated the formation of the basin may be minimal.

Previous authors based on interpretation of some few wells and outcrop studies have described the basement topography of the eastern Dahomey Basin, which Abigi – Ijebu waterside belongs, as composed of a series of horst and graben structures (Omatsola & Adegoke, 1981; Olabode & Adekoya, 2007). The study area is a small section of the Dahomey Basin which was described to span 440 km in length (Francheteau & Le Pichon, 1972) and therefore represents a part in terms of structure and basement geometry. The results obtained through the analyses of magnetic data of the study area confirmed the occurrence of regional structures whose trend agrees with previous works. However the depth

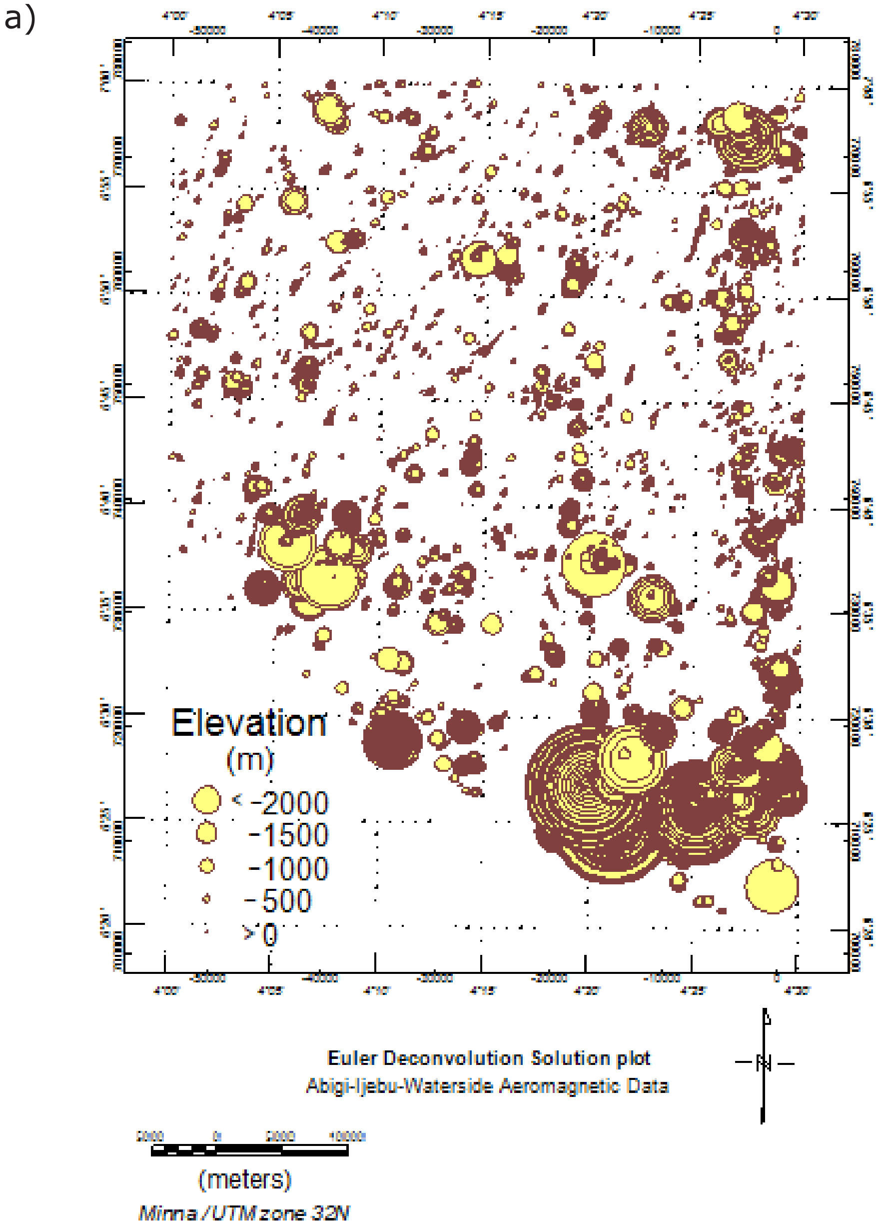

Figures 9. (a) Euler Solutions Depth proportional plots.

b)

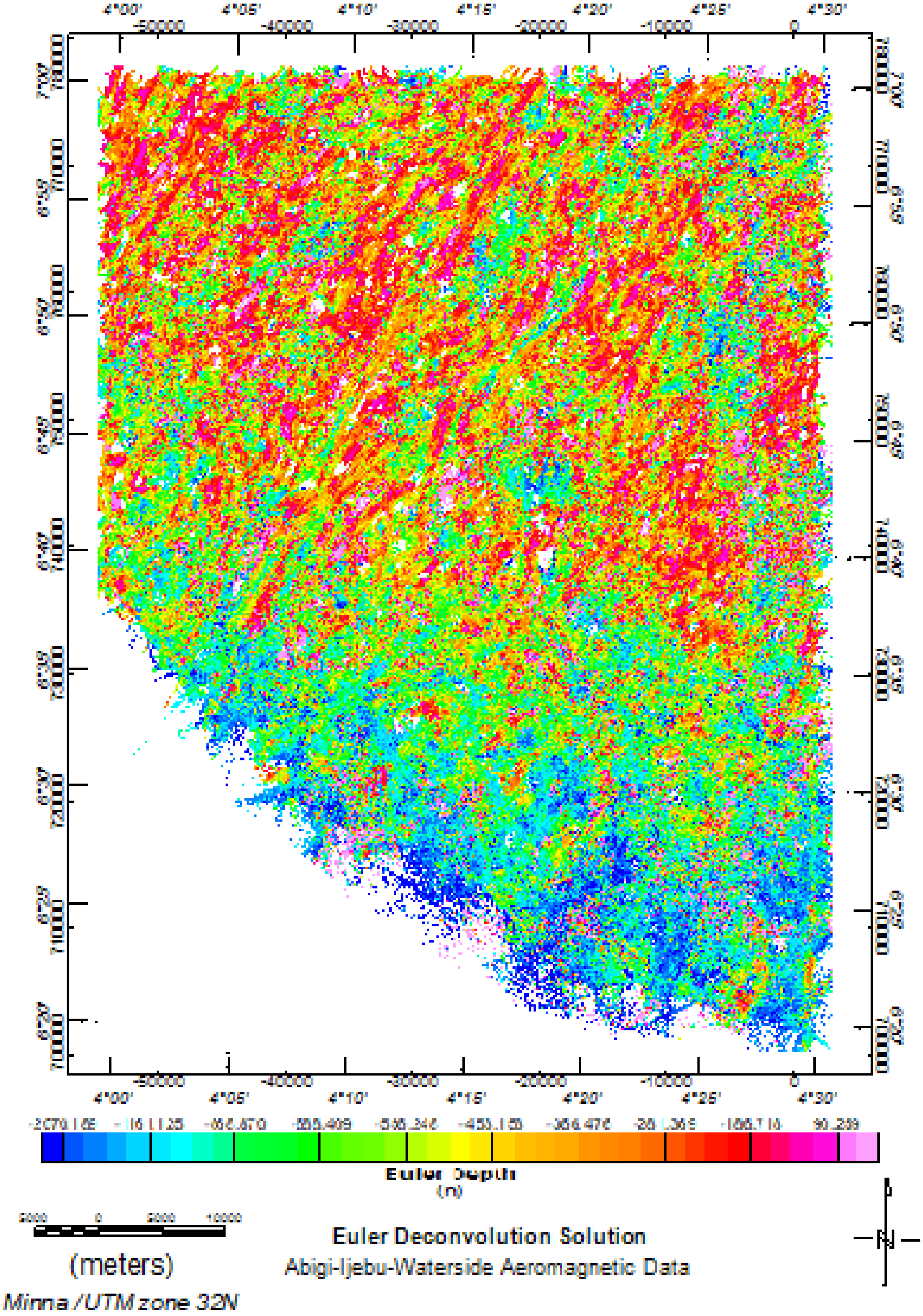

Figure 9. (b) Euler Depth distribution across the study area (Structural Index (N) 0.1).

weighting results did not indicate sharp drop in depth characteristic of rifting which could support the horst and graben model around the study area, rather a gentle increase in depth from about 100 m above the reference datum in the north to around 2000 m in the south. The distribution of the Euler solutions points as well as the narrow range of data suggest a rather gentle step increment in depth to basement rocks that could be attributed to step faulting.

The integration of the obtained results from this study and previous studies such as the works of Francheteau & Le Pichon, (1972), Burke *et al* (1976), Omatsola & Adegoke, (1981), Olabode and Adekoya (2007) among others suggest that the study area may be part of the regional horst and graben structure but exhibit step faulting around the study area which causes the thickness of clastic sediment overlying the basement rocks to progressively thickens southward as the basement rocks dip southwards and the crustal slab get more and more depressed towards the sea.

This probably explains the reason for the occurrence of tar sands instead of oil and gas pools in the area. This is because oil and gas generation, accumulation and preservation require considerable depth, usually in excess 3 km, to guarantee the appropriate temperature and pressure conditions required for generation of hydrocarbon from organic matter as well as maintenance of the cap rock integrity for the preservation of the generated hydrocarbon. Where the thickness of the sedimentary unit is less than this minimum average, poorly matured organic matter as well as poorly preserved generated hydrocarbon will result which upon further exposure to the surface conditions such as biodegradation will generate bitumen, bituminous or and tar sands.

The discovery of commercial accumulations of hydrocarbon in the eastern and western offshore of the Nigerian sector of the Dahomey Basin, such as. Aje and Ogo oil and gas fields suggests the basement topography further south support the accumulation of up to 3 km of clastic sediment which is one of the most important petroleum accumulation and preservation requirements. This therefore points to south of the study area (into the deep offshore) as prospective area for petroleum prospect evaluation and development.

Conclusions

The analysis and interpretation of various enhanced, derivative and attribute maps generated from the high resolution aeromagnetic data of Abigi-Ijebu waterside in southwestern Nigeria revealed the distribution of crystalline basement rocks at considerable

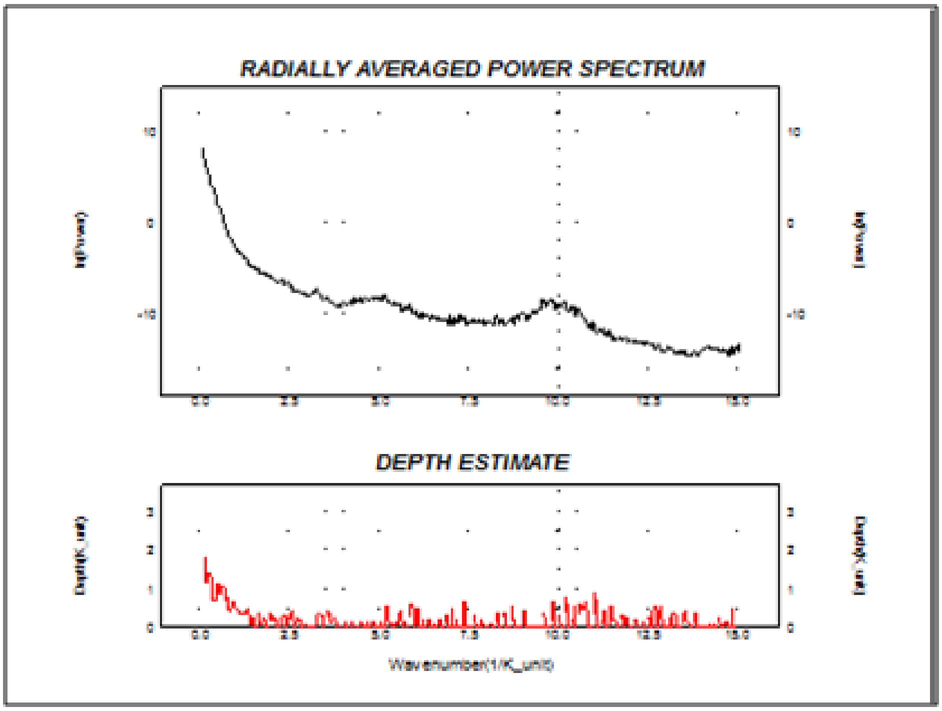

Figure 10. Radially Average Power Spectrum Analysis of Magnetic data of Abigi – Ijebu waterside, SW Nigeria.

depth, identified structural framework as well as the basement topography which determines the thickness of sedimentary units overlying the Ijebu waterside region of the Nigerian sector of the Dahomey Basin. The structural framework as defined by the enhanced linear structures derived from the application of derivative filters indicate occurrence of regional linear structures, some of which are more than 15 km in length and generally trend NE - SW. The gradual increase in depth to magnetic source from about 100 m to over 2.0 km southward as obtained from spectral analysis and Euler deconvolution solutions indicate a gentle increase in thickness of the overlying sedimentary unit towards the south as the crustal rocks get depressed through the aid of regional faults which gradually step down the basement rocks southward toward the ocean. The basement geometry and structural framework point south of the study area, toward the offshore of the Dahomey Basin as the appropriate direction to focus hydrocarbon exploration energy since further basement depression and corresponding thickness of sedimentary rocks could support hydrocarbon generation and preservation.

References

Adegoke, O. S., 1969, Eocene Stratigraphy of Southern Nigeria. Bureau de Recherches Geologiques et Minières Memoir, 69, 23-48.

Ako, B. D., Adegoke, O. S., & Petters, S. W., 1980, Stratigraphy of the Oshosun Formation in South-Western Nigeria. Jour. Min. Geol., 17, 97-106.

Arkani-Hamed, J., 1988, Differential reduction to the pole of regional magnetic anomalies. Geophysics, 53 (12), 1592-1600.

Burke, K. C., Freeth, S. J. & Grant, N. K. 1976. The structure and sequence of geological events in the Basement Complex of Ibadan area, Western Nigeria, Prec. Res. Vol. 3 No. 6.

Baranov, V. & Naudy, H., 1964, Numerical calculation of the formula of reduction to the magnetic pole. Geophysics, 29, 67–79.

Billman, H. G., 1976, Offshore stratigraphy and paleaontology of the Dahomey basin, West Africa. Nigerian Association of Petroleum Explorationist Bulletin, 7, 121-139.

Brownfield, M. E. & Charpentier, R. R., 2006, Geology and Total Petroleum Systems of the Gulf of Guinea Province of West Africa U.S. Geological Survey Bulletin 2207- C.

Burke, K. C, Freeth, S. J. & Grant, N. K., 1976, The structure and sequence of geological events in the Basement Complex of Ibadan area Western Nigeria Precamb. Res. 3:537-545.

Cooper, G.R.J. & Cowan, D. R., 2008, Edge enhancement of potential-field data using normalized statistics. *Geophysics,* 73 (3), H1–H4.

Ekinci Y. L., Ertekin C. & Yiğitbaş E., 2013, On the effectiveness of directional derivative based filters on gravity anomalies for source edge approximation: synthetic simulations and a case study from the Aegean graben system (western Anatolia, Turkey) J. Geophys Eng. Vol. 10 (3) :035005. doi:10.1088/1742-2132/10/3/035005.

Francheteau, J. & Le Pichon, X., 1972, Marginal fracture zones as structural framework of continental margins in South Atlantic ocean. *The American Asscoiation of Petroleum Geologists Bulletin, 56*(6), 991-1007.

Ferreira, F. J. F., de Castro, L. G., Bongiolo, A. B. S., de Souza, J. & Romeiro, M. A. T., 2011, Enhancement of the total horizontal gradient of magnetic anomalies using tilt derivatives: Part II—Application to real data: 81st Annual International Meeting, SEG, Expanded Abstracts, 887–891.

Garcia. J. G., & Ness, G. E., 1994, Inversion of the power spectrum from magnetic anomalies. Geophysics, vol. 59, 3, pp. 391-401.

Grant, N. K. 1971. South Atlantic, Benue trough and Gulf of Guinea Cretaceous triple junction. *Bull. geol. Soc. Am.* 82,2295-2298.

Idowu J. O. & Ekweozor C. M., 1993, Petroleum potential of cretaceous shales in the Upper Benue trough, Nigeria. J. Petrol. Geol., 21, 105-118.

Jones, H. A. & Hockey, R. D., 1964. The Geology of part of southwestern Nigeria; *Geological Survey of Nig. Bull*, 31: 101-104.

Keating P. & Zerbo L., 1996, An improved technique for reduction to the pole at low latitudes. Geophysics, 61(1), 131-137.

Kogbe, C. A., 1974, Paleo-ecologic significance of vertebrate fossil in the Dukamaje and Dange Formations (Maastrichtian and Paleocene) of northwestern Nigeria. Jour. Min. Geol.(Nigeria). 8, 49-55.

Li, X., 2008, Magnetic reduction-to-the-pole at low latitudes: observations and considerations. *Lead Edge*, 27, 990–1002.

Lu, R.S., Mariano, J & Willen, D. E., 2003, Differential reduction of magnetic anomalies to the pole on a massively parallel computer. Geophysics, 68 (6), 1945-1951.

Macleod, I. N., Jones, K. & Dai, T. F., 1993, 3-D analytic signal in the interpretation of total magnetic field data at low magnetic latitudes. *Explor. Geophys.,* 24, 679–688.

Miller, H. G. & Singh,V., 1994, Potential field tilt - a new concept for location of potential field sources. *Journal of Applied Geophysics*, 32, 213–217.

Mushayandebvu, M. F., Van Driel, P., Reid, A. B. & Fairhead, J. D. 2001, Magnetic source parameters of two-dimensional structures using extended Euler deconvolution. *Geophysics*, 66, pp814-823.

Nabighian, M. N. & Hansen, R. O. 2005, Unification of Euler and Werner deconvolution in three dimensions via the generalized Hilbert transform, Geophysics, 66.

Nigeria Geological Survey Agency (NGSA), 2004, Airborne Geophysical Digital data Dissemination Guideline.

Nigeria Geological Survey Agency (NGSA), 2009, Geological map of Southwestern Nigeria.

Obaje, N. G., 2009, Geology and Mineral Resources of Nigeria. Lecture note in Earth Sciences, Heidelberg. 219pp.

Ogbe, F. A. G., 1970, Stratigraphy of strata exposed in the Ewekoro Quarry Western Nigeria. In: (Dessauvagie, T. F. J. and Whiteman, A. J. (eds). African Geology University of Ibadan Press, Nigeria, 305-324.

Okosun, E. A., 1990, A review of the Cretaceous stratigraphy of the Dahomey Embayment, West Africa. – Cretaceous Research, 11, 17-27.

Olabode, S. O. & Adekoya, J. A., 2007, Seismic stratigraphy and development of Avon canyon in Benin (Dahomey) basin, southwestern Nigeria. *Jour. of African Earth Sciences* 50, 286-304.

Omatsola, M. E. & Adegoke, O. S., 1981, Tectonic evolution and Cretaceous Stratigraphy of the Dahomey Basin. *Jour. of Mining Geology*, 8, 130-137.

Paterson, N. R. & Reeves, C.V., 1985, Applications of gravity and magnetic surveys : the state-of-the-art in 1985. Geophysics, 50, 2558-2594.

Rahaman, M. A., 1976, Review of the Basement Geology of Southwestern Nigeria. In: Geology of Nigeria, edited by C.A. Kogbe, Elizabethan Publ. Co., Lagos. pp. 41-58.

Reeves C. V., 2005, Aeromagnetic surveys: Principles, practice and Interpretation. 155pp.

Reid A. B., Allsop I. M., Grsner H, Millet A. J. & Somerton I. W., 1990, "Magnetic interpretation in three dimensions using Euler deconvolution", Geophysics, 55, 80 – 91

Reid, A. B. & Thurston, J. B., 2014, The structural index in gravity and magnetic interpretation: Errors, uses, and abuses, Geophysics, 79 (4), J61–J66.

Salem, A., Williams, S., Fairhead, J. D., Ravat, D. & Smith, R., 2007, Tilt depth method: A simple depth estimation method using first-order magnetic derivatives: The Leading Edge, 26, 1502–1505, doi: 10.1190/1.2821934.

Silva, J. C. B., 1986, Reduction to the pole as an inverse problem and its application to low latitude anomalies. Geophysics, 51 (2), 369-382.

Thompson, D. T., 1982, EULDPH. A New technique for making computer assisted depth estimates from magnetic data. Geophysics, 47, 31-37.

Verduzco, B., Fairhead, J. D. & Green, C. M., 2004, New insights into magnetic derivatives for structural mapping. *The Leading Edge*, 23 (2), 116–119.

Webring, M., 1981, MINC, a gridding program based on minimum curvature: U.S. Geological Survey Open-File Report 81-1224, 43 p.

Whitehead, N., & Musselman, C., 2008, Montaj Grav/Mag Interpretation: Processing, Analysis and Visualization System for 3D Inversion of Potential Field Data for Oasis montaj 63 pp.

Geofísica Internacional (2019) 58-4: 279-293

Original paper

Electrical Resistivity Tomography for the detection of subsurface cavities and related hazards caused by underground coal mining in Coahuila

José A. Batista Rodríguez*, Marco A. Pérez Flores, Yuri Almaguer Carmenates and Maximiliano Bautista Hernández

Received: September 05, 2018; accepted: September 27, 2019; published on line: October 01, 2019

Resumen

En este estudio se utilizó Tomografía de Resistividad Eléctrica para identificar cavidades en el subsuelo de la región carbonífera del Estado de Coahuila, originadas por la minería del carbón, y con ello se valora el riesgo geológico inducido. Las mediciones se tomaron a lo largo de perfiles ubicados en las proximidades de carreteras y puentes, dentro de sectores de actividad minera. Estos perfiles se ubican evitando las propiedades privadas y abarcando algunas zonas de hundimientos de las carreteras. Se considera que la subsidencia es antropogénica y está relacionada con la actividad minera somera y relativamente profunda. En las secciones transversales de resistividad eléctrica obtenidas del proceso de inversión se identifican varias cavidades con diferentes formas desde los 7 m de profundidad. La mayoría de estas estructuras causan deformaciones en la superficie, generando hundimientos y fracturas en las carreteras. De forma general, las cavidades identificadas en dos de los sectores analizados se encuentran rellena de agua o sedimentos. En un tercer sector todas las cavidades están vacías o parcialmente rellenas con material colapsado de sus paredes y techos. Las secciones eléctricas revelan otras características del ambiente geológico, tales como zonas de disminución de los niveles acuíferos, inclinación de estratos (que indican paleo-subsidencia del terreno), fallas y fracturas que afectan la secuencia estratigráfica. La disminución de los niveles de los acuíferos indica cambios en el régimen hidrodinámico de las aguas subterráneas que han sido ocasionados por los espacios vacíos generados por la minería. Estos cambios provocan que el subsuelo se hunda debido a la presión litostática y el peso de los vehículos que pasan por encima de las carreteras. Como resultado final, se ubican en los tres sectores analizados, las áreas con mayor riesgo potencial de peligros relacionados con el hundimiento del subsuelo.

Palabras clave: minería subterránea del carbón, cavidades, subsidencia, Tomografía de Resistividad Eléctrica, región carbonífera de Coahuila.

J. A. Batista Rodríguez*
Y. Almaguer Carmenates
M. Bautista Hernández
Escuela Superior de Ingeniería
Universidad Autónoma de Coahuila
Nueva Rosita, 26830, México
**Corresponding author: josebatista@uadec.edu.mx*

M. A. Pérez Flores
División de Ciencias de la Tierra, CICESE
Baja California, 22860, México

Abstract

This study used Electrical Resistivity Tomography (ERT) to identify the subsurface cavities in the carboniferous region on the State of Coahuila caused by underground coal mining and the hazards they induce. Measurements were taken next to roads and bridges support in three sectors with mining activity. Authors used roads to run the ERT profiles in order to avoid private properties, with some of these profiles including areas with subsidence. It is considered that subsidence is an anthropogenic related to both shallow and relatively deep underground mining activity. The electrical resistivity cross-sections obtained from the geophysical inversion process identified several cavities with a variety of dimensions ranging upwards from a depth of 7 m. Most of these structures cause deformations on surface in the form of subsidence or fractures. In general, the cavities identified in two of the sectors analyzed are filled with water or sediments. In a third sector analyzed in this study, all cavities were either empty or partially filled with collapsed material from their walls and ceiling. Geo-electrical sections reveal other characteristics of the geological environment, such as zones in which aquifer levels decrease, strata dipping (indicating prior subsidence), and faults and fractures that affect the stratigraphic sequence. The decrease in aquifer levels indicates changes in the hydrodynamic groundwater regime that have been caused by the voids generated by mining. These changes cause the ground to sink due to lithostatic pressure and the weight of the vehicles passing above. As a final result, the areas at the greatest potential risk of hazards related to ground subsidence are located within the three analyzed sectors.

Key words: underground coal mining, cavities, subsidence, Electrical Resistivity Tomography, the carboniferous region of Coahuila.

Introduction

The mining industry has been well known for the potential of risk it generates, mainly underground mining operations. These operations can generate geotechnical accident, such as, roof collapse, subsidence, landslides, rock burst, etc., which negatively affects economic profitability. Underground mining operations generating damage on the surface of the ground in urbanized and populated zones. The most important and most frequent problems related to mining operation include mine subsidence and risk to buildings, for example, in the Upper Silesia Coal Basin (Strozik *et al.*, 2016) and in some coal mining of China (Chugh, 2018).

The Sabinas basin, located in Northeastern Mexico, contains significant coal deposits (Figure 1) distributed across eight sub-basins (Rivera-Martínez and Alcocer-Valdés, 2003). The exploitation of this mineral resource through open pit and underground mining (mainly longwall mining method) has caused major modifications to the environment, including the generation of underground galleries and low relief areas. When caused by rudimentary mining, these galleries can be very shallow and small, whereas those caused by deep mining (conducted at approximately 350 m) may be much larger (SE, 2017). These galleries can often collapse, causing deformations to the geological environment such as fractures, faults, and terrain collapse (Bruhn *et al*., 1978). In areas with shallower galleries, there is a greater hazard of subsidence (Bruhn *et al*., 1978; Peng, 2008), a process which has been identified in some sectors of the Sabinas basin (Serrano-González, 2014) and which affects socio-economic infrastructure such as roads, buildings, and bridges supports. The locations of these sectors suggest that this process could be related to collapsing of underground galleries, namely subsurface cavities generated by underground coal mining.

Cavities generated by underground coal mining can be partially or completely air-filled, water-filled or sediment-filled (Van Schoor, 2002; Zhou *et al*., 2002). In all cases, the cavities can be identified by the contrast between their physical properties and the surrounding geological environment. Electrical resistivity is one of the main physical properties that enable the characterization of these structures (Militzer *et al*., 1979; Putiska *et al*., 2012).

In the study region, coal is located in a sedimentary sequence formed by sandstones and shales overlapped by conglomerates or sediments such as alluviums, sands and clays (SGM, 2003; Corona-Esquivel *et al*., 2006; González-Sánchez *et al*., 2007).

In this research, the ERT was used in three sectors of the Sabinas coal basin to locate and characterize subsurface cavities related to underground coal mining and identify the anthropogenic hazard they induce. The three sectors selected are located in areas in which mining activity is undertaken next to roads, bridges and buildings. Two sectors with subsidence and one without visible subsidence were selected. The subsidence in one of the sectors was related to shallow mining while it was related to relatively deep mining in the other.

Geological setting

The Sabinas Basin initially developed on the margin of the North American Craton during the opening of the Gulf of Mexico in the early Mesozoic. This basin is a depression formed by a series of subsided blocks. The Sabinas Basin is separated from the Chihuahua Basin by blocks elevated to the Northwest (Eguiluz de Antuñano, 2001). It developed over several evolutionary phases, with the first phase comprising a long period of Triassic-Lower Jurassic magmatic-arc activity. A rupture of the lithosphere occurred in the second phase, while the rift, associated with the opening of the Gulf of Mexico, developed in the third phase (Eguiluz de Antuñano, 2001).

Evaporite, carbonate and detrital formations predominate in the lower basin levels, whereas detrital formations predominate in the upper levels, such as in the San Miguel and Olmos Formations. The Olmos Formation is of great significance because it presents the most exploitable coal seams found in the region (Eguiluz de Antuñano, 2001; Corona-Esquivel *et al*., 2006; González-Sánchez *et al*., 2007). In the study area, the San Miguel and Olmos Formations outcrop, as well as Sabinas Conglomerate and alluvial sediments (SGM, 2003; Figure 1).

The coal deposits are distributed across eight sub-basins (Rivera-Martínez and Alcocer-Valdés, 2003; Figure 1). The most significant because of its extensive size and coal content, the Sabinas sub-basin is the most explored and exploited, containing at least three coal beds, which have been found at depths up to 350 m (SE, 2017).

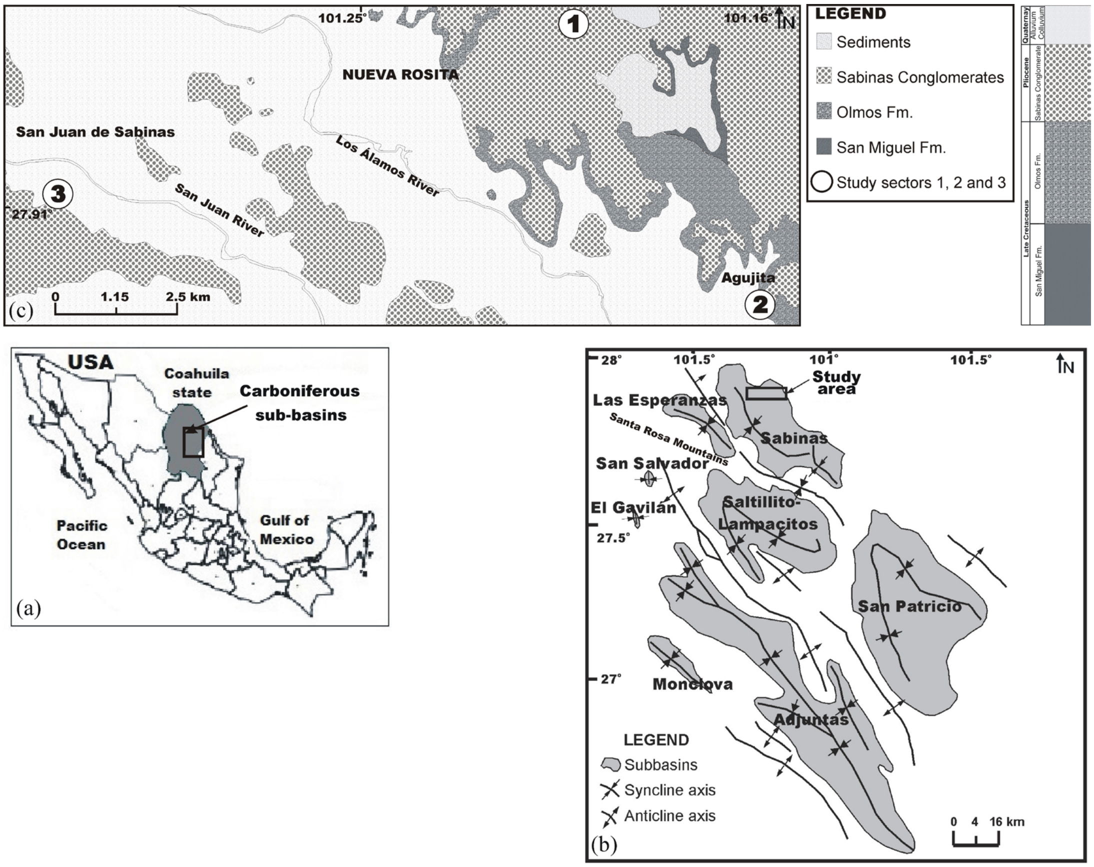

Figure 1. a) Location of carboniferous sub-basins in Northeastern Mexico. b) Carboniferous sub-basins in Northeastern Mexico (modified from Rivera-Martínez and Alcocer-Valdés, 2003). Rectangle indicates location of the study area. c) Geological map of the study area. Original scale 1:50,000 (modified from SGM, 2003). 1, 2 and 3 indicate study sectors.

Coal mining in the Sabinas basin

As mentioned previously, two ways of extracting coal are used in the Sabinas basin, surface and underground mining. The surface mining is carried out as opencast (open pit) mining, mainly. This type of mining is used when the coal outcrops or is located a few meters deep; approximately 20 m (Figures 2a and 2b). In this basin most of the coal is extracted using underground mining with the longwall mining method considering the depths and a tilt of the coal beds. With this mining method the area to be mined is divided into a series of elongate panels accessed from an entry roadway (Figure 3a). In this case, the hydraulic and self-supporting pillars temporarily maintain the roof, while the coal is extracted; later this roof can collapse (Thomas, 2013). The vertical shaft is another method of entry for underground mines (Figure 3b). During the underground mining, when the coal seam is excavated, the vertical stresses above it are generated and they can cause the overburden fails completely and it is transferred to the goaf, generating a subsequent surface subsidence (Figure 4; Van der Merwe and Madden, 2010).

Hydrogeological setting

Two aquifers systems are recognized in the Coahuila coal mining region (CONAGUA, 2015). First system is found in the Early Cretaceous limestones, mainly in the Cupido and Aurora formations located to the southeast of the Santa Rosa Mountains of Coahuila. Several water wells indicate that this aquifer system is the deepest (about 800 m). This aquifer is classified as mainly confined, although there are some sites where limestones outcrop and the aquifer becomes free-type (e.g., Santa Rosa Mountains; Figure 1). The permeability of this aquifer system is related to fractures and the chemical dissolution of rocks.

Second system is formed by shallow aquifers mainly located in Quaternary alluviums and in Sabinas Conglomerates (Pliocene) with a static level from 5 to 15 m. This system includes fractures and weathering zones within the conglomerates and the detrital formation in the upper levels of the Late Cretaceous. Located in granular materials (alluviums and conglomerates), these aquifers are classified as free-type, and semi-confined-type in the Late Cretaceous rocks. Aquifers in the granular materials may seep down through fractures into the Upper Cretaceous Formations (e.g. the Escondido, Olmos, San Miguel, Upson, Austin and Eagle Ford formations, as well as the Washita Group). The Olmos Formation is considered an aquitard because it stores fluids with low permeability (CONAGUA, 2015).

The second aquifer system is of great significance to the study of the cavities generated by mining activity, because some coal seams in the Olmos Formation are located below the static level (Figure 2b), which indicates flooding of the underground galleries.

Data acquisition and processing

Electrical Resistivity Tomography (ERT) data was collected along ten different profiles in areas that have been affected by underground galleries (cavities) in the carboniferous region of Coahuila (Table 1). In order to locate cavities situated under roads, two profiles were set parallel each other and on the roads, close to the principal buildings in order to ascertain infrastructure damage (Figures 5, 6 and 7).

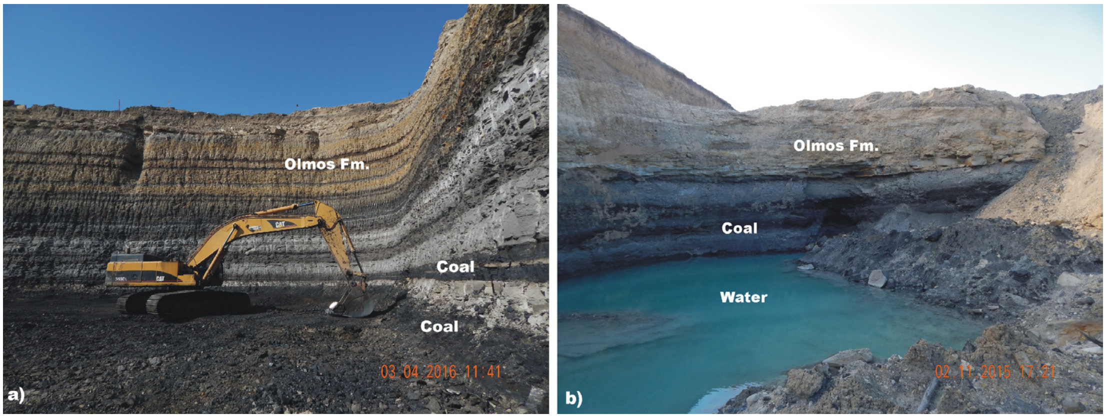

Figure 2. Coal open pit mines in Sabinas basin. a) Coal seams in the Olmos Fm. b) Aquifer cutting coal seams in the Olmos Fm.

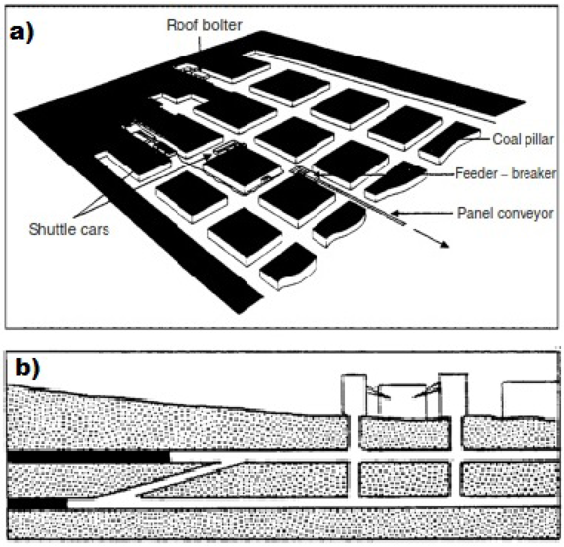

Figure 3. a) Method of mining in underground mine: room and pillar mining (Hunt and Bigby, 1999). b) Method of entry for underground mine: vertical shafts (Ward, 1984).

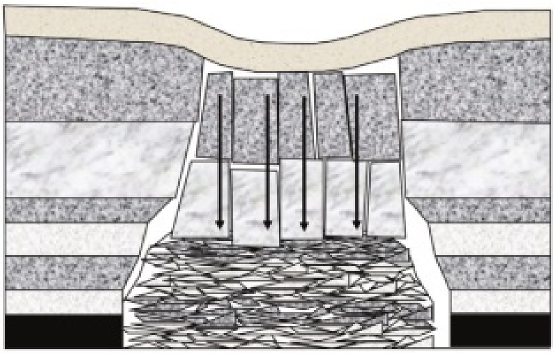

Figure 4. An failed overburden and its load transferred to the goaf. The abutments are stress relieved (Van der Merwe and Madden, 2010).

Table 1. Characteristics of ERT data acquisition. Equipment: AGI SuperSting R1/IP/SP with schlumberger, wenner and dipole-dipole arrays in all profiles. All measurements were carried out with two cycles, maximum current of 2000 mA and measure time of 1.2 s.

Sector	Profile	Length (m)	Spacing of electrode (m)
1	1 (P1)	270	10
	2 (P2)	270	10
	3 (P3)	540	20
	4 (P4)	400	20
2	1 (T1)	270	10
	2 (T2)	270	10
	3 (T3)	270	10
3	1 (G1)	270	10
	2 (G2)	960	20
	3 (G3)	540	20

Figure 5. Study Sector 1. M indicates mining zones. Continuous black lines indicate location of the measurement profile (P1, P2, P3 and P4). Dashed black lines indicate location of the bridge. F1 and F2 indicate the reference point for the photographs shown in figures 9b and 9c. Yellow ellipse indicates a subsidence zone on the road (view photography in Figure 9a). Star indicates well.

Figure 6. Study Sector 2. Continuous white lines indicate location of the measurement profile (T1, T2 and T3). F1 and F2 indicate the reference point for the photographs shown in figures 13a and 13b.

The AGI SuperSting R1/IP/SP was used for data collection (Figure 8) using schlumberger, wenner and dipole-dipole arrays (with 10 m and 20 m electrode spacing), which are the most common arrays used in electrical resistivity tomography.

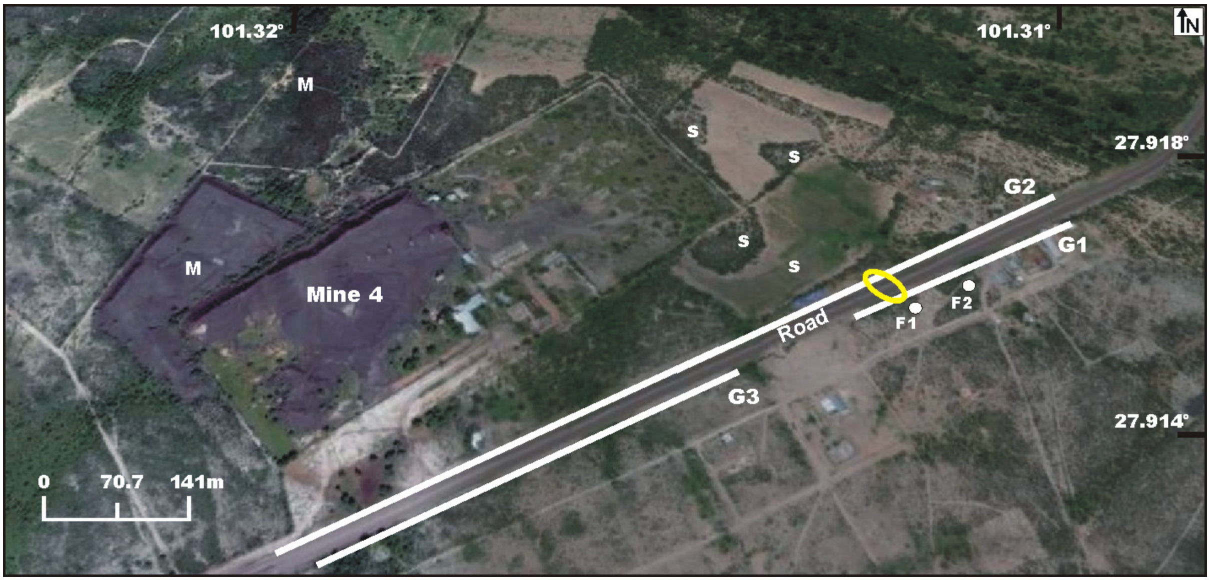

Figure 7. Study Sector 3. Continuous white lines indicate location of the measurement profile (G1, G2 and G3). S indicates areas with a sinkhole. F1 and F2 indicate the reference point for the photographs shown in figures 14c and 14d. Yellow ellipse indicates a subsidence zone on the road (view photography in Figure 14a).

Figure 8. Data collection using the AGI SuperSting R1/IP/SP.

Each ERT array has a specific underground current pattern and it give us a specific apparent resistivity pseudo-section. That means that each ERT array looks the subsurface electrical structures in different way according their currents pattern. When doing the geophysical inversion of a single ERT array, we obtain the estimated underground true resistivity since the point of view of that specific currents pattern. If we try three different ERT arrays, we will have three slightly different versions of the underground according the current patterns of every array. If we do joint inversion of the three arrays, we impose the geophysical inversion that a single model must explain the three data sets. Meaning that the more arrays we use, the better underground model we will obtain (less uncertainty). Because, we are using many currents patterns or many points of view for a single underground reality.

An overlap on the data profiles was created between the lines in P2 on Sector 3 (Figure 7) in order to ensure the continuity of the model and attain a length greater than 540 m. This overlap was achieved using the Roll-along technique, in which the electrode cable advance forward along the measurements profile by moving your cable sections in a leap-frog way. Subsequently, the joint inversion of the three arrays was performed using EarthImager 2D resistivity inversion software developed by Advanced Geosciences, Inc. The software uses a finite element algorithm to compute the estimated real resistivity (model) thought the apparent resistivity data (AGI, 2009), from which a geological explanation for every 2D resistivity model was found (Huebner and Thornton, 1995). The geophysical inversion gives us the resistivity model with a very low or the lowest Root Mean Square (RMS) error value, according the imposed inversion parameters. This RMS error quantifies the difference between the apparent resistivity measured in the field and the apparent resistivity obtained from the response of the 2D resistivity model estimated. In this way, a single resistivity model was obtained for every profile with three datasets (schlumberger, wenner and dipole-dipole).

Results

In order to evaluate how underground coal mining has affected and how it may affect in the future the socio-economic infrastructures (e.g. roads, buildings, bridges, etc.) located within the Sabinas Basin, three study sectors were selected for the measurement of the ERTs. Sectors 1 and 2 were located in a very shallow underground mining area. The first sector has subsidence on the road surface. The third sector was located in a relatively deep underground mining area in which subsidence on the road was also present.

The interpretation of the ERT results aimed; to locate cavities, to show the characteristics of the geological environment that are related to the observed subsidence on the road surface and to guess the probability that this process occurs in the future.

For every profile the water table was obtained from using static level from CONAGUA (2015) of 5 to 15 m, as well as the resistivity values in each ERT.

Sector 1

This sector contains both a road and a bridge support (Figure 5), with subsidence found on the road at the northeast end (Figure 9a), which could be related to the underground coal mining (Peng, 2008) due the shallower mining activities in this sector and its surroundings.

In order to locate and characterize the subsidence-related hazard zones, four ERT profiles (referred as P1, P2, P3 and P4) measured on both sides of the road and at the beginning of the bridge support (Figure 5). The profiles ran on a NE-SW direction of the sector, covering the areas of the road affected by subsidence (profiles 1 and 2, with lengths of 270 m) and other areas where this geological process is not observed (profiles 3 and 4). Conglomerates were found to outcrop in the four profiles (Figures 1, 10 and 11).

The northeastern end of Profile 2 covers the area of the road where subsidence is found (Figure 9a). Two possible cavities are identified with the ERT below the road, at 13 m depth, with both structures presenting different electrical resistivity, size and depth (Figure 10). It can be inferred from the resistivity image that the first cavity is smaller, larger resistivity and partially empty or filled with dry sediments. The second cavity is larger, lower resistivity and filled with either water or water-saturated sediments (Van Schoor, 2002; Zhou *et al*., 2002; Martínez-López *et al*., 2007; Putiska *et al*., 2012). Above these cavities, around 7 m depth, a small size aquifer is located within the Sabinas Conglomerates (CONAGUA, 2015). Above the area that covers both cavities, the road is highly fractured, with some fractures cutting across the entire road (Figures 9b and 9c). The electrical tomography suggests that some of these fractures penetrate into the subsoil, mainly in the area of the second cavity (see the inferred fracture in Figure 10).

Four small cavities are found in the SW end of Profile 2 (Figure 10), located next to the bridge (Figure 5) with subsidence on the road (Figure 9). Two cavities have very low resistivity, while the other two are more resistive, smaller and shallower (approximately 7 m). The cavity found at the center of the profile is clearly the cause of fracturing on the road surface. Moreover, in this zone, the ERT results show at patterns that suggest subsidence, namely, zones of low resistivity (represented by the light gray color) with a convex form (Figure 10).

Profile 1 also shows several cavities from a depth of 7 m onwards, most of which present low values of resistivity and are small in size. Above these cavities water table of about 5 m inside the conglomerates is located. According to the ERT, the geometry of these structures shows patterns of probable subsidence, although no visible deformations are observed on the surface of the roads. These patterns were found in the ERT results for zones with low resistivity and convex shapes with respect to the surface (Figure 10). These zones resemble the characteristic descent into a small basin which is caused by the accumulation of sediments. Towards the northeast of the profile, a large cavity with very low resistivity was observed, extending from a depth of 10 to 50 m (x=110 m). Above this cavity, the road presented no subsidence; however, the ERT showed that it is so close to surface that we expect possible fracturing on surface. We found, in some buildings adjacent to the road fractured walls. All fracture systems observed on the road are perpendicular and oblique to the highway (Figures 9b and 9c), following the probable galleries direction (Peng, 2008). The fracture systems follow three different directions: perpendicular to the road on a NW-SE direction; oblique on a NE-SW direction; and, a NW-SE direction.

While profiles 1 and 2 run paralleled on both road sidewalks, but they have an offset each other (Figure 5). They only coincide until x= 60 m in P2 (Figure 10). For this reason, it is not possible to assess whether the cavities continue on another sidewalks.

Figure 9. Sector 1. a) Image showing the subsidence of the road. b) and c) Image showing fractures on the road surface in profile P2. Arrows indicate location and direction of the fractures. Reference points for the photographs shown in b) and c) are indicated as F1 and F2 in Figure 2, respectively. F1 and F2 also are indicated in Figure 9a.

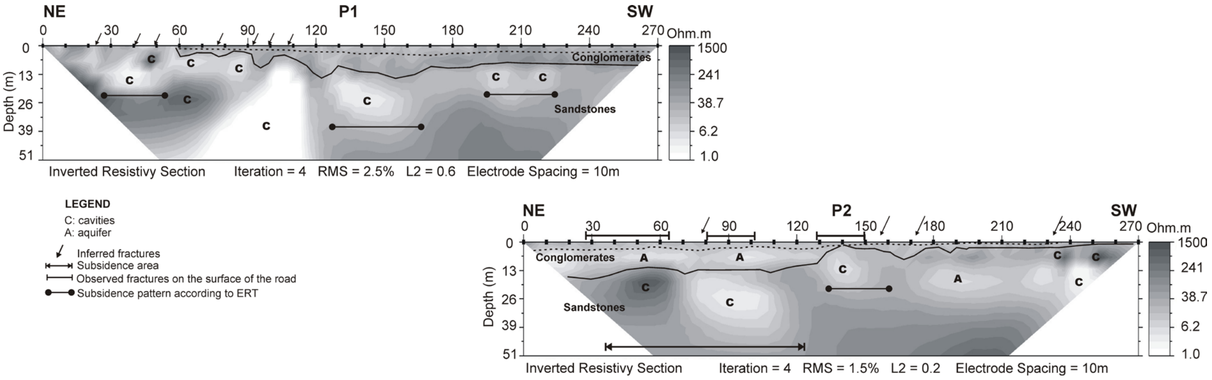

Figure 10. ERT of Sector 1 (profiles P1 and P2). The section of P2 from 170 to 270 m is located next to the bridge. Continuous curved lines indicate boundaries between rocks and discontinuous curved lines indicate water table. The profiles are located graphically according to their position in the field (see Figure 5).

The bridge support is found at the southwest end of the sector, where profiles 3 and 4 were measured (Figure 5) as having lengths of 540 m and 400 m, respectively and their resistivity models are shown in Figure 11. In this zone, the road presented no subsidence and no fractures; however, the ERT results indicate cavities patterns by underground mining activity. These patterns are circular and oval shape and they are located at two depth levels (approximately 22 m and 50 m). Some of these cavities were observed at both sidewalks, indicating that they are connected and cross under the road. All cavities identified are low resistivity (represented by the light gray color). Values lower than 10 ohm-m suggests that the cavity is water-filled (Van Schoor, 2002; Zhou *et al*., 2002; Martínez-López *et al*., 2007;

Putiska *et al*., 2012). This water is provided by the aquifers located in conglomerates and the upper level of the Olmos Fm. (Figure 11). The water table was determined with using a well located in the profile P3 (x=465 m) with a water table at 12 m. Their variations are stablished using resistivity values. Cavities with a resistivity between 30 and 200 ohm-m may be filled with sediments slightly saturated with water (represented by the light gray color; Van Schoor, 2002; Zhou *et al*., 2002; Martínez-López *et al*., 2007; Putiska *et al*., 2012), probably due to cavity collapse. It is possible that some faults or fractures infiltrated water inside the cavities as a first stage and the absence of water as a second stage could cause the collapse itself.

The larger cavities (30 m wide and 25 to 35 m high) identified at a depth larger than 30 m, do not produce visible road deformation; however, this is not a general rule. Some of the zones with probable land subsidence (x=360 m in P3 and x=180 in P4) are related to cavities deeper that the mentioned depth.

It should be noted that, most of the cavities identified are located on both sides of the bridge support. The bridge support itself is located in an area with a large hazard level.

These results suggest that special attention should be paid to both of these areas and to activate a system for monitoring the roads and the bridge integrity in order to avoid damage due the gradual or sudden land collapse.

Sector 2

A road without subsidence is located in this sector, in spite of being located in a zone with many evidences of shallow underground mining activity (Figure 6). ERT results were obtained for both sidewalks of this road. The three parallel profiles are referred as T1, T2 and T3 (Figure 6). Profiles T1 and T2 are on the same sidewalk but have and offset of 10 m, due the heavy truck traffic. While profiles T3 and T1 are parallel and on opposed sidewalks (Figure 6). The 2D resistivity models obtained are shown in Figure 12.

Sediments with a very low resistivity outcrop at the SE end of T1 and they extend to depths larger than 35 m (Figure 12). Electrical resistivity values suggest that these sediments are water saturated, in which the water table oscillates around 5 m, deepening to the NW of the profile T1, according to the resistivity values. Towards the SW end of the profile, conglomerates outcrop and extending to 14 m depth. Several cavities, beginning at a depth of 14 m, are identified in the sandstones underlying the sediments and conglomerates, all of which recorded low resistivity values (Figure 12), indicating that these structures are probably filled with water or water-saturated sediments.

This study identified several fracture systems on the road above the identified cavities (Figure 12), with most of these fractures running perpendicular to the road (Figures

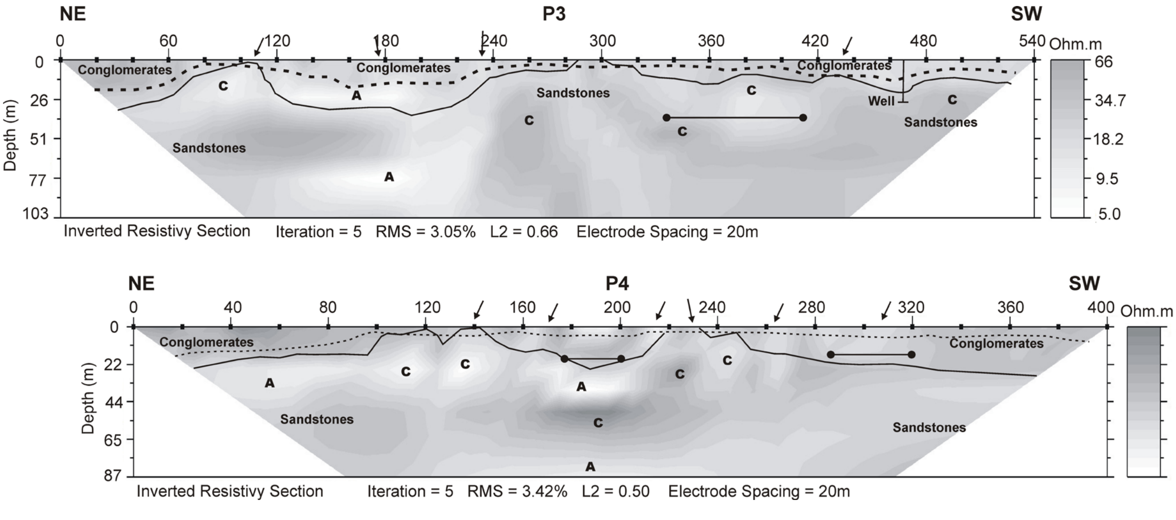

Figure 11. ERT of Sector 1 (P3 and P4). The profiles are located graphically according to their position in the field (see Figure 5). Continuous curved lines indicate boundaries between rocks and discontinuous curved lines indicate water table. The section of P3 from 0 to 280 m and the section of P4 from 0 to 230 m are located next to the bridge. Vertical line indicate well.

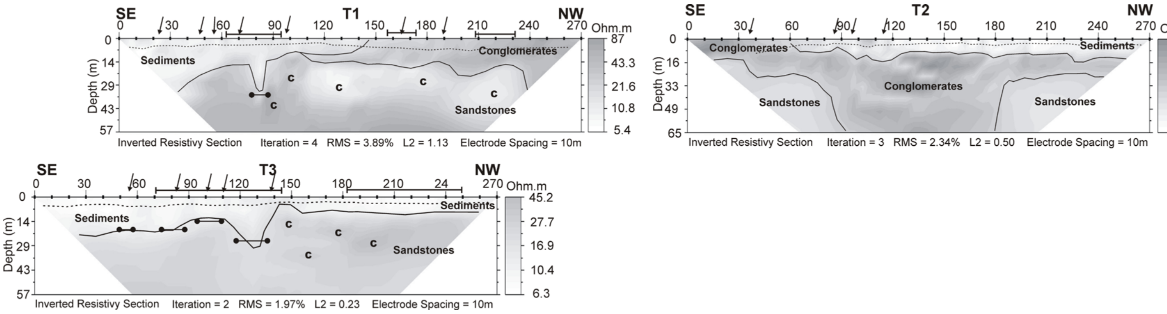

Figure 12. ERT of Sector 2. The profiles are located graphically according to their position in the field (see Figure 6). Continuous curved lines indicate boundaries between rocks and discontinuous curved lines indicate water table.

13a and 13b). The ERT models also present patterns that suggest deep extended fracture systems related to the cavities. Similarly, the ERT model for T1 shows a pattern of probable subsidence with low resistivity (represented by the light gray color) and a convex form, while on the road increases the density of fractures and decreases the spacing between them.

Sediments and conglomerates outcrop in the T1 and T2 models (Figure 12), while ten meters depth, conglomerates cover almost the entire Profile 2 (T2) and raise a thickness of 50 m at the center. No cavities in the central part are identified in the ERT model. This explains why no fractures were found on the road.

Profile 3 (T3) is located on the opposite sidewalk (Figure 12). Only sediments outcrop in Profile 3 and the cavities identified in Profile 1 also appear, suggesting that they are located below the road.

More road fractures were found on the east side than on the west (Figure 13b), which may be related to the outcrop of less competent materials (sediments) on the east side.

Sector 3

This sector includes a road which is located next to an abandoned underground coal mine (Mine 4 in Figure 7), which reached an approximate depth of 350 m. Two sections of extensive subsidence were identified on the road (Figure 14a), related, apparently, to underground mining.

In this sector, three ERTs were also obtained from profiles 1, 2 and 3, referred to here as G1, G2 and G3, respectively, with G1 measured at 270 m, G2 at 960 m, and G3 at 540 m. An overlap was implemented in G2 between the three segments of the line in order to ensure data continuity and, therefore, a 960 m-long continuous resistivity model. Several cavities were also identified in these profiles, most of them larger and deeper than those identified in the previously described sectors (Figure 15). Generally, cavities were identified at a depth of 30 m and reached up to 50 m in diameter.

Conglomerates outcrop the profiles measured in this study, while the ERT results reveal an aquifer (CONAGUA, 2015) attached to the sandstone contact. This aquifer is thicker and wider in lateral extension than those identified in the previous sectors (sectors 1 and 2). Resistivity values indicate that this aquifer has a very variable water table that can exceed 15 of static level reported by CONAGUA (2015). The results of this study permit the inference that cavities can be found at a depth of below 28 m.

Figure 15 shows that, generally, the aquifer level becomes deeper in the zones between the cavities (x=60 m, x=150 m and x=200 m in G1; x=200 m, x=290 m and x=440 m in G2; and, x=300 m in G3). Two of these zones are located just below the subsidence observed on the road (Figure 14a). One zone is located at the SW of G1 and another at around x=200 m in G2, while a third is found at around x=800 m at the SW end of G2 and at 380 m in G3 (Figure 15). In all the zones located between the cavities identified in this study, a high number of fractures were observed on the road (Figures 14b and 15).

Within the sandstones, another aquifer was found at a depth of 100 m below the cavities (Figure 15), in some areas connected to the upper aquifer located at x=200 m, x=460 m, and x=860 m in G2. This finding concurs with the CONAGUA (2015) results, which indicate the connection, through fractures, between the shallow and deep aquifers. These ERT findings indicate a high level of fracturing at depth, which was also identified on the road surface (Figures 14c and 14d). The two zones presenting subsidence on the road surface are located at x=200 m and x=860 m in G2.

Most of the cavities identified in this study present high values of electrical resistivity, indicating that they are not water-filled and, instead air-filled or partially filled with sedimentary materials (Martínez-López *et al*., 2007; Putiska *et al*., 2012). These materials may be associated with the ceiling collapses that have occurred in the mining structures.

Discussions

Analysis of the ERT 2D models of the profiles measured in this study reveals several cavities, some located below the roads. The resistivity values in those structures suggest that they may either be empty or filled with water sediments. The road surface located above some of the cavities (sectors 1 and 2) presents a fracture system, apparently induced by the soil instability found around the cavities (Peng, 2008). Similarly, these fractures may also cause cavities to fill with water and wet sediments. The movement of groundwater into the cavities, the empty space of the cavities themselves or their collapse can cause geometrical deformation and the sinking of the land. This process is accelerated on the road surface due to the lithostatic pressure exerted on the cavities by the weight and vibration of the vehicles that circulate on the roads above on a daily basis.

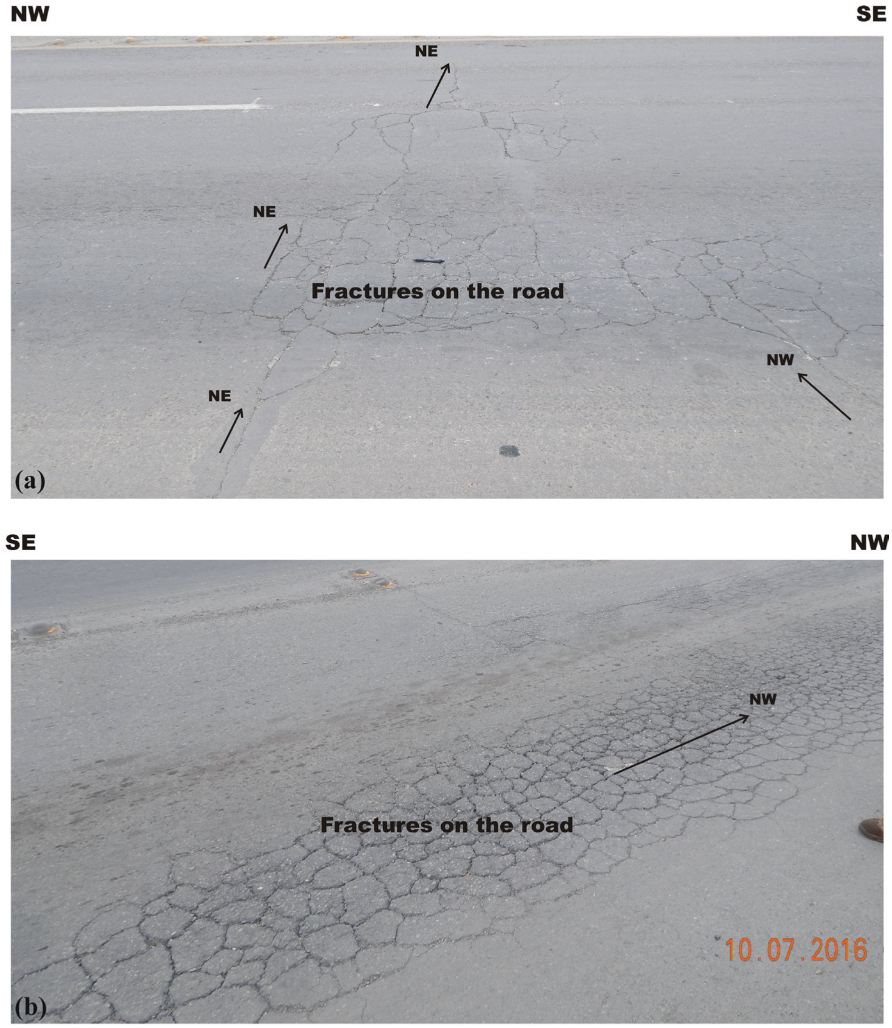

Figure 13. Images of fractures with signs of subsidence on the road surface in Sector 2. a) Profile T1. b) Profile T3. Arrows indicate location and direction of the fractures. Reference points for the photographs shown in a) and b) are indicated as F1 and F2 in Figure 6, respectively.

Cavity flooding can change the hydrodynamic groundwater regime, deepening the water table and modifying its natural flow. This can cause a loss of pore pressure in granular materials (e.g., alluviums and conglomerates) and generate land subsidence (Galloway and Burbey, 2011). Changes in the hydrodynamic groundwater regime not only disrupt the infrastructure (e.g., roads and bridges) but can also affect economic activities that depend on the use of water, as with livestock and agriculture.

Considering that road repairs have been carried out in some of the study sectors and, perhaps, due to land subsidence, it is possible that some of the subsided zones indicated by the ERT results, namely, zones of low resistivity (represented by the light gray color) and convex in form, have been previously filled with construction materials. For this reason, the evidence of sinking was erased, meaning that these areas can be considered areas of old subsidence.

Analysis of the ERT models for the 3 sectors shows some areas where no surface subsidence is present even when a cavity is located below. In these cases, it is possible that the relationships between the dimensions, depths and characteristics of the rocks (some which may be more competent than others) have not permitted subsidence to occur on the road surface. However, this study found various fracture systems directly related to these cavities on the most of the road surfaces examined. These fracture systems run in a transverse direction to the roads and, sometimes, completely cross them, for which reason, they were used as an indicator of a sinking process caused by underground coal mining (Bruhn *et al*., 1978; Peng, 2008). There is the possibility of an increase in these deformations over time, due to the weakening in the geological structures below the roads, as caused by the constant movement of vehicles above.

The subsidence patterns observed in Sector 3 are different from those found in sectors 1 and 2, in that, in Sector 3, the subsidence on the road surface occurs between two identified cavities rather than above them, as found in sectors 1 and 2. According to the ERT models generated for Section 3, the sinking seems to be related to the deepening of the aquifer level between two cavities. The cavities observed in Sector 3 are generally larger and deeper. Therefore, it is assumed that the fracture systems and subsidence patterns are related to the change in the hydrodynamic groundwater regime, probably caused by the water flow toward the underground galleries which is generated by deeper-level underground mining activities (occurring after 350 m). Once the underground cavities have been created, the underground water inside them is displaced, deepening the phreatic level. The conglomerates undergo a compaction process over time, leading to subsidence. At the NE end of Sector 3 (Figure 7), several sinkholes are observed (Figure 14b), indicating the existence of underground cavities generated by mining.

Figure 14. Sector 3. a) Image showing the subsidence of the road. b) Image of a sinkhole next to the road. c) and d) Images of fractures on the road surface in Profile P1. Reference points for the photographs shown in c) and d) are indicated as F1 and F2 in Figure 7, respectively.

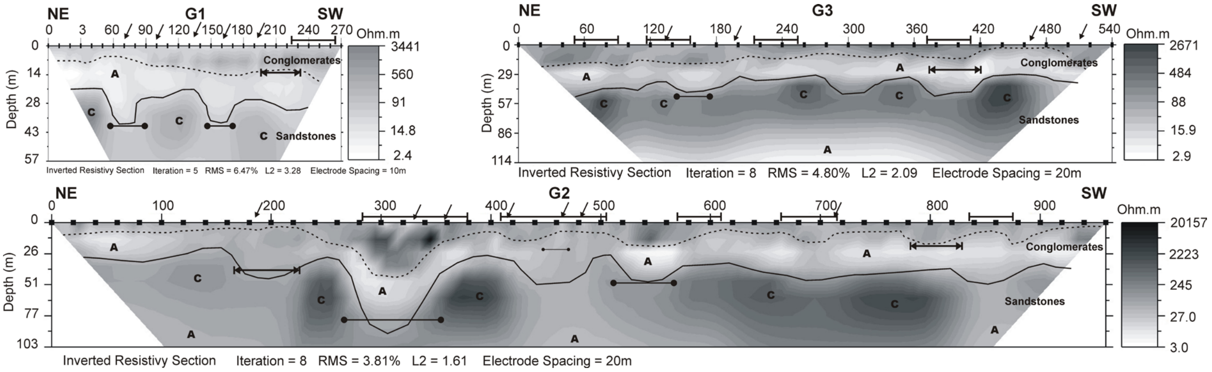

Figure 15. ERT of Sector 3. The profiles are located graphically according to their position in the field (see Figure 7). Continuous curved lines indicate boundaries between rocks and discontinuous curved lines indicate water table.

The fracture systems on the road surface in Sector 3 are found above the depressed zones identified, indicating the relationship between the two processes. The cavities present high resistivity values, indicating that they were not flooded by water from the upper level aquifer. The movement of groundwater can occur at lower levels, where cavities are larger and are related to the deepest mining activities (located at a depth of 350 m). According to CONAGUA (2015), the aquifers embedded in the granular materials of the Cenozoic (e.g., the Sabinas Conglomerates) may be connected through fracture systems with the Upper Cretaceous Formations (e.g., the Olmos Fm.).

The fracture systems observed on the road surface, the cavity patterns revealed by the ERT models in the three sectors, and the morphology of the aquifers suggest several potential hazard zones caused by the subsidence of the land in the study region.

According to the analysis carried out on the entire set of ERT resistivity models, there are several factors generating land subsidence due to the underground cavities. The main factors are: the size and depth of the cavity, the material with which it is filled or whether or not it is filled at all; the rock type and the level at which it fractures; and, the presence of an aquifer and their depth and thickness. When the cavities are empty, larger in size and not as deep, the hazard of subsidence increases, as it does if the cavity is located in rock that is non-competent and/or with a high propensity to fracture. Similarly, the presence of large aquifers above these cavities, combined with fractured or faulted rocks, will change the hydrodynamic groundwater regime and increase the hazard of subsidence.

Conclusions

Analysis of the ERT models applied to the three sectors from the northern end of the Sabinas Basin reveals cavities generated by underground coal mining. Some of these cavities have caused subsidence and a fracture system on the road surface, and damage to the surrounding buildings. These ERT models also show other characteristics of the geological environment caused by the fractures and the sinking of the roads, such as the decrease in the level of the aquifers, the fractures and faults that affect the stratigraphic sequence, and the layering of some strata (zones of low resistivity with a convex form) that show prior subsidence. According to the analysis carried out, the subsidence observed in Sector 1 is mainly related to very shallow cavities generated by shallow underground mining, whereas the subsidence in Sector 3 is related to the decrease in the level of the aquifers, as caused by changes in the hydrodynamic regime of the underground water, which is linked to deep-level mining activities. The distribution and characteristics of the cavities identified in the three sectors, as well as the geological characteristics inferred, suggest that the areas containing the profiles measured by this study are potentially hazardous. Fracture systems observed on the road surface without subsidence and located above the cavities identified via ERT are indicators of the initial stage of the deformation on the roads, as related to the process of subsidence.

Acknowledgments

We thank the University Autonomous of Coahuila and CICESE for its support of this research.

References

Advanced Geosciencies, Inc (AGI), 2009, Instruction Manual for EarthImager. Version 2.4.0. Resistivity and IP Inversion Software, 139 pp.

Bruhn, R.W., Magnuson, M.O., Gray, R.E., 1978, Subsidence over the mined-out Pittsburgh Coal. A.S.C.E. Convention ´Coal Mine Subsidence´ session, Pittsburgh, Pa, USA, April, pp. 26-55.

Comisión Nacional del Agua (CONAGUA), 2015, Actualización de la disponibilidad de media anual de agua en el Acuífero Región Carbonífera (0512), Estado de Coahuila. 27 pp. https://www.gob.mx/cms/uploads/attachment/file/102852/DR_0512.pdf. 06-10-2016.

Corona-Esquivel, R., Tritlla, J., Benavides-Muñoz, M.E., Piedad-Sánchez, N., Ferrusquía-Villafranca, I., 2006, Geología, estructura y composición de los principales yacimientos de carbón en México. *Boletín de la Sociedad Geológica Mexicana*, 57, 141-160.

Chugh, Y.P., 2018, Concurrent mining and reclamation for underground coal mining subsidence impacts in China. *International Journal of Coal Science & Technology*, 5(1), 18-35.

Galloway, D.L., Burbey, T.J., 2011, Review: regional land subsidence accompanying groundwater extraction. *Hydrogeology Journal*, 19, 1459-1486.

Eguiluz de Antuñano, S., 2001, Geologic evolution and gas resources of the Sabinas Basin in northeastern Mexico. In Bartolini, C., Buffler, R.T., Cantú-Chapa, A., (eds.), The western Gulf of Mexico Basin: Tectonics, sedimentary basins, and petroleum systems. *AAPG Memoir*, 75, 241-270.

González-Sánchez, F., Puente-Solís, R., González-Partida, E., Camprubí, A., 2007, Estratigrafía del Noreste de México y su relación con los yacimientos estratoligados de fluorita, barita, celestina y Zn-Pb. *Boletín de la Sociedad Geológica Mexicana,* 59, 43-62.

Huebner, K.H., Thornton, E.A., 1995, The finite element method for engineers, John Wiley and Sons.

Hunt, K., Bigby, D., 1999, Designing for success. *World Coal*, 8(7), 47–52.

Martínez-López, J., Rey, J., Sandoval, S., Rodríguez, M., 2007, Electrical resistivity tomography: a tool to aid in the detection of mining voids (Arrayanes mine, Linares-Jaén). *Geogaceta*, 42, 43-46.

Militzer, H., Rösler, R., Lösch, W., 1979, Theoretical and experimental investigations for cavity research with geoelectrical resistivity methods. *Geophysical Prospecting*, 27, 640–652.

Peng, S., 2008, Coal Mine Ground Control, Third Edition. 764 pp.

Putiska, R., Nikolaj, M., Dostal, I., Kusnirak, D., 2012, Determination of cavities using electrical resistivity tomography. *Contributions to Geophysical and Geodesy*, 42, 201-211.

Rivera-Martínez, J. C., Alcocer-Valdés, C., 2003, La situación actual del aprovechamiento del carbón en el estado de Coahuila. *Boletín* Técnico de*l Consejo de Recursos Minerales*, 9, 2-19.

Secretaria de Economía (SE), 2017, Perfil del mercado del carbón. Coordinación General de Minería. Dirección General del Desarrollo Minero. Secretaría de Economía, México. 44 pp. https://www.gob.mx/cms/uploads/attachment/file/287796/Perfil_Carbon__2017.pdf.

Serrano-González, E., 2014, Identificación de riesgos geológicos ocasionados por la minería subterránea del carbón, en la cercanía de la Colonia Maseca, a partir de mediciones geoeléctricas. Tesis de licenciatura. Universidad Autónoma de Coahuila. 85 pp.

Servicio Geológico Mexicano (SGM), 2003, Carta geológico-minera Nueva Rosita G14-A13. Coahuila. Escala 1:50,000.

Strozik, G., Jendrus, R., Manowska, A., Popczyk, M., 2016, Mine Subsidence as a Post-Mining Effect in the Upper Silesia Coal Basin. *Pol. J. Environ. Stud*, 25(2), 777-785.

Thomas, L., 2013, Coal geology. Second edition. John Wiley & Sons. 444 pp.

Van der Merwe, J.N., Madden, B.J., 2010, Rock engineering of underground coal mining. Second edition. The Southern African Institute of Mining and Metallurgy. 259 pp.

Van Schoor, M., 2002, Detection of sinkholes using 2D electrical resistivity imaging. *Journal of Applied Geophysics*, 50, 393-399.

Ward, C.R., 1984, Coal Geology and Coal Technology. Blackwell Scientific Publications, Oxford, 345 pp.

Zhou, W., Beck, B.F., Adams, A.L., 2002, Effective electrode array in mapping karst hazards in electrical resistivity tomography. *Environ. Geol.*, 42, 922-928.

Geofísica Internacional (2019) 58-4: 295-315

Original paper

Unidades oceanográficas del Golfo de México y áreas adyacentes: La integración mensual de las características biofísicas superficiales

Oceanographic units of Gulf of Mexico and adjacent areas: The monthly integration of surface biophysical features

Uribe-Martínez, A.*, Aguirre-Gómez, R., Zavala-Hidalgo, J., Ressl, R. y Cuevas, E.

Received: November 14, 2018; accepted: July 09, 2019; published on line: October 01, 2019

Resumen

El Golfo de México (GoM) es una región oceánica de una dinámica y complejidad particular, que se evidencia en las variaciones espacio temporales de la configuración de sus aguas superficiales. Varios estudios han utilizado las características superficiales térmicas, biológicas o de circulación para proponer subdivisiones estáticas del GoM; sin embargo, ninguna investigación ha regionalizado la zona integrando distintos aspectos oceanográficos de forma dinámica. El objetivo de este trabajo fue proponer una división del GoM que considerara las características físicas y biológicas y que permitiera analizar la evolución mensual espacial de las unidades en un año promedio. Utilizamos análisis multivariados para reconocer la estructura subyacente de los datos, para generar una expresión espacial mensual de los conglomerados y para probar la robustez de los resultados. Se obtuvieron 18 regiones denominadas unidades oceanográficas (UO) que condensan diversas características superficiales del GoM. Se observaron dos grupos de UO: aquellas que están relacionadas con las propiedades de circulación y aquellas que fueron definidas por la asociación de las características biológicas y térmicas. Quince UO están presentes a lo largo del año, mientras que dos tienen presencia únicamente en verano. Todas las UO tienen variaciones temporales tanto en sus características biofísicas como en su expresión espacial. Este estudio propone una manera novedosa de particionar un sistema marino y aporta parámetros cuantitativos interpretables de las UO propuestas. La representación de la variabilidad de unidades oceanográficas homogéneas provee información valiosa para el manejo diferenciado de recursos marinos asociados temporalmente a masas de agua especificas. Los resultados obtenidos proveen también bases robustas para analizar de manera condensada la dinámica de largo plazo de un sistema tan complejo como es el GoM.

Palabras clave: Regionalización marina, análisis espacio-temporal, oceanografía satelital.

Uribe-Martínez, A.*
Posgrado en Geografía
Instituto de Geografía
Universidad Nacional Autónoma de México
Circuito de la Investigación Científica
Cd. Universitaria, C.P. 04510
Ciudad de México
**Corresponding author: abigailum@gmail.com*

Aguirre-Gómez, R.
Instituto de Geografía
Universidad Nacional Autónoma de México
Circuito de la Investigación Científica
Cd. Universitaria, C.P. 04510
Ciudad de México

Zavala-Hidalgo, J.
Centro de Ciencias de la Atmósfera
Universidad Nacional Autónoma de México
Circuito de la Investigación Científica
Cd. Universitaria, C.P. 04510
Ciudad de México

Ressl, R.
Comisión Nacional para el Conocimiento
y Uso de la Biodiversidad
Liga Periférico - Insurgentes Sur #4903
Tlalpan, 14010
Ciudad de México

Cuevas, E.
Universidad Autónoma del Carmen
Calle Laguna de Términos S/N
Renovación 2da Sección, 24155
Cd. del Carmen, Campeche

Abstract

The Gulf of Mexico (GoM) is a large marine ecosystem that has unique oceanographic dynamics, as it shows important spatio-temporal variations in the configuration of its surface waters. Several studies have used the thermal and biological features to subdivide the GoM, while other had provided subdivisions using circulation features. Nevertheless, none of those works have produced a dynamic regionalization that consider biological and physical features of the GoM simultaneously. The goal of this work was to propose a dynamic division of the GoM which considers physical and biological features and to analyze the monthly spatial evolution of regions in an average year. We used statistical multivariate analysis to recognize the underlying structure of the data, to generate a monthly expression of clusters and to test the robustness of the achieved regionalization. We obtained 18 regions called oceanographic units (UO) that merged unique surface characteristics of the GoM and that had a monthly spatial configuration. We observed two main groups of UO: those that are mainly related with circulation properties and those that were defined by its biological and thermal associations. Fifteen UO were present all year long, while three of them were only present some months. All UO have monthly internal variations and their boundaries displayed seasonal spatial variation; however, they remained well differentiated from each other. This study offers a novel way to divide an oceanic system, which provides quantitative and pragmatic parameters that can help to develop monitoring systems considering the intrinsic ocean dynamics. The information about oceanographic unit variability provides valuable information to promote marine resources management, in concordance to their temporal association with certain water masses. These results also provide the basis to analyze interannual variations of oceanographic units to offer information about the sea surface dynamics and to help understanding a complex system such as Gulf of Mexico.

Key words: Marine regionalization, spatio-temporal analysis, satellite oceanography.

Introduction

La regionalización de los océanos ha sido una forma de estudiar grandes porciones de mar desde hace varias décadas, con aproximaciones, interpretaciones, insumos y sobre todo objetivos distintos (Esaias *et al.,* 2000; Yáñez-Arancibia y Day, 2004; Longhurst, 2006). Los diversos enfoques para regionalizar los mares han servido de base para otras propuestas de organización de grandes extensiones marinas de acuerdo con sus características físicas, químicas o biológicas.

El Golfo de México (GoM) ha sido objeto de diversas divisiones que han abordado aspectos de su oceanografía de forma independiente. Los primeros trabajos se enfocaron en una visión estática del ecosistema (Yáñez-Arancibia y Day, 2004; Zavala-Hidalgo y Fernández-Eguiarte, 2006). Otros trabajos han considerado la variación espacio temporal de parámetros físicos y biológicos como en Salmerón-García *et al.* (2010), donde, a partir de un análisis de la concentración de clorofila *a* derivada de imágenes SeaWiFS, obtuvieron 14 regiones con patrones temporales diferenciables a partir de un análisis de componentes principales. Por su parte, Callejas-Jiménez *et al.* (2012) propusieron una regionalización de 11 regiones clasificadas en provincias oceánicas y costeras, diferenciadas a partir de la razón entre las bandas azul y verde de imágenes MODIS.

Más recientemente, Miron *et al.* (2017) presentaron una propuesta de la geografía dinámica lagrangiana del GoM a partir de un análisis de una gran colección de datos provenientes de boyas de deriva. En este estudio que integra de manera condensada la variabilidad temporal de la circulación, se reconocieron siete regiones entre las que se estima que el intercambio de partículas sea muy bajo, mientras que al interior de cada región se prevé que sea más intenso.

La delimitación oceánica del GoM ha sido un reto, debido a que sus características oceanográficas tienen un comportamiento altamente dinámico (Muller-Karger *et al.,* 2015). El GoM es una cuenca semicerrada cuya dinámica oceanográfica tiene una fuerte influencia de las aguas que ingresan del Mar Caribe por el canal de Yucatán. A su vez, la salida de agua del interior hacia el Atlántico a través del canal de Florida, tienen influencia en las características oceanográficas de la costa oeste de Estados Unidos (Fiechter y Mooers, 2007).

Una de las características de circulación es la corriente del Lazo, la cual presenta grandes variaciones de forma, extensión y penetración al interior del GoM, y que suministra una amplia gama de giros y remolinos que se desprenden de ella (De la Lanza-Espino, 2004). A pesar de que el GoM tiene un ciclo térmico estacional marcado (Muller-Karger *et al.,* 1991), existen diferencias de la amplitud de los rangos térmicos entre regiones con variaciones intra-anuales muy marcadas en la zona norte, en contraste con las mínimas diferencias estacionales que se presentan al sur (Muller-Karger *et al.,* 2015).

El GoM es considerado como una ecoregión de productividad moderada (Heileman y Rabalais, 2009), pues cuenta con importantes aportes de nutrientes provenientes de las descargas de ríos como el sistema Grijalva-Usumacinta y el Misisipi-Atchafalaya. Aunado a esto, en las zonas de la plataforma y talud continental se observan las mayores concentraciones de clorofila mientras que en la zona oceánica, con menores concentraciones se han detectado variaciones estacionales y asociadas los giros de mesoescala (Muller-Karger *et al.,* 1991).

Las diversas regionalizaciones que se han planteado han servido de base para diferentes propósitos, como proveer información para el manejo integrado de regiones marinas (Córdova *et al*., 2009, Wilkinson, 2009), o como base para estudios ecosistémicos integrados (Roff *et al*., 2003; Yáñez-Arancibia *et al*., 2013). Sin embargo, también se ha reconocido que los esfuerzos de monitoreo y manejo dependen de los componentes que pueden ser observados y medidos de manera continua, los cuales pueden utilizarse como aproximaciones o sustitutos para la identificación de características claves de los ecosistemas (Zacharias y Roff, 2000, Roff y Zacharias, 2011). Observar la dinámica espacial y temporal de las regiones, así como su variabilidad estacional resulta fundamental para conocer cómo estas variaciones se asocian a la disponibilidad de recursos de interés comercial o de conservación, y con ello proveer mejores esquemas de manejo y protección (Longhurst, 2006; Díaz de León *et al.*, 2009).

Hasta ahora las regionalizaciones del GoM han ofrecido distintas subdivisiones, físicas y biológicas que aportan elementos independientes para distinguir configuraciones estáticas del paisaje. Estos planteamientos estáticos han omitido las diferentes configuraciones espaciales que una masa de agua de características similares puede tener en diferentes épocas del año. A pesar de que algunas regionalizaciones del GoM han involucrado la dinámica temporal (Miron *et al.,* 2017), ninguna había presentado las variaciones espacio temporales de las regiones o la aparición de conglomerados distintos a las condiciones circundantes, como en el caso de las surgencias estacionales o las aportaciones de agua fría, rica en nutrientes provenientes de los ríos. En contraparte, en el presente trabajo proponemos una subdivisión dinámica del GoM, en la que se realiza la integración de parámetros tanto biológicos como físicos, a la vez que se analizan las distintas configuraciones espacio temporales de los segmentos obtenidos.

La percepción remota ha contribuido significativamente en el análisis de procesos ecológicos a escalas regionales, por lo que varias aproximaciones han abordado el tema de las provincias marinas con base en el análisis de imágenes satelitales (Esaias *et al.,* 2000; Saraceno *et al.,* 2006; Palacios *et al.,* 2006; Hobday *et al.,* 2011). Por su parte, el modelado numérico permite entender la dinámica oceánica o bien predecir el movimiento de las masas de agua, sin que hasta el momento se hayan utilizado para delimitar regiones marinas. Ambas técnicas de observación y análisis proveen información integral de las condiciones del GoM, y que al analizarse en conjunto permiten tener un panorama sinóptico y multitemporal.

El objetivo de este trabajo fue identificar unidades oceanográficas del GoM equiparables mensualmente a partir de la integración de datos biofísicos derivados de percepción remota y modelado numérico y analizar su dinámica en un año promedio. En este trabajo se define una *unidad* como una entidad de características biofísicas superficiales similares e indivisibles con un conjunto de datos dados a una escala fija (IOCCG, 2009). Se presentan los métodos utilizados para encontrar la estructura de los datos, la definición ambiental de las unidades obtenidas y el análisis de sus variaciones espacio temporales.

Este trabajo presenta una forma novedosa de particionar una región de alto interés económico y ecológico al integrar distintos aspectos oceanográficos. Con ello se proponen provincias marinas que incorporan aspectos que influencian o incluso definen la configuración de hábitats y ecosistemas marinos y que no son estáticos a lo largo del tiempo. La visión de este trabajo es establecer un precedente para monitorear la evolución de las unidades oceanográficas a lo largo del tiempo y con ello aportar elementos cuantitativos de sus anomalías en el mediano plazo.

Materiales y Métodos

El área de estudio comprende el GoM, entre los 98°O, 30.5°N y los 78°O, 18°N, donde se incluyen las zonas de influencia de la trinchera del Caimán y la salida de agua hacia el Atlántico (Figura 1).

Los insumos utilizados para los análisis se obtuvieron de diversos productos satelitales y de modelado numérico que se describen a continuación.

Moderate Resolution Imaging Spectroradiometer (MODIS).

En México, la Comisión Nacional para el Conocimiento y uso de la Biodiversidad procesa los productos oceanográficos del sensor Aqua-MODIS a una resolución espacial de 1 km para México (Cerdeira-Estrada y López-Saldaña, 2011). De aquí se obtuvieron los compuestos mensuales de los productos: Temperatura superficial del Mar Nocturna (NST), Concentración de la Clorofila *a* (CLO) y altura de la línea de fluorescencia (FLH) de enero de 2003 a diciembre de 2013 (CONABIO, 2014).

Archiving, Validation and Interpretation of Satellite Oceanographic data (AVISO).

Es un sitio que distribuye los productos del proyecto Ssalto/Duacs.

En este acervo se realiza la unificación de productos de altimetría de distintas misiones (Saral, Cryosat-2, Jason-1*y*2, Topex/Poseidon, Envisat, GFO, ERS-1 *y* 2, Geosat). De aquí se obtuvo la topografía dinámica del mar (ADT) de enero de 2003 a diciembre de 2013 en promedios mensuales rasterizados. Se utilizó el conjunto DUACS 2014 procesado con un período de referencia del 1993-2012, a una resolución espacial de ¼ de grado (AVISO, 2016).

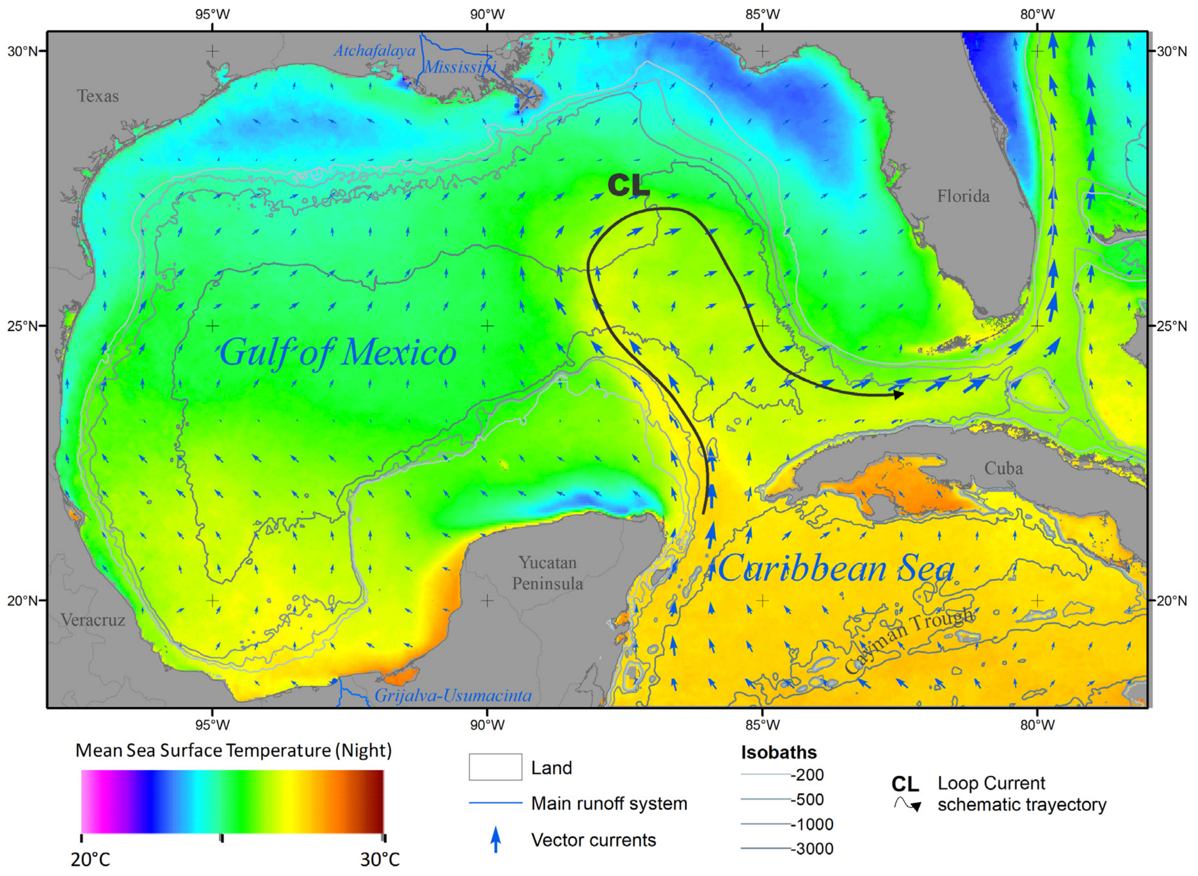

Figura 1. Área de Estudio con el promedio climatológico para el mes de mayo de la temperatura nocturna de la superficie del mar (NST) con los vectores resultantes de la circulación superficial para el mismo mes (flechas azules). En tonos de gris se sobreponen las isobatas más representativas (tonos de gris) y las entradas de los principales afluentes de los sistemas Grijalva-Usumacinta y Atchafalaya-Misisipi. Se presenta un esquema de la trayectoria típica de la Corriente del Lazo (flecha en negro).

Modelo oceánico de coordenadas híbridas (HYCOM).

El consorcio multiinstitucional HYCOM desarrolla modelo numérico de circulación oceánica híbrido generalizado con asimilación de datos llamado HYbrid Coordinate Ocean Model (Halliwell, 2004). Los modelos HYCOM permiten que las regiones poco profundas y costeras sean modeladas considerando un sistema coordenado de terreno que incorpora fronteras laterales y batimétricas, mientras que en el océano abierto utiliza un sistema de coordenadas Z en la capa de mezcla y se ajusta suavemente a un sistema de coordenadas isopícnicas por debajo de esta, donde el flujo de las corrientes sigue superficies de igual densidad. Este modelo permite la evolución dinámica de las coordenadas verticales tanto en tiempo como en espacio, lo que hace que HYCOM sea una buena opción para aplicarlo en dominios que incluyen tanto océano abierto como aguas poco profundas. El modelo también utiliza el sistema de asimilación de datos NCODA (Navy Coupled Ocean Data Assimilation) que incorpora altimetría satelital, altura promedio de la superficie del mar, forzamientos atmosféricos y temperatura superficial del mar (HYCOM, 2017). Particularmente, el experimento sobre el Golfo de México genera una simulación de 1/25° de resolución espacial del que se obtuvieron los experimentos 20.1 (datos del 2003 al 2009) y 31.0 (datos de abril del 2009 a diciembre de 2013) (HYCOM, 2017). La resolución horizontal relativamente alta esta adaptada para estudiar la dinámica de la Corriente de Lazo y los giros y remolinos que se desprenden de ella. Aunque se han documentado deficiencias del modelo en resolver la frontera entre el océano y la plataforma (Le Hénaff *et al*., 2012), sale de los alcances de esta investigación analizar las interacciones entre estructuras de mesoescala.

De este conjunto de datos se descargaron los componentes U y V de la representación vectorial de la corriente superficial (CSU y CSV) y la resultante de la magnitud a 0m (CSMag), al igual que la salinidad superficial (SAL), todos ellos en promedios diarios.

Preprocesamiento de insumos

Para el caso de los productos derivados de modelos de circulación HYCOM, se construyeron composiciones mensuales ya que originalmente se generan como un panorama instantáneo de forma diaria.

A partir de la serie de tiempo de promedios mensuales del 2003 al 2013, se generaron compuestos climatológicos mensuales (promedio aritmético) de todos los parámetros en su resolución original. En el caso de la ADT, los pixeles se disgregaron en seis partes iguales para aumentar artificialmente la resolución a 4.16 km, conservando su valor original.

Para homologar todos los rasteres en términos del origen, resolución espacial (4 km), número de pixeles y proyección cartográfica, se realizó un remuestreo con una interpolación por el vecino más cercano (Li y Heap, 2008). Para el caso de CLO y FLH se realizó una transformación reciproca de la forma $x'=x^{-1}$ (donde x es el valor original del pixel) para simetrizar la distribución de las variables ya que están fuertemente sesgadas hacia valores pequeños. Esta transformación permite mantener la interpretación de las variables (en sentido opuesto), con un efecto en la distribución de los valores, al comprimir los más altos y expandir los bajos, lo que favorece la diversificación de los datos para la posterior segmentación (Quevedo-Urías y Pérez-Salvador, 2014).

Estructura de datos

Como requisito para utilizar los algoritmos de agrupación, los datos se estandarizaron para minimizar errores de agrupamiento derivados de las diferentes escalas de las unidades utilizadas. Se generaron diferentes clasificaciones no supervisadas utilizando el algoritmo *k-means* (Jain, 2010) con el método de Hartigan and Wong implementado en la función *kmeans* de *R* (Everitt y Hothorn, 2016) para encontrar la estructura de los datos con base en la homogeneidad de las variables. En cada escenario se evaluó la variabilidad óptima dentro y entre grupos, la coherencia espacial y la aportación de las variables a la separación de las clases. Este proceso se realizó de forma iterativa, hasta lograr un resultado que permitiera el reconocimiento de clases de manera consistente intermensualmente, es decir, que las clases obtenidas fueran equiparables entre meses. Para obtener el número de clases adecuado para cada conjunto de datos mensual, se generaron clasificaciones no supervisadas de entre 3 y 20 clases. Se determinó cuál representaba el menor cambio en la variación entre las clases, que fue evaluado como la suma total de cuadrados del error dentro de cada grupo (Tan *et al*., 2018).

De forma independiente para cada conjunto de datos mensual, se obtuvieron métricas de disimilitud entre los centros de clase (Tan *et al*., 2018). Se evaluó la separabilidad de las clases mediante la distancia euclidiana del conjunto de los promedios de los parámetros biofísicos. También se realizó un análisis de agrupamiento jerárquico con el método de mínima varianza expresado en dendogramas (Gotelli y Ellison, 2004). De esta forma, se agruparon las clases con características similares y que presentaran dificultad para separarse espacialmente y se mantuvieron aquellas clases con disimilitudes constantes.

Definición ambiental de unidades oceanográficas

La definición ambiental se conceptualizó como el conjunto de características que diferencian de forma única a una clase. Tal definición se establece como el promedio y desviación estándar mensual de los parámetros biofísicos que la distinguen del resto de las clases obtenidas con el proceso no supervisado. Para lograrlo, se realizó un proceso iterativo de depuración, de tal forma que las curvas de valores mensuales de cada parámetro fueran consistentes y definieran cada clase de manera única a lo largo del año. Particularmente, las variables de circulación se manejaron como constantes en todos los meses para todas las clases, ya que no presentaron evidencia de variar estacionalmente.

Las clases depuradas y definidas ambientalmente se denominaron *unidades oceanográficas* (UO), en donde cada UO se diferencia del resto en al menos uno de los parámetros. A fin de mantener la estabilidad en la definición ambiental de las UO a lo largo del año, se buscó que se mantuviera una relación constante entre sus parámetros con el resto de las UO. Para visualizar la definición ambiental mensual, se utilizaron diagramas de caja y bigote.

Para cuantificar la separabilidad y confusión entre las clases, se realizó un análisis de discriminante lineal (LDA) para cada mes. El LDA es una técnica que determina la combinación lineal de variables que mejor separa las clases al maximizar la relación entre las varianzas inter e intraclase, que se puede interpretar como un agrupamiento en reversa (Gotelli y Ellison, 2004). La técnica permite la predicción *a posteriori* de nuevas observaciones, lo que la convierte en una técnica tanto de análisis como de clasificación supervisada (Xanthopoulos *et al.,* 2013). Esta técnica asume una distribución normal de los patrones y discrimina bien si las diferencias se encuentran en los promedios de los valores. Esto hace que la prueba de separabilidad sea suficientemente exigente y robusta para asumir diferencias representativas entre las UO.

La fase de entrenamiento de los LDA se efectuó de forma mensual con 100 realizaciones aleatorias de la definición ambiental de cada UO. Estos conjuntos de valores fueron clasificados para su mes correspondiente y la clasificación obtenida se evaluó cuantitativamente con apoyo visual. Se obtuvieron matrices de confusión mensuales en las que se contrastaron los datos de entrenamiento contra lo predicho por el LDA. Se definió el 20% como el error máximo aceptable entre UO (Chuvieco, 1995). Aquellas con confusiones mayores fueron redefinidas o reagrupadas, ya que se asume que esto representa el grado de yuxtaposición entre las definiciones ambientales de las UO o bien áreas de transición.

Distribución espacial de las UO

Cada modelo LDA mensual obtenido se utilizó para clasificar el área de estudio y obtener la distribución espacial de las UO. Como parte del proceso de depuración, se consideró la coherencia espacial (en términos de vecindad y forma) de la definición ambiental. Debido a que se presentaron confusiones de clasificación entre pixeles de características biofísicas similares pero separados espacialmente (i.e. distintas UO), se adicionó un conjunto de reglas para considerar la ubicación como un criterio para asignar una UO. La contribución de las variables a la separabilidad de las UO se evaluó con gráficas de ordenación de los dos primeros componentes discriminantes. Finalmente, se obtuvieron las distancias euclidianas entre los centroides de las UO para representar su relación en dendogramas.

Validación

La confusión final entre la definición ambiental de las UO se evaluó con matrices de confusión mensuales (Chuvieco, 1995). Se generaron 100 nuevas realizaciones de la definición ambiental de cada UO, de forma similar a la realizada para la clasificación supervisada. Estas realizaciones se contrastaron contra las predicciones del modelo mensual de clasificación. Las doce matrices de confusión mensual se promediaron para obtener una matriz de confusión general.

Resultados

El resultado final de este trabajo fue la definición ambiental y la representación espacial mensual de 18 unidades oceanográficas (UO) climatológicas del Golfo de México y áreas adyacentes como el producto de la integración de datos biofísicos derivados de percepción remota y modelos numéricos.

Estructura de datos

Se obtuvieron 12 compuestos climatológicos mensuales para los parámetros: ADT (topografía dinámica del mar), CLO (concentración de clorofila a), CSU y CSV (componentes de los vectores de corrientes superficiales), CSMag (magnitud de la corriente superficial), FLH (altura de la línea de fluorescencia de la clorofila), SST (temperatura superficial del mar) y SAL (salinidad superficial).

Se generaron doce clasificaciones no supervisadas mensuales únicas. El número de grupos (*k*) fue determinado a partir de los valores del error dentro de cada clase, lo que permitió mantener la consistencia entre los meses, con el mínimo de error. De los meses de enero a agosto se utilizó una k=13, mientras que para septiembre, octubre y noviembre una k=15. Para diciembre se estableció una k=14 debido a que los meses de otoño presentan las condiciones más variables interanualmente, por lo que los parámetros promediados pierden la homogeneidad observada en el resto del año.

Para casi todos los meses, excepto de mayo a julio, se unieron las clases que dividían la zona central del GoM, pues éstas tenían una forma poco consistente entre meses. En las clasificaciones no supervisadas, la separación de la corriente del Lazo del GoM Norte se diluye a partir de agosto y hasta noviembre, por lo que esta UO se redefinió con base en sus parámetros ambientales.

Definición ambiental de unidades oceanográficas

Se obtuvo un esquema de definiciones ambientales de 14 unidades oceanográficas (UO) diferenciables por sus características biofísicas más cuatro UO separadas espacialmente (tabla 1) y con una secuencia consistente a lo largo del año de los parámetros que las definen por sus valores promedio y desviación estándar (Figuras 1-3). Mensualmente se observan entre 15 y 18 UO, ya que las UO *11.Surgencia de Yucatán, 15.Costa oeste* y *18.Surgencia de Tabasco*, se presentan estacionalmente entre mayo y agosto. El resto de las UO tienen representación a lo largo del año, con variaciones tanto en los parámetros biofísicos (Figuras 2-4) como en su extensión (Figuras 7).

En los dendogramas de los centros de clase, se observan dos grupos generales de unidades (Figura 5): las definidas por la circulación (UO 6, 7, 2, 8, 3, 1, 4, 5) y aquellas con rasgos costeros definidos por la NST y el InvCLO (UO 10, 11, 12, 9, 13, 14). Los gráficos de ordenación mensuales derivados de LDA presentaron resultados similares (Figura 6). De forma conjunta, todas las UO que pertenecen al sistema de circulación de la corriente del Lazo (UO 1 a 5) son las de mayor magnitud de la corriente superficial, particularmente la UO *4.Corriente del Golfo*, siendo la más intensa con dirección marcadamente hacia el norte (Figura 2). Al otro extremo se ubican las plataformas conformadas por las UO *12. Plataforma Continental sur*, incluyendo a sus UO derivadas (UO 16 y 17) y la UO *13.Plataforma Oeste de Florida* con corriente superficial más débil. El resto de las UO son de magnitud de corriente baja, cercanas a 0 m/s y con poca variación, a excepción de la *6.Corriente del Caribe* de magnitud de corriente superficial media.

Se distinguen también las UO de NST y SAL opuestas (Figura 3): por un lado la UO asociadas a las masas de agua del Caribe más salinas, en contraposición con las aguas frías del norte del GoM (UO 9, 10 y 14), además de la UO *11.Surgencia de Yucatán*, las cuales a su vez presentan altas concentraciones de CLO (representado como valores bajos del InvCLO, Figura 4).

La mayoría de los parámetros biofísicos (con excepción de las corrientes superficiales), presentan una oscilación estacional de sus valores en todas las UO (Figuras 3 y 4). Por ejemplo, las UO del norte del GoM que presentan variaciones térmicas anuales de hasta 15°C, como en la UO *10.Costa norte* donde se observan los valores de NST más bajos de noviembre a marzo, pero los más altos de la región en agosto. En contraste, se distinguen algunas UO cuya variabilidad es muy corta y mantienen valores altos de estos parámetros, particularmente las del Mar Caribe (UO 5, 6 y 7). Un patrón diferente se observa en la UO *14.NE Florida*, que muestra temperaturas bajas y la ADT mínima de la región a lo largo del año.

En la salinidad se distinguen UO de variabilidad muy alta, tanto anual como mensualmente (Figura 3c). Las UO del norte (9 y 10) tienen las salinidades más bajas de la región con variaciones de más de 4 UPS entre los meses de verano e invierno. De ellas resalta la UO 10, la cual refleja las amplias variaciones de salinidad que se esperan de la influencia del sistema de ríos de la costa de Estados Unidos. La UO *8.Golfo Central* oscila anualmente de forma similar a las anteriores, pero presenta un rango de variabilidad mensual menor pero de valores más altos que las anteriores. De

Tabla 1. Características principales que establecen las diferencias más evidentes entre las clases de las unidades oceanográficas. Además de las abreviaturas ya mencionadas anteriormente, se utilizan CL=Corriente del Lazo y CS=Corriente Superficial.

	Nombre	Características principales
1	Corriente de Lazo Sur	Sector de la CL con componente en U negativo (siendo el menor del GoM), y magnitud ligeramente más alta que su contraparte al Norte (CL Norte). La ADT y NST también son mayores que la CL Norte.
2	Corriente Lazo Norte	Representa el segmento de flujo hacia el SE (componente U de la CS más alto del GoM) de la CL de aguas cálidas y ADT alta.
3	Corriente de Florida	Flujo intenso marcadamente al Este (componente en U de la CS más alto y la segunda en magnitud) de NST cálida y parámetros biológicos bajos (CLO y FLH).
4	Corriente del Golfo	Se definen por tener la magnitud de corriente (particularmente en su componente en V) más alta del área de estudio. Del grupo de UO más cálidas.
5	Corriente de Yucatán	Ambientalmente similar a la UO 4 salvo por la NST que en este caso es más cálida.
6	Corriente Caribe	ADT y NST más altas del área de estudio y de muy baja variación intra anual. CS es de baja magnitud, particularmente con flujo promedio hacia el NNO e intrusión de agua con bajas concentraciones de los parámetros biológicos (CLO y FLH).
7	Atlántico	Similar a la UO 6 con NST ligeramente más baja al igual que sus concentraciones de los parámetros biológicos. CS de poca intensidad particularmente en el componente U.
8	Golfo Central	Esta clase representa la porción del GoM más variable donde todos los parámetros analizados se presentan en sus valores promedio regionales.
9	GoM Norte	Transición diferenciable entre la Costa Norte y el GoM central. Alta fluctuación de NST a lo largo del año, con concentraciones de CLO altas. Presenta las magnitudes de CS segundas más bajas.
10	Costa Norte	Presentan los valores más altos en los parámetros biológicos (CLO y FLH) y la menor SAL a lo largo del año. De octubre a abril tiene la menor NST, aunque está se eleva y se iguala con la mayor parte del GoM durante el verano.
11	Surgencia de Yucatán	UO bien separada durante el verano por las NST más frías y concentraciones elevadas de los parámetros biológicos (CLO y FLH).
12	Plataforma Continental sur	Es la UO más salina del área con concentraciones de CLO considerables.
13	Plataforma Oeste de Florida	Se separa de la UO 10.Golfo Norte por su salinidad marcadamente más alta, mayor concentración de clorofila y NST, particularmente durante el verano.
14	NE Florida	Agua localizada entre la UO4.Corriente del Golfo y la Costa NE de la Florida. Es diferenciable por CS mucho menor que las aledañas, con la ADT más baja del área de estudio y concentraciones de CLO importantes.
15	Surgencia de la Costa Oeste	UO ambientalmente similar a la UO 11, pero diferenciada por ubicación, ya que abarca una delgada franja costera en la costa oeste del GoM.
16	Plataforma Cubana	Ambientalmente similar a la UO12. Plataforma Continental sur, separada por su ubicación, y no varía espacialmente a lo largo del año.
17	Bancos de las Bahamas	Ambientalmente similar a la UO12. Plataforma Continental sur, separada por su ubicación, y no varía espacialmente a lo largo del año.
18	Surgencia de Tabasco	Ambientalmente idéntica a la UO11. Surgencia de Yucatán, separada por su ubicación. Se presenta únicamente en julio y agosto.

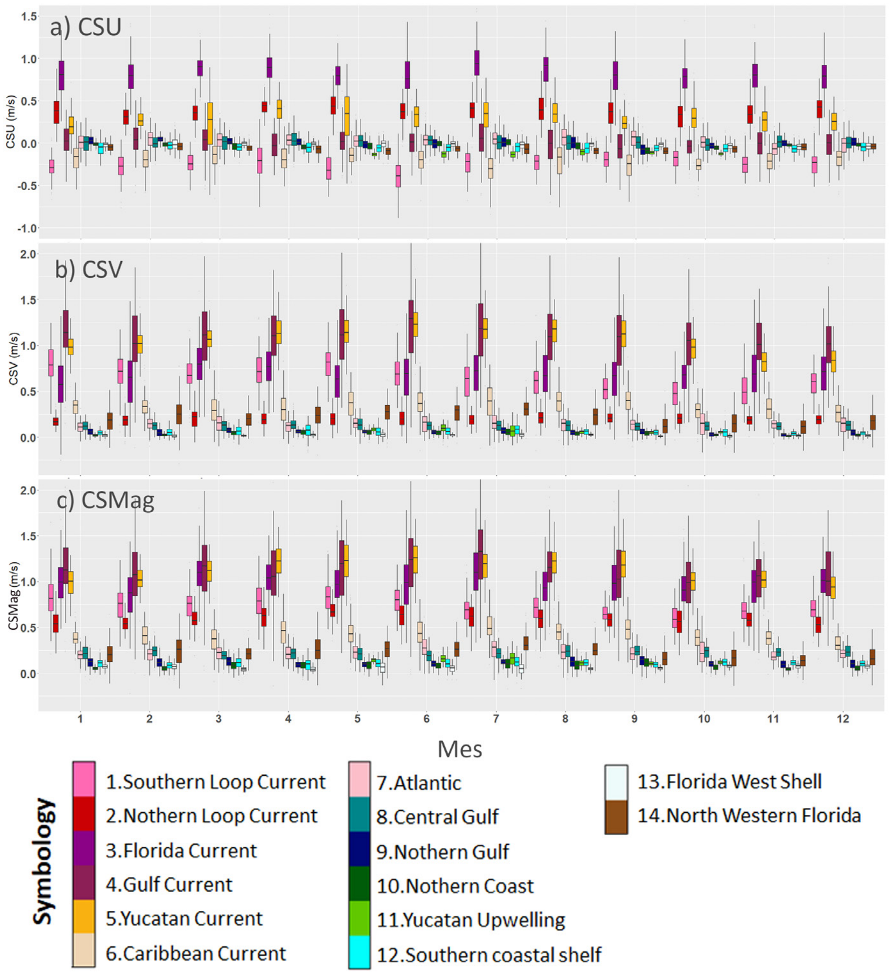

Figura 2. Gráficos de caja y bigote de los parámetros que definen la circulación: (a) CSU, (b) CSV y (c) CSMag, y que son obtenidos de la definición ambiental mensual de las unidades oceanográficas (promedio y desviación estándar de los parámetros) y que muestran la relación que guardan las unidades.

manera asíncrona, la UO *13.Plataforma Oeste de Florida* presenta disminución de salinidad de julio a octubre y un aumento considerable en abril y mayo. A lo largo del año, la UO *12. Plataforma Continental sur* y las UO derivadas de esta (16 y 17), tienen la salinidad más alta, excepto de agosto a octubre cuando ésta disminuye ligeramente (Figura 3).

En los parámetros biológicos se observan dos conjuntos de UO que evolucionan de forma disímil a lo largo del año (Figura 4). Por un lado, están las UO que mantienen consistentemente altas concentraciones de CLO y FLH, de las que resalta la UO *10. Costa Norte*, seguida de la UO *11.Surgencia de Yucatán* y como consecuencia las UO derivas: *15.Costa Oeste* con presencia de mayo a octubre y *18.Surgencia de Tabasco*, con presencia en julio y agosto. En el otro extremo están las UO del Mar Caribe con muy bajas concentraciones de los parámetros biológicos, excepto la UO *5.Corriente de Yucatán*, que presenta un aumento significativo entre julio y octubre.

De forma general, la circulación superficial de la región presenta componentes en U y en V (CSU y CSV) positivos, a excepción de las unidades *6.Corriente Caribe* y *7.Atlántico* con un componente de circulación hacia el oeste (CSU negativo). Con circulación hacia el este, están la UO *3.Corriente de Florida*, seguida de las UO *2.Corriente del Lazo Norte* y *5.Corriente de Yucatán*; aunque ésta última es la segunda más intensa en CSV y la segunda en la magnitud de la corriente (CSMag) (Figura 2).

Distribución y variación espacial de las UO

Se generaron doce mapas de unidades oceanográficas del Golfo de México utilizando predicciones espaciales a partir de la

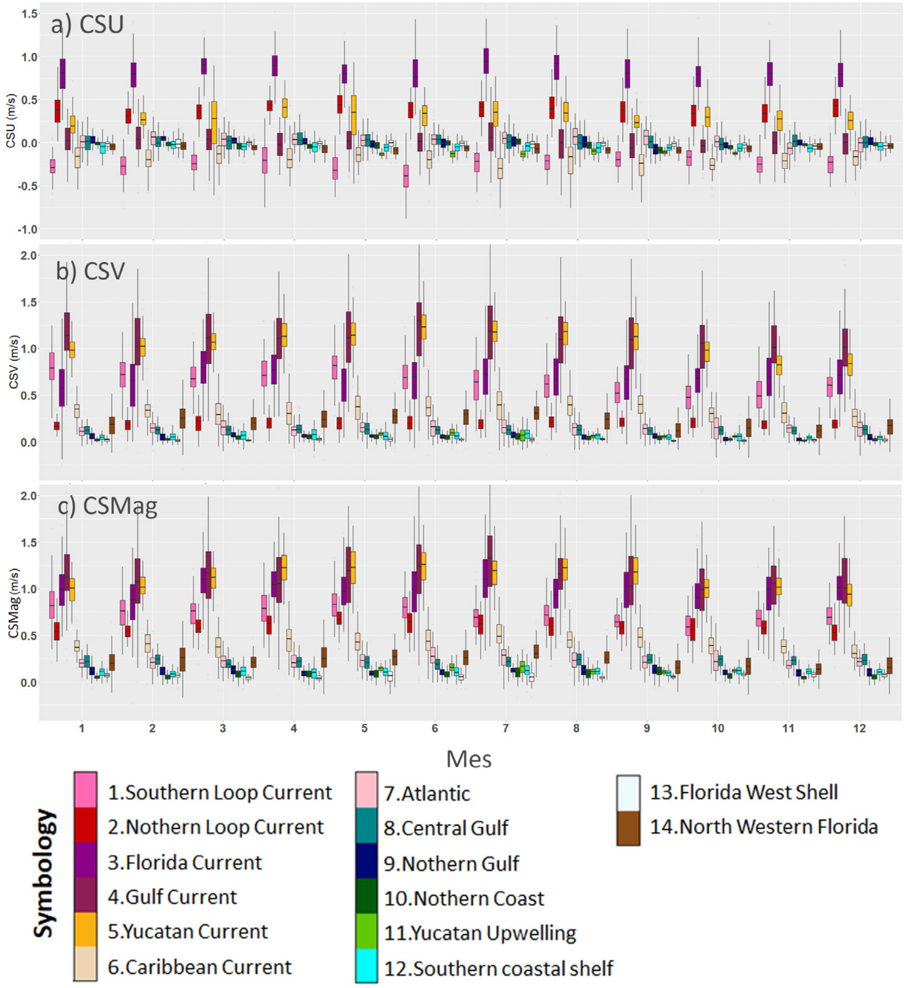

Figura 3. Gráficos de caja y bigote de los parámetros indicadores de la condición térmica y de densidad: (a) ADT, (b) NST y (c) SAL, que muestran la evolución temporal y la relación que guardan entre las unidades. Los valores que se grafican fueron obtenidos de la definición ambiental mensual de las unidades oceanográficas (promedio y desviación estándar de los parámetros).

definición ambiental (Figura 7). Aquí se observa la corriente del Lazo bien definida en dos secciones: *1.Corriente del Lazo Sur* y *2.Corriente del Lazo Norte* que se conectan de forma continua. Sin embargo, de agosto a noviembre, esta continuidad entre ambas UO se corrompe hasta diciembre, cuando vuelve a representar un flujo continuo.

En el sentido del flujo principal, está la UO *3.Corriente de Florida*, presente en el estrecho de Florida, que a pesar de tener bien definidas magnitud y dirección de forma constante, su forma varia ligeramente a lo largo del año. Hacia el norte se encuentra la UO *4.Corriente del Golfo* bien delineada de forma casi constante. En el otro extremo se ubica una porción del flujo de circulación principal denominado como UO *5.Corriente de Yucatán*, que de octubre a febrero inicia al borde sur de la isla de Cozumel internándose de forma vertical hacia el interior del GoM. El resto del año, se mezcla con la unidad *6.Corriente del Caribe*, que ocupa la mitad de la porción del mar Caribe, con una división inclinada hacia el oeste. La contra parte del mar Caribe es la UO *7.Atlántico*, la cual se interna por el centro de la Corriente del Lazo y ocupa la zona noreste del área de estudio de forma constante.

El centro del Golfo de México forma una única unidad oceanográfica (*8.Golfo Central*) delimitada al este por la Corriente del Lazo. Ésta cambia de forma en respuesta a las modificaciones de las UO aledañas, particularmente de la UO *9.GoM Norte*, que tiene variaciones de tamaño que se presentan de forma no estacional; por un lado, esto se debe a la disminución de la NST, y alcanza su mayor extensión en marzo, cuando cubre una

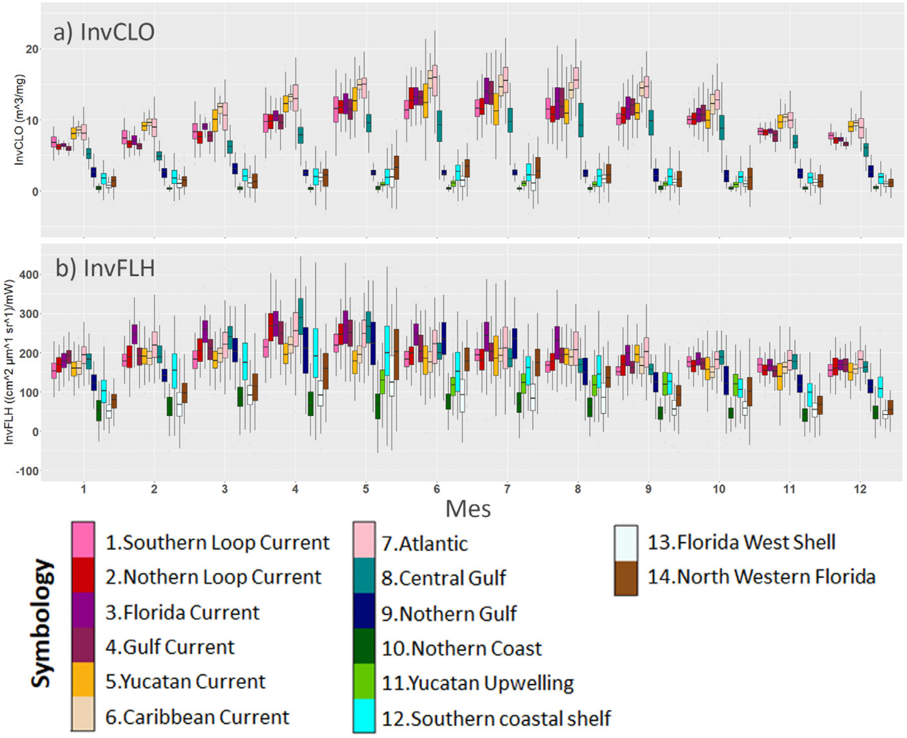

Figura 4. Gráficos de caja y bigote de los parámetros que se incorporaron como indicadores biológicos, ambos representados como su inverso matemático: (a) InvCLO y (b) InvFLH. Las gráficas muestran la evolución temporal de los parámetros y la relación que guardan entre las unidades. Los valores que se grafican fueron obtenidos de la definición ambiental mensual de las unidades oceanográficas (promedio y desviación estándar de dichos parámetros).

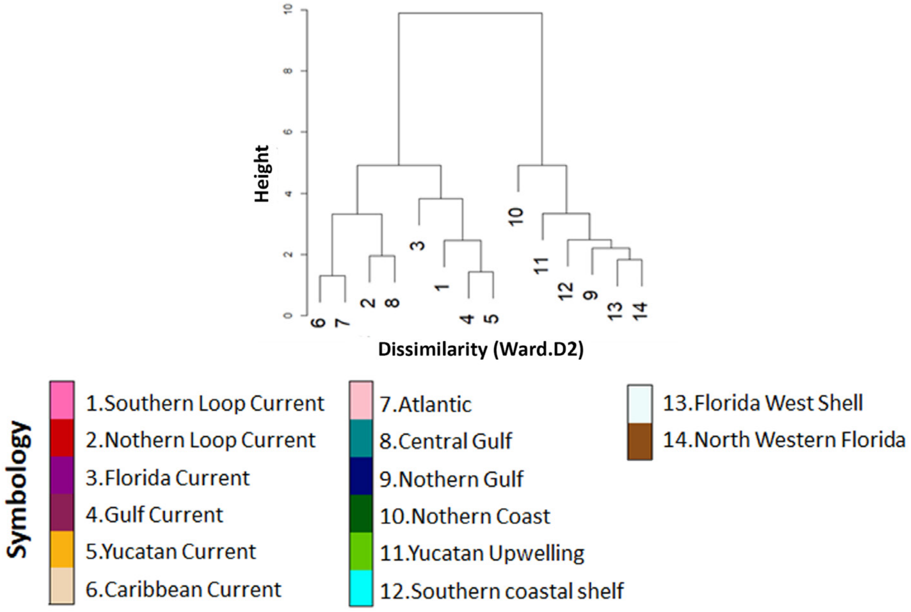

Figura 5. Dendograma de disimilitud que muestra la asociación que existe entre los centroides de las unidades oceanográficas donde se observan dos grupos fundamentales de UO.

vasta porción del norte del GoM. Por otro lado, esta unidad también se expande en agosto, debido a la intrusión de aguas con valores de CLO altos en una porción al norte de la Corriente del Lazo.

La costa norte del Golfo de México está ocupada por la UO *10.Costa Norte*, que desde noviembre hasta marzo, se extiende desde Texas hasta la Bahía de Tampa. De abril a agosto disminuye su extensión paulatinamente, hasta concentrarse entre las Bahías Galveston y Mobile. Complementariamente, la UO 9.*GoM Norte* se expande de septiembre a diciembre. Aledañas a la UO 9 y 10 hacia el sur, se ubica la UO *13. Plataforma Oeste de Florida*, que presenta variaciones estacionales de tamaño particularmente hacia el norte, ya que, hacia el sur, tiene como límite la corriente de Florida. Su menor expresión sucede durante febrero y la mayor en julio, abarcando una buena porción de la plataforma de Florida.

Con excepción de la UO 13, el resto de las plataformas continentales del área de estudio se aglomeraron en la definición ambiental como la UO *12.Plataforma Continental sur* debido a la interrelación que existe en sus parámetros biofísicos, por lo que fueron separadas por su ubicación. De aquí se derivan la UO *16.Plataforma Cubana* que incluye el Golfo de Guantánamo y el interior del archipiélago de los Jardines de la Reyna y la UO *17.Bancos de las Bahamas*, que incluye los bancos asociados a estas islas. De este grupo de UO, la UO *12.Plataforma Continental sur* es la única que presenta modificaciones geográficas debido a que ahí la NST e InvCLO varían estacionalmente y presenta una deformación hacia la Bahía de Campeche a partir de junio y con las últimas reminiscencias presentes en noviembre.

La alteración más importantes a la forma de la UO12 es la aparición de la UO *11.Surgencia de Yucatán* que se presenta desde abril y hasta septiembre cuando se disipa. La UO 11 aparece en Cabo Catoche con un incremento de la CLO y una disminución de la NST, características fundamentales de esta surgencia. Ésta presenta una evolución de este a oeste, cubriendo paulatinamente el resto de la plataforma norte de la Península de Yucatán. Esta UO 11 exhibe dos áreas de características ambientales similares en el interior del GoM que son diferenciadas por su ubicación. Un área frente a las costas de Tabasco que se presenta en julio y agosto, llamada *Surgencia de Tabasco (UO18)*. La otra ocurre entre mayo y agosto a lo largo de la costa oeste del GoM, desde Laguna Madre en Tamaulipas hasta en Boca del Río, que fue denominada *15.Surgencia de la Costa Oeste*.

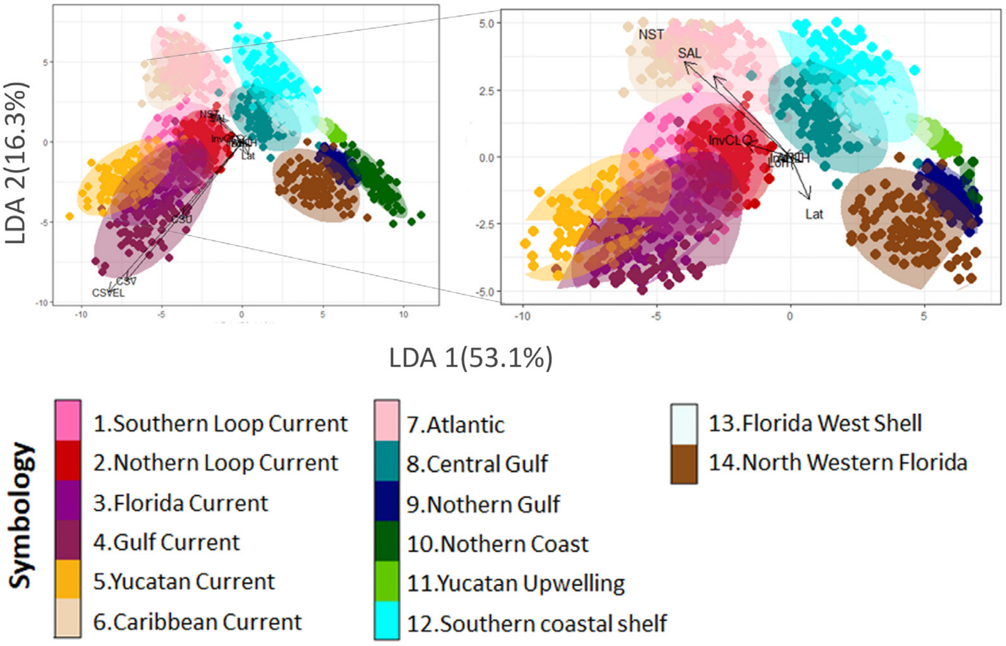

Figura 6. Gráficos de ordenación de los dos primeros discriminantes obtenidos con el análisis de discriminante lineal para el mes de mayo, donde se representa graficamente tres dimenciones de la asociación que existe entre UO y los parametros biofisicos a partir de la definición ambiental de las UO. En (a) se muestra el diagrama completo y en (b) un acercamiento al centro del grafico para apreciar los vectores más cortos de los parámetros.

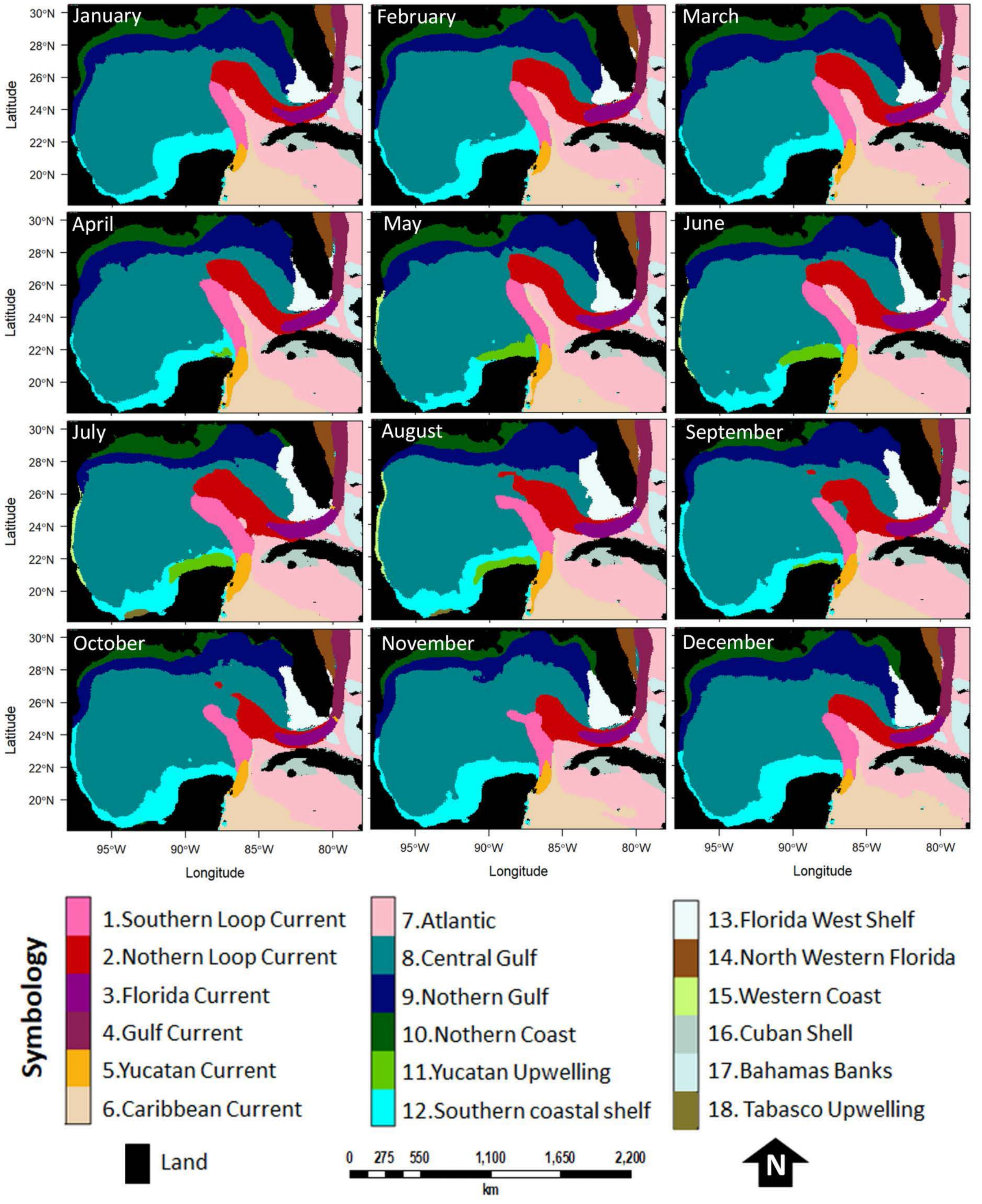

Figura 7. Representación espacial y distribución de las unidades oceanográficas a lo largo del año generada a partir de su definición ambiental.

Finalmente, la UO *14.NE de Florida*, se refiere a una porción de mar ubicada entre la Corriente del Golfo y la costa este de Florida, debido a que presenta una corriente superficial débil y NST mucho menores que el resto de la zona. No presenta variaciones de forma considerables a lo largo del año.

Validación

Se generó una matriz de confusión general que promedia las matrices de confusión mensuales, donde se excluyen las UO 15 a 18 que son separadas por ubicación y no por sus valores ambientales (Tabla 2). La exactitud promedio por UO es superior al 89% (D. E.= 7.83%). Las confusiones principales ocurren entre la *9.GoM Norte* y la *10.Costa Norte*, particularmente entre mayo y octubre debido a la homologación de la NST y a incrementos en las CLO y FLH; entre las UO *6.Corriente Caribe* y *la 7.Atlántico* y *entre 12. Plataforma Continental sur* y *13.Plataforma de Florida*, por ser consistentemente unidades similares en todos los meses. Existen confusiones menores entre las UO1 y UO4, entre las UO2 con UO3 particularmente por la similitud que presentan en los parámetros de la circulación superficial.

Discusión

En este trabajo se diferenciaron para Golfo de México (GoM) conglomerados de características superficiales homogéneas, equiparables a lo largo del año denominados unidades oceanográficas.

Existen varios esfuerzos de regionalización del GoM especialmente enfocados en aspectos particulares, ya sea en la parte biológica (Salmerón-García *et al.,* 2010), delimitación de hábitats (Yáñez-Arancibia y Day, 2004), por procesos físicos (Zavala-Hidalgo y Fernández-Eguiarte, 2006 y Miron *et al.,* 2017) o bien por la respuesta espectral en imágenes satelitales (Callejas-Jiménez *et al.,* 2012). Estos trabajos tienen coincidencias espaciales y de interpretación, pero ninguno había expresado la dinámica anual integrando las distintas propiedades oceanográficas de este ecosistema.

En este trabajo realizamos análisis estadísticos multivariados para proponer una agrupación robusta de datos de diferente índole que permitieran obtener una interpretación directa de la integración de variables. De esta manera, describimos la evolución temporal de las unidades oceanográficas superficiales (UO) en un año promedio, establecimos el comportamiento intra anual de los parámetros biofísicos que las definen y se presentan las variaciones espaciales de estas UO. El resultado fue la definición mensual ambiental y la representación espacial de 18 unidades oceanográficas en las que se observan los rasgos característicos del GoM, particularmente, los que se presentan periódicamente. Se distinguieron dos agrupaciones generales: las clases asociadas al flujo predominante de la región, en contraposición con las aledañas a este flujo, en las que predominan valores altos de los parámetros biológicos en costas y plataformas y diferencias importantes del régimen térmico.

Algunas de las regiones asociadas a la circulación reconocidas en este estudio fueron planteadas previamente por Zavala-Hidalgo y Fernández-Eguiarte (2006). Por ejemplo, estos autores dividen el Banco de Campeche en dos secciones al separar la zona con aportes de los ríos Grijalva y Usumacinta del resto de la plataforma, con fronteras son similares a las propuestas para la UO *12.Plataforma Continental sur*. Sin embargo, los autores separan el giro ciclónico que se presenta en la Bahía de Campeche (Monreal-Gómez y Salas-de León, 1990), que con nuestra regionalización no pudimos diferenciar, potencialmente debido a la relativamente débil circulación superficial de la zona en comparación con el resto del GoM, y a la variabilidad temporal con la que se presenta (Vázquez de la Cerda *et al.,* 2005; Pérez-Brunius *et al*. 2013).

Por ejemplo, en los límites de la sección que divide el Mar Caribe donde se separa la corriente del Caribe, de la zona de giros y remolinos al sur de Cuba. Por otro lado, en el caso del flujo de circulación hacia el norte, ellos lo plasman como una sola región, mientras aquí la dividimos en 6 segmentos de acuerdo con la magnitud y dirección de la corriente superficial, diferenciando incluso, el agua del Atlántico que las rodea.

Zavala-Hidalgo y Fernández-Eguiarte (2006) y Miron *et al.* (2017), ambos a partir factores de circulación, dividen la porción Lousiana-Texas de la sección Mobile-Alabama-Florida en la desembocadura del río Misisipi. En contraposición, hay quienes debido a factores bióticos consideran como una sola región a la porción entre las Bahías de Galveston y Mobile (Yáñez-Arancibia y Day, 2004; Salmerón-García *et al.,* 2010; Callejas-Jiménez, 2012). Nosotros, proponemos la división del norte del GoM en dos UO separadas longitudinalmente, una más costera que su contraparte, debido a que en general, la intensidad de la corriente es menor y en promedio más homogénea que

Tabla 2. Matriz de confusión promedio entre la definición de las unidades oceanográficas expresada en porcentajes. Se remarcan en escala de grises la intensidad de la confusión entre clases mayores al 1%.

	Referencia													
Predicción	1	2	3	4	5	6	7	8	9	10	11	12	13	14
1. Corriente de Lazo Sur	98 (+-1.6)	0.42	0.00	2.58	1.00	0.08	0.00	0.00	0.00	0.00	0.00	0.00	0.00	0.00
2. Corriente Lazo Norte	0.50	98.75 (+-1.96)	2.42	1.58	0.00	0.00	0.58	0.50	0.00	0.00	0.00	0.00	0.00	0.00
3. Corriente de Florida	0.00	0.17	96.25 (+-1.91)	0.50	0.58	0.00	0.00	0.00	0.00	0.00	0.00	0.00	0.00	0.00
4. Corriente del Golfo	0.25	0.00	0.17	94.67 (+-2.5)	0.00	0.00	0.00	0.00	0.00	0.00	0.00	0.00	0.00	0.00
5. Yucatán	0.75	0.00	1.17	0.17	98.42 (+-2.57)	0.00	0.00	0.00	0.00	0.00	0.00	0.00	0.00	0.00
6. Corriente Caribe	0.42	0.00	0.00	0.00	0.00	97.08 (+-2.07)	7.75	0.08	0.00	0.00	0.00	0.00	0.00	0.00
7. Atlántico	0.00	0.25	0.00	0.42	0.00	2.83	91.5 (+-4.3)	0.08	0.00	0.00	0.00	0.08	0.00	0.00
8. Golfo Central	0.08	0.42	0.00	0.00	0.00	0.00	0.08	96.67 (+-1.87)	0.08	0.00	0.00	2.92	0.00	0.00
9. GoM Norte	0.00	0.00	0.00	0.00	0.00	0.00	0.00	0.67	95.83 (+-3.01)	7.83	0.00	0.33	0.08	0.00
10. Costa Norte	0.00	0.00	0.00	0.00	0.00	0.00	0.00	0.00	0.33	90.83 (+-3.21)	0.00	0.00	0.00	0.00
11. Surgencia de Yucatán	0.00	0.00	0.00	0.00	0.00	0.00	0.00	0.00	0.00	0.00	100 (+-0)	0.33	0.00	0.00
12. Plataforma continental Sur	0.00	0.00	0.00	0.00	0.00	0.00	0.08	2.00	0.00	0.00	0.00	89.33 (+-4.58)	0.00	0.00
13. Plataforma de Florida	0.00	0.00	0.00	0.00	0.00	0.00	0.00	0.00	1.67	0.75	0.00	6.92	99.83 (+-0.39)	2.00
14. NE Florida	0.00	0.00	0.00	0.08	0.00	0.00	0.00	0.00	2.08	0.58	0.00	0.08	0.08	98 (+-2.04)

en resto del GoM, por lo que su separación responde a las concentraciones de clorofila *a* y a las condiciones térmicas.

En el siguiente grupo de UO, se divide claramente la zona norte con rangos térmicos amplios, algunas de ellas diferenciadas por una alta actividad biológica (Yáñez-Arancibia y Day, 2004; Salmerón-García, *et al.,* 2010, Muller-Karger *et al.,* 2015) mientras que por otro lado están las UO oligotróficas y de temperaturas estables como las del Mar Caribe y agua característica del Atlántico (Aguirre-Gómez, 2014).

La región del norte es presentada como una combinación de varias zonas tanto en el trabajo de Salmerón-García *et al.,* 2010, como en el de Callejas-Jiménez *et al.,* 2012, aunque considerablemente distintas entre sí, mientras que en nuestros resultados se expresan como dos unidades oceanográficas que evolucionan espacialmente a lo largo del año y que muestran variaciones estacionales de sus parámetros ambientales. Por ejemplo, los primeros autores describen la pluma del Misisipi como una región con presencia en verano, mientras que nosotros observamos el cubrimiento de esa área como una expansión de la UO9 entre julio y septiembre, presumiblemente por un enriquecimiento de aguas debido al flujo sureste de la pluma de dicho sistema rivereño (Müller-Karger *et al*., 1991). El transporte de altas concentraciones de clorofila por el sistema del Misisipi hacia el interior del golfo ocurre por la interacción de giros y meandros con la topografía, contribuyendo al enriquecimiento de la zona profunda (Martínez-López y Zavala-Hidalgo, 2009).

Consideramos que la integración de datos físicos y biológicos disminuye el efecto de las fuertes diferencias en la respuesta óptica de esta zona, como se presenta en Callejas-Jiménez *et al.,* 2012. Aunque, por otro lado, destaca que estos autores no hacen una diferencia entre la zona de transición de la zona norte del sur en la temporada de huracanes que nosotros pudimos distinguir debido a la inclusión de otros parámetros como la NST.

En la región llamada Corriente del Lazo en el trabajo de Callejas-Jiménez *et al.* (2012), fue diferenciada por nosotros como una porción homogénea del agua del Atlántico (UO7) de temperatura estable y circulación diferenciada del flujo de la Corriente del Lazo. En su trabajo, Callejas-Jiménez *et al.* (2012) integran en la región oligotrófica del Golfo de México lo que aquí diferenciamos como las Corrientes del Caribe, Yucatán, Lazo y Florida. En ese sentido, Salmerón-García *et al.* (2010) con base en las anomalías de la clorofila *a,* mantuvieron esas UO de circulación diferenciada, como una sola región junto con el centro del GoM.

Callejas-Jiménez *et al.* (2012) utilizaron datos de color del mar, como un resumen de la información detectada con percepción remota, argumentando que la temperatura superficial del mar y la concentración de clorofila *a* no tienen gradientes lo suficientemente agudos para ser diferenciados con técnicas de clasificación. Sin embargo, con nuestro trabajo obtuvimos unidades oceanográficas diferenciables con estos, e incluso otros parámetros. Por ejemplo, estos autores delimitan un área que representa la surgencia de Yucatán, que va desde Cabo Catoche hasta Cayo Arenas para la temporada de junio a noviembre, a diferencia con lo que planteamos aquí, donde se puede diferenciar espacialmente la surgencia (UO *11.Surgencia de Yucatán*) desde los primeros esbozos detectados en mayo, hasta su máxima expresión en agosto. En Callejas-Jiménez *et al.* (2012) se enmascaró la evolución espaciotemporal de la surgencia, probablemente como efecto del agrupamiento estacional donde se presentan una región menor en la estación de secas, mientras que nosotros observamos que desaparece totalmente a partir de octubre.

Por otro lado, observamos la aparición de un área alargada entre Tamaulipas y Veracruz asociada ambientalmente a la UO 11 que se presenta de mayo a agosto, y que denominamos UO *15.Surgencia de la Costa Oeste*, mientras que Callejas-Jiménez *et al.,*(2012) muestran esta región bien delimitada durante todo el año. De manera similar existe una pequeña área que se presenta durante julio y agosto frente a la costa de Tabasco, de propiedades físicas y biológicas similares a la surgencia de Yucatán. Estas zona se alimenta de aguas frías provenientes de la descarga del afluente del sistema Grijalva-Usumacinta, que enriquecen las aguas y provoca florecimientos algales que pueden acarrearse hacia el interior del golfo (Aldeco *et al*., 2009; Zavala-Hidalgo *et al*., 2006; Martínez-López y Zavala-Hidalgo, 2009).

Si se considera la extensión que presentan Salmerón-García *et al.* (2010) con respecto de la extensión de la UO *12.Plataforma Continental sur* de junio a octubre, se observan similitudes considerables. Esta área se caracteriza por la confluencia de las corrientes costeras provenientes del norte con las originadas en el interior de la plataforma de Campeche por lo que, durante el verano y otoño, las descargas del río Usumacinta se mueven hacia el interior del GoM (Zavala-Hidalgo *et al.,* 2006). Es por lo que, coincidiendo con Salmerón-García *et al.* (2010), proponemos una extensión de la región del *Plataforma Continental sur* que se relaciona con la influencia de elementos terrígenos, en contraposición con lo propuesto por Zavala-Hidalgo y Fernández-Eguiarte (2006) y Miron *et al* (2017) relacionados con la circulación.

La unidad que llamamos *Plataforma Oeste de Florida* ha sido reconocida como una entidad diferenciable en varios trabajos, ya sea por su contenido biológico (Salmerón-García *et al.,* 2010; Callejas-Jiménez, *et al.,* 2012), por su relevancia ecológica (Yáñez-Arancibia y Day, 2004) o por la particularidad de la circulación (Miron, *et al.,* 2017). Esta UO presenta una circulación muy débil que es una barrera de transporte, y que aísla los aportes de ríos y lagunas de Florida (Olascoaga, 2010) y, de forma similar que en Salmerón-García *et al.* (2010), tiene características similares con la del *Plataforma Continental sur*, especialmente durante el verano.

La parte central del GoM quedó definida como una sola UO con valores promedio regionales para todos los parámetros, a pesar de que se conoce una gran variedad de procesos oceanográficos que ahí ocurren. Estos procesos no estacionales y de periodicidad poco definida (Muller-Karger *et al.,* 2015), provocan que los promedios climatológicos enmascaren la firma tanto de la circulación como de la temperatura, necesarias para ser disgregados, por lo que en la mayoría de los trabajos de regionalización ocurre el mismo efecto.

El presente trabajo muestra una forma de evaluar el complejo sistema del GoM, a partir de un análisis integrador de datos de diferente índole, obtenidos de manera remota, estandarizada y bien documentada. Las unidades oceanográficas definidas condensan atributos importantes que hacen particular a cada sección y de manera única, se presenta su evolución espacial a lo largo del año.

Si bien, las observaciones de temperatura hechas mediante satélites representan una pequeña fracción de la superficie conocida como la piel del océano (Aguirre-Gómez, 2001), considerar variables derivadas del color del mar (CLO y FLH) y de altímetros (ADT) permiten incorporar a la concepción de UO información indirecta de la columna de agua. Las variables obtenidas del color del mar envuelven información de la capa eufótica que, aunque puede variar de acuerdo a las condiciones oceanográficas, estos datos son comúnmente utilizados como un proxy de las dinámica trófica de las aguas superficiales (Muller-Karger *et al*.,2015, Pardo *et al*., 2015, Briscoe *et al*., 2018). Establecer asociaciones de la productividad oceánica a partir de mediciones superficiales ha resultado fuertemente debatible, pues existen diferencias regionales en la forma de la distribución vertical de la clorofila y por lo tanto del fitoplancton. Esta producción está potencialmente relacionada con la profundidad de la capa de mezcla y la estratificación de la columna de agua, variables que no se han resuelto de manera contundente utilizando únicamente imágenes satelitales (Pasqueron de Fommervault *et al*. 2017). Para el golfo se estima que la profundidad del máximo de clorofila varía ampliamente (>35 m y hasta 100 m) entre diferentes regiones y en diferentes épocas del año (Hidalgo-Gonzales y Alvarez-Borrego, 2008; Pasqueron de Fommervault *et al*. 2017) lo que hace difícil asumir de manera contundente una representatividad de las condiciones más profundas.

Por otro lado, la NST y la ADT en conjunto proveen un panorama de la estructura térmica de la columna de agua, ya que los procesos que afectan el balance termodinámico modifican su volumen y por lo tanto la altura de la topografía dinámica absoluta (Pardo *et al*., 2015). Particularmente la ADT tiene información embebida de la estructura acumulada de toda la columna de agua que, con los datos complementarios de temperatura y los componentes de la circulación, proveen un panorama integrado de las condiciones oceánicas, al menos en la capa superior (Welsh e Inoue, 2000). En ese sentido diversos estudios muestran que la circulación característica superficial del golfo puede observarse en los primeros 800 m – 1000 m, con variaciones dependiendo de la influencia que imprimen las estructuras de mesoescala y los forzantes preponderantes de la circulación (DeHaan y Sturges, 2005) mientras que la circulación profunda sigue patrones muy poco variables hacia la zona más profunda y poco correlacionados con los patrones superficiales (Hamilton, 2009; Pérez-Brunius *et al*. 2017).

Sale de los alcances de este trabajo asumir o desentrañar la representatividad de las condiciones oceanográficas superficiales con respecto a toda la columna de agua. Sin embargo, como lo plantean Zacharias y Roff (2000) proponemos reconciliar los componentes de los ecosistemas que son medibles, que proveen información sinóptica, y que pueden servir de proxys para la identificación de regiones de características similares. Estas observaciones continuas permitirán además el monitoreo sistemático de tales regiones y de sus hábitats subyacentes.

La regionalización de los mares considerando la variabilidad temporal y espacial de las condiciones oceánicas es estratégico para el ordenamiento, manejo y conservación de los recursos y capital marino. Previamente se ha planteado la pertinencia de establecer esquemas de regionalización que permitan conocer cuál es la dinámica de los ecosistemas en términos de variabilidad estacional, anual, interanual e interdecadal para los mares mexicanos (Díaz de León *et al*. 2009) e inclusive como primicia para el monitoreo de grandes ecosistemas marinos (Longhurst, 2006). Proveer información de las variaciones inherentes de una región que se comporta de forma acoplada a lo largo del año permite a los tomadores de decisiones considerar esquemas flexibles o adaptables para el manejo de recursos asociados temporalmente a masas de agua (p. ej. Tiburón ballena, atunes, aves marinas migratorias, tortugas, etc.) o bien para la implementación de estrategias para contingencias ambientales como florecimientos algales nocivos (Soto *et al*., 2012) o derrames de hidrocarburos (Miron *et al*., 2017).

Estos resultados abren la posibilidad de analizar y monitorear la variabilidad interanual de las unidades y con ello aportar elementos cuantitativos de sus anomalías de mediano y largo plazo. Tener un esquema integrado de diferentes aspectos biológicos y físicos permitirá un monitoreo determinista que disminuya los efectos de la interpretación cualitativa de las variaciones de unidades oceanográficas, entendiendo como unidad a una entidad indivisible a partir de un conjunto de características dado. Por otro lado, reconocemos la necesidad de analizar a mayor escala espacial y temporal algunas unidades para definir y posteriormente monitorear otras estructuras de mesoescala conocidas como los giros desprendidos de la Corriente del Lazo o el giro ciclónico veracruzano.

Consideramos que esta investigación aporta información relevante en la caracterización espacio temporal de entidades relacionadas tanto con aspectos físicos como biológicos superficiales similares y que plantea bases sustentadas para el monitoreo integral de las aguas superficiales del Golfo de México.

Agradecimientos

Al Posgrado en Geografía de la UNAM por la oportunidad y facilidades prestadas para desarrollar esta investigación. A Olivia Salmerón-García por sus valiosos comentarios. Funding for the development of HYCOM has been provided by the National Ocean Partnership Program and the Office of Naval Research. Data assimilative products using HYCOM are funded by the U.S. Navy. Computer time was made available by the DoD High Performance Computing Modernization Program. The output is publicly available at http://hycom.org.

Bibliografía

Aldeco J., Monreal-Gómez M. A., Signoret M., León D. A. S., Hernández-becerril D. U., 2009, Occurrence of a subsurface anticyclonic eddy, fronts, and Trichodesmium *spp* . over the Campeche Canyon region, Gulf of Mexico. *Ciencias Marinas*, 35,4, 333–344.

Aguirre-Gómez, R. 2001. *Los mares mexicanos a través de la percepción remota.* Instituto de Geografía*.* Universidad Nacional Autónoma de México y Plaza y Valdés. México, D.F. 94 pp.

Aguirre-Gómez R., 2014, Spectral Reflectance Analysis of the Caribbean Sea. *Geofis. Int*., 534, 385–398. http://doi.org/10.1016/S0016-71691470073-X

AVISO, 2016, Ssalto/duacs multimission altimeter products. Disponible en: http://www.aviso.altimetry.fr/en/data/product-information Consultado mayo de 2016.

Briscoe D. K., Fossette S., Scales K. L., Hazen E. L., Mchuron E. A., Bograd S. J., Maxwell S. M., Lewison R. L., Robinson P. W., Kuhn C., Costa D. P., Crowder L. B., 2018. Characterizing habitat suitability for a central place forager in a dynamic marine environment. *Ecology and Evolution*, 2788–2801. https://doi.org/10.1002/ece3.3827.

Callejas-Jimenez M., Santamaria-del-Angel E., Gonzalez-Silvera A., Millan-Nuñez R., Cajal-Medrano R., 2012, Dynamic Regionalization of the Gulf of Mexico based on normalized radiances nLw derived from MODIS-Aqua. *Cont. Shelf. Res.*, 37, 8–14. http://doi.org/10.1016/j.csr.2012.01.014.

Cerdeira-Estrada S., López-Saldaña G., 2011, Nuevo Sistema Satelital de Monitoreo Oceánico para México. *Cienc. Mar*., 372, 237-247. https://doi.org/10.1016/j.jenvman.2013.01.036.

CONABIO, 2014, Promedios mensuales de temperatura superficial del mar, concentración de clorofila a y fluoresencia de la clorofila de enero de 2003 a diciembre de 2013, Ciudad de México.

Chuvieco, E., 1995, *Fundamentos de teledetección espacial*. 2ª Edición. Madrid, España. Ediciones RIALP. 451 pp.

Córdova A., Rosete-Vergés F., Enriquez G., Hernandez B., 2009, *Ordenamiento Ecológico Marino. Visión integrada de la regionalización*. Secretaria de medio ambiente y recursos naturales (SEMARNAT). Distrito Federal, México. 232 pp.

De la Lanza-Espino G., 2004, Gran escenario de la zona costera y oceánica de México. *Ciencias*, 076, octubre-diciembre, 4-13.

DeHaan C. J., Sturges W., 2005, Deep cyclonic circulation in the Gulf of Mexico. *J. Phys. Oceanogr*., 35, 1801–1812, https:// doi.org/10.1175/JPO2790.1.

Díaz de León A., Álvarez Torres P., Iglesias Barron O., 2009, Experiencias globales de clasificación y ejercicios de zonificación marina. En: *Ordenamiento ecológico marino, Visión integrada de la regionalización*. Córdova, *et al*. comps. Secretaria de medio ambiente y recursos naturales (SEMARNAT). Distrito Federal, México. 232 pp.

Esaias E.W., Iverson R.L., Turpie K., 2000, Ocean provinces classification using ocean color data: observing biological signatures of variations in physical dynamics. *Global Change Biol*., 6, 39-55.

Everitt B., Hothorn T., 2016, *A Handbook of Statistical Analyses Using* R. Disponible en: https://cran.rproject.org/web/packages/HSAUR/vignettes/Ch_cluster_analysis.pdf, consultado en diciembre de 2016.

Fiechter J., Mooers C. N. K., 2007,Primary production associated with the Florida Current along the East Florida Shelf: Weekly to seasonal variability from mesoscale-resolution biophysical simulations. *Journal of Geophysical Research*,. 112,12002, https://doi:10.1029/2006JC003576, 2007.

Gotelli N. J., Ellison A.M., 2004, *A primer of ecological statistics*. Sinauer Associates Inc. USA. 510 pp.

Halliwell G.R., 2004, Evaluation of vertical coordinate and vertical mixing algorithms in the HYbrid-Coordinate Ocean Model (HYCOM). *Ocean Modelling,* 7, 3–4, 285–322, https://doi.org/10.1016/j.ocemod.2003.10.002.

Hamilton P., 2009, Topographic Rossby waves in the Gulf of Mexico. *Progress in Oceanography*, 82,1, 1–31. https://doi.org/10.1016/j.pocean.2009.04.019.

Heileman S., Rabalais N., 2009, XV-50 *Gulf of Mexico: LME #* 5, Disponible en: http://lme.edc.uri.edu/images/Content/LME_Briefs/lme_5.pdf, Consultado en mayo de 2016.

Hidalgo-González R. M., Álvarez-Borrego S., 2008. Water column structure and phytoplankton biomass profiles in the Gulf of Mexico. *Ciencias Marinas*, 34,2,, 197–212.

Hobday aJ., Young J.W., Moeseneder C., Dambacher J.M., 2011, Defining dynamic pelagic habitats in oceanic waters off eastern Australia. *Deep Sea Res. Pt II,* 585, 734–745, http://doi.org/10.1016/j.dsr2.2010.10.006.

HYCOM, 2017, HYCOM Overview. Disponible en https://hycom.org/hycom/overview, Consultado en mayo de 2017.

IOCCG, 2009, Partition of the Ocean into Ecological Provinces: Role of Ocean-Colour Radiometry. Dowell, M. and Platt, T. eds, *Reports of the Coordinating Group, No. 9, IOCCG*, Dartmouth, Canada International Ocean-Colour.

Jain A.K., 2010, Data clustering: 50 years beyond K-means. *Pattern Recognition Letters*, 31-8, 651-666, ISSN 0167-8655, https://doi.org/10.1016/j.patrec.2009.09.011.

Le Hénaff M., Kourafalou V. H., Morel Y., Srinivasan, A., 2012, Simulating the dynamics and intensification of cyclonic Loop Current Frontal Eddies in the Gulf of Mexico. *Journal of Geophysical Research: Oceans*, 117-2, 1–20. https://doi.org/10.1029/2011JC007279

Li J., Heap A.D., 2008, A Review of Spatial Interpolation Methods for Environmental Scientists. *Geoscience*. Canberra, Australia, 163 pp. ISBN: 978 1 921498 28 2.

Longhurst A., 2006, *Ecological geography of the sea*, 2nd edn. Elsev Sci Pub. New York. 560 pp.

Martínez-López B., Zavala-Hidalgo J., 2009. Seasonal and interannual variability of cross-shelf transports of chlorophyll in the Gulf of Mexico. *Journal of Marine Systems*, 77,1–2, 1–20. https://doi.org/http://dx.doi.org/10.1016/j.jmarsys.2008.10.002.

Miron P., Beron-Vera F.J., Olascoaga M.J., Sheinbaum J., Pérez-Brunius P., Froyland G., 2017, Lagrangian dynamical geography of the Gulf of Mexico. *Sci*.71. https://doi.org/10.1038/s41598-017-07177-w.

Monreal-Gómez M.A., Salas-de León D.A., 1990, Simulación de la circulación en la Bahía de Campeche. *Geofísica Internacional,* 29, 2.

Müller-Karger F.E., Smith J.P., Werner S., Chen R., Roffer M., Liu Y., Muhling B., Lindo-Atichati D., Lamkin J., Cerdeira-Estrada S., Enfield D.B., 2015, Natural variability of surface oceanographic conditions in the offshore Gulf of Mexico. *Prog. Oceanogr,* 134, 54–76, https://doi.org/10.1016/j.pocean.2014.12.007.

Müller-Karger F.E., Walsh J.J., Evans R.H., Meyers M.B., 1991, On the seasonal phytoplankton concentration and sea surface temperature cycles of the Gulf of Mexico as determined by satellites. *J. Geohys. Res-Oc,* 96,C7, 12645-12665.

Olascoaga M.J., 2010, Isolation on the West Florida shelf with implications for red tides and pollutant dispersal in the Gulf of Mexico. *Nonlinear Proc. Geoph,* 176, 685–696. https://doi.org/10.5194/npg-17-685-2010.

Palacios D.M., Bograd S.J., Foley D.G., Schwing F.B., 2006, Oceanographic characteristics of biological hot spots in the North Pacific: a remote sensing perspective. *Deep Sea Res. Pt II,* 533, 50-269.

Pardo M. A., Gerrodette T., Beier E., Gendron D., Forney K. A., Chivers S. J., Barlow J., Palacios D. M., 2015, Inferring cetacean population densities from the absolute dynamic topography of the ocean in a hierarchical bayesian framework. *PLoS ONE*, 10(3), 1–23. https://doi.org/10.1371/journal.pone.0120727.

Pasqueron De Fommervault O., Perez-Brunius P., Damien P., Camacho-Ibar V. F., Sheinbaum J., 2017. Temporal variability of chlorophyll distribution in the Gulf of Mexico: Bio-optical data from profiling floats. *Biogeosciences*, 14,24, 5647–5662. https://doi.org/10.5194/bg-14-5647-2017.

Pérez-Brunius P., García-Carrillo P., Dubranna J., Sheinbaum J., Candela J. 2013. Direct observations of the upper layer circulation in the southern Gulf of Mexico. *Deep Sea Res. Pt II*, 85, 182–194. https://doi.org/10.1016/j.dsr2.2012.07.020.

Pérez-Brunius P., Furey H., Bower A., Hamilton P., Candela J., García-Carrillo P., Leben R., 2017, Dominant circulation patterns of the deep Gulf of Mexico. *Journal of Physical Oceanography*, 17,0140,1. https://doi.org/10.1175/JPO-D-17-0140.1.

Quevedo-Urías, H. A., Pérez-Salvador, B. R., 2014, *Estadística para Ingeniería y Ciencias*. Grupo Editorial Patria, México, D.F. ISBN: 978-607-438-939-5.

Roff J. C., Taylor M. E., Laughren J., 2003, Geophysical approaches to the classification, delineation and monitoring of marine habitats and their communities. *Aquatic Conservation: Marine and Freshwater Ecosystems*, 13,1, 77–90. https://doi.org/10.1002/aqc.525.

Roff J., Zacharias M., 2011, *Marine Conservation Ecology*. Earthscan publisher, Washington, D.C., USA. 439 p.p.

Salmerón-García O., Zavala-Hidalgo J., Mateos-Jasso A., Romero-Centeno R., 2010, Regionalization of the Gulf of Mexico from space-time chlorophyll-a concentration variability. *Ocean Dynam,* 614, 439–448. https://doi.org/10.1007/s10236-010-0368-1.

Saraceno M., Provost C., Lebbah M., 2006, Biophysical regions identification using an artificial neuronal network: A case study in the South Western Atlantic. *Adv Space Res,* 37, 793–805. https://doi.org/10.1016/j.asr.2005.11.005.

Soto I., Hu C., Steidinger K., Muller-Karger F., Cannizzaro J., Wolny J., Cerdeira-Estrada S., Santamaria-del-Angel E., Tafoya-del-Angel F., Alvarez-Torres P., Herrera-Silveira J., Allen J., 2011, Binational Collaboration to Study Gulf of Mexico ’ s Harmful Algae. *Eos*, 93,5, 49–50. https://doi.org/10.1016/j.csr.2004.04.007.

Tan P.N., Steinbach M., Karpatne A., Kumar V., 2018, *Introduction to Data Mining*. 2a edición. Pearson Addison-Wesley. 840 pp. ISBN: 9780134080284, 0134080289.

Vazquez de la Cerda A.M., Reid Ro., DiMarco S.F., Jochens A.E., 2005, Bay of Campeche Circulation: An Update. En: *Circulation in the Gulf of Mexico: Observations and Models*. Eds: Wilton Sturges, Alexis Lugo-Fernandez. Geoph Monog Series.161 pp.

Welsh E. S., Inoue M., 2000, Loop Current rings and the deep circulation in the Gulf. *Journal of Geophysical Research*, 105,c7, 951–959.

Wilkinson T., Wiken E., Bezaury J., Hourigan T., Agardy T., Herrmann H., Janishevski L., Madden C., Morgan L., Padilla M., 2009, *Marine ecoregions of North America*. Commission for Environmental Cooperation. Montreal, Canada. 200 pp.

Xanthopoulos P., Pardalos P.M., Trafalis T.B., 2013., Linear Discriminant Analysis. In: *Robust Data Mining*. Springer Briefs in Optimization. Springer, New York, NY. https://doi.org/10.1007/978-1-4419-9878-1_4.

Yáñez-Arancibia A., Day J.W., 2004, Environmental sub-regions in the Gulf of Mexico coastal zone: the ecosystem approach as an integrated management tool. *Ocean Coast Management,* 4711-12, 727–757. https://doi.org/10.1016/j.ocecoaman.2004.12.010.

Yáñez-Arancibia A., Day J. W., Reyes E., 2013. Understanding the Coastal Ecosystem-Based Management Approach in the Gulf of Mexico. *Journal of Coastal Research*, 63, 244–262. https://doi.org/10.2112/SI63-018.1

Zacharias M., Roff J. C., 2000, A Hierarchical Ecological Approach to Conserving Marine Biodiversity. *Conservation Biology*, 14,5, 1327–1334. https://doi.org/10.1046/j.1523-1739.2000.99191.x

Zavala-Hidalgo J., Fernandez-Eguiarte A., 2006, Propuesta para la regionalización de los mares mexicanos desde el punto de vista de los procesos físicos: el caso del Golfo de México. En: *Ordenamiento Ecológico Marino. Visión temática de la regionalización*. Córdova A., Rosete-Vergés F., Enriquez G., Hernandez, B. coords. INE, México. Pags 21-32.

Zavala-Hidalgo J., Gallegos-García A., Martínez-López B., Morey S.L., O'Brien J.J., 2006, Seasonal upwelling on the Western and Southern Shelves of the Gulf of Mexico. *Ocean Dynam.,* 563-4, 333–338. https://doi.org/10.1007/s10236-006-0072-3